FINAL REPORT
EE-SSL-1767

THERMAL MAPPING OF THE LUNAR SURFACE

By

W. L. Raine

September 1973

Prepared For

ELECTROMAGNETIC AND SOLID STATE PHYSICS DIVISION
SPACE SCIENCES LABORATORY
GEORGE C. MARSHALL SPACE FLIGHT CENTER

Contract No. NAS8-26343

Prepared By

ELECTRONICS AND ENGINEERING
TELEDYNE BROWN ENGINEERING
HUNTSVILLE, ALABAMA

ABSTRACT

A program of lunar infrared radiometry which uses large-area scanning is described. Procedures for atmospheric attenuation correction and data reduction to temperature by relative radiometry are outlined. Flow charts of the computer data reduction program are included, which also contain the astrometric analysis from ephemeral data. The scan data of ten evenings in 1971 and 1972, taken in the 10- to 12-micrometer window, are presented as isothermal contour maps of the lunar disc. More than 160 areas of anomalous thermal emission have been found in the lunar darkside data. A table is presented listing these regions. Eclipse cooling curves measured in the same wavelength band for seven lunar regions during the eclipse of February 10, 1971, are also presented. Errors of the scan and eclipse data are calculated from accuracy estimates of the parameters.

Approved:

N E Chatterton

N. E. Chatterton, Ph. D.
Manager
Research Laboratories

TABLE OF CONTENTS

LIST OF ILLUSTRATIONS

LIST OF ILLUSTRATIONS - Continued

LIST OF ILLUSTRATIONS - Concluded

LIST OF SYMBOLS

A	Difference in azimuth between the Sun and observer as seen from the point observed on the Moon (Section 4.2), lunar albedo (Section 4.1)
a_E	Altitude of the observer above the lunar horizon at the point observed
$a_\odot$	Altitude of the Sun above the lunar horizon at the point observed
b_G, ℓ_G	Selenographic coordinates of the center of the Earth, due to librations, and tabulated in the Ephemeris
b_T, ℓ_T	Selenographic coordinates of the observer
C_G	Position angle of the lunar axis viewed from the center of the Earth and tabulated in the Ephemeris
C_T	Position angle of the lunar axis seen by the observer
D(T)	The quantity $\frac{Q(T)}{T}\left(\frac{dQ}{dT}\right)^{-1}$
$d_\odot$	Lunar-solar distance, A.U.
F_c	Lunar surface conducted flux
$F_\odot$	The total solar flux at 1 A.U.
h_D, δ_D	Topocentric hour angle and declination of the detector field
h_{Di}, δ_{Di}	Coordinates of photographed points in a scan
$\bar{h}_D$, $\bar{\delta}_D$	Average topocentric coordinates of a series of points
$\dot{h}_D$, $\dot{\delta}_D$	Rates of telescope motion in hour angle and in declination
h_G	Geocentric hour angle of the center of the Moon
h_P, δ_P	Topocentric coordinates of a photographed point
h_T, δ_T	Topocentric coordinates of the lunar center

ℓ	Selenographic longitude of object point
$\ell_\odot$	Solar selenographic longitude
$\Delta\ell$	Change in selenographic longitude between Earth center and observer
$N(\lambda, T)$	The Planck expression for radiation by a blackbody, expressed as a radiance
Q	Angle at the sublunar point between great circles through the Earth's north pole and the observer, measured as positive eastward from the pole
Q(T)	Integral of the Planck blackbody expression, weighted by the normalized radiometer responsivity and expressed as a radiance
R	Topocentric distance to the lunar center in units of the lunar radius
$R_d(\lambda)$	Spectral detector responsivity
$R_s(\lambda)$	Spectral radiometer responsivity $[\tau_w(\lambda)\,\tau_f(\lambda)\,R_d(\lambda)]$
R_i	Subscript referring to extinction observations
R_{max}	Maximum value of $R_s(\lambda)$
r	Apparent angle between the antisolar direction and a lunar surface point
ST_o	Greenwich sidereal time at 0^h, Universal Time, tabulated in the Ephemeris
T	Brightness temperature
T_m	Lunar surface temperature
T_o	Subsolar point temperature
t	Time

U.T.	Universal Time
V	Signal voltage
ΔV_b	Residual background signal due to incomplete cancellation of background
V_m	Radiometer signal due to transmitted lunar radiation only
V_m'	Actual radiometer signal during lunar observation
X	Air mass
X, Y, Z	Coordinates of detector field with origin at observer, Z axis through celestial equator below lunar center, and X axis pointing eastward in units of the lunar radius
X', Y', Z'	Direction cosines of an object point, with the same axis directions as the X, Y, Z system and origin at the observer
x, y, z	Coordinates of the observed point in units of the lunar radius with origin at the center of the Moon, z-axis pointing toward the observer and y-axis in the plane containing the lunar north pole and observer
x', y', z'	Coordinates of the observed point in units of the lunar radius, with origin at the observer, z'-axis through the lunar center, and x' axis pointing eastward
x'', y'', z''	Direction cosines of an object point, with origin at the observer, z''-axis through the lunar center and x''-axis pointing eastward
x''', y''', z'''	Coordinates of the intersection of the line of sight with a plane containing the lunar center and perpendicular to a line joining the observer and lunar center, in units of the lunar radius; same origin and axis directions as the x'', y'', z'' system
x_E, y_E, z_E	Coordinates of the sub-observer point in the x, y, z, system

x_o, y_o	Coordinates of the intersection mentioned in the definition for x''', y''', z''' in the x, y, z system
Z_G	Geocentric zenith angle of the lunar center
Z_P	Topocentric zenith angle of the photographed point
$Z_\odot$	Lunar surface solar zenith angle
α_D, δ_D	Astronomical coordinates of the detector field
α_G, δ_G	Geocentric right ascension and declination of the lunar center, tabulated in the Ephemeris
α_P	Topocentric right ascension of the photographed point
α_T	Topocentric right ascension of the lunar center
$\dot{\alpha}$, $\dot{\delta}$	Apparent angular velocities of the Moon relative to the antisolar direction (Earth's shadow) in right ascension and declination
α_o, δ_o	Zero-point constants in right ascension and declination
$\Delta\alpha_o$, $\Delta\delta_o$	Lunar surface point shift in right ascension and declination
$\bar{\epsilon}_m$	Average lunar emissivity
θ	Angle between the Sun and observer in the lunar sky at the point observed
λ	Wavelength (Section 4.2); the observer's longitude (Section 4.3)
ξ, η, ζ	Lunar orthographic coordinates of the observed point
ξ_i, η_i	Lunar orthographic coordinates of the ith photographed point in a scan
ξ_E, η_E, ζ_E	Lunar orthographic coordinates of the sub-Earth point

$\xi_\odot$, $\eta_\odot$, $\zeta_\odot$	Lunar orthographic coordinates of the subsolar point
π_G	Geocentric horizontal lunar parallax, tabulated in the Ephemeris
π_T	Topocentric lunar parallax
ρ	Ratio of the Earth center-observer distance to the equatorial radius of the Earth
$\rho_t(\lambda)$	Spectral reflectivity of a telescope mirror
τ	Time measured in lunar days
$\bar{\tau}_a$	Average atmospheric transmission over the band of observation
$\tau_a(\lambda)$	Spectral transmission of the atmosphere
$\tau_f(\lambda)$	Spectral transmission of filter
$\tau_w(\lambda)$	Spectral transmission of window
ϕ'	Observer's geocentric latitude
$\odot$	Subscript referring to solar quantities
1i, 2i	Subscripts referring to initial and final calibration point measurements

1. INTRODUCTION

Infrared radiometric measurements of lunar heat radiation began in 1929 with the measurements of Pettit and Nicholson (Ref. 1). Their instrument incorporated a vacuum thermocouple attached to the 100-inch reflector at Mt. Wilson. These workers successively measured the entire lunar radiation transmitted by the atmosphere, and the radiation transmitted by a microscope cover glass. The difference in these measurements was assumed to be entirely heat radiation. Their effective wavelength band essentially covered the region from 8 to 14 micrometers. Their observations included a number of scans across the disc, measurements of the subsolar point, and eclipse measurements.

The first isothermal maps of the daytime lunar surface were constructed in 1960 by Geoffrion, Korner, and Sinton (Ref. 2) from measurements with a pyrometer in the spectral band from 8.0 to 9.5 micrometers. Eclipse measurements of the crater Tycho were also made by Sinton (Ref. 3).

The most extensive measurements of the illuminated lunar surface have been made by Saari and Shorthill (Ref. 4). Their radiometer contained a mercury-doped germanium photodetector working in the band from 10 to 12 micrometers. These authors have completely mapped the daytime lunar surface, both in the infrared and, with a phototube in the visual region, at selected phases throughout a lunation. Their measurements have also been presented as isothermal contour charts. Their data are of high spatial resolution, and the charts clearly show contours outlining specific features. Calculated temperatures for the lunar subsolar point were used for their absolute calibration.

Largely because of the relatively low signal, somewhat fewer measurements have been taken of the nighttime lunar surface. Measurements have been made by Saari (Ref. 5), by Low at 20 micrometers (Ref. 6), by Mendell and Low also at 20 micrometers (Ref. 7), and by Murray and Wildey in the 8- through 14-micrometer band (Ref. 8). This last group used a mercury-doped germanium detector cooled to liquid hydrogen temperature. These authors have also constructed a thermal contour chart of the nighttime surface near last quarter phase under rather low resolution (Ref. 9).

Measurements of the temperature of the lunar nighttime surface are important in ascertaining the thermal environment to which instrumentation left on the Moon will be subjected. Such measurements are more important than lunar daytime surface measurements in the definition of the thermophysical structure of the near surface layers. More extensive radiometric data of the lunar nighttime surface are clearly needed.

For the past 4 years, Teledyne Brown Engineering has been involved in the acquisition of such measurements in cooperation with the Space Sciences Laboratory, MSFC (Refs. 10 through 17 and 26). The dewar-detector system for these measurements was obtained from Infrared Industries of Tucson, Arizona, and the radiometer was designed and developed by Teledyne Brown Engineering.

The radiometer uses dual germanium bolometric detectors working in bands from 10 to 12 micrometers and from 17.7 to 25.0 micrometers. Most of the work to date has been in the 10- to 12-micrometer band. The radiometer has been used attached to a 30-centimeter telescope in Huntsville, and also attached to a 1.5-meter telescope in Arizona.

The theory of measurement is simple. A measurement is made of the lunar radiance in the wavelength band of the instrument. Both infrared spectral bands lie at sufficiently long wavelengths that scattered sunlight from the surface is negligible. The radiation observed is, therefore, primarily lunar heat radiation. With the assumption that this measured radiance is described by the Planck Radiation Function, a corresponding temperature is calculated. The temperature obtained is, therefore, a brightness temperature, rather than a color temperature.

Because of problems of diffraction of the radiation by the field limiting apertures located within the dewar, and also because of alignment problems, it was decided to perform the absolute calibration of the radiometer with the Moon as the source. The measurements of Saari and Shorthill were used for this purpose. The astrometric analysis was done according to the procedure of Ingrao (Ref. 18).

The results of the scan data are presented here as isothermal contour charts. The lunar phases mapped and amounts of data for each are presently incomplete, because of difficulties with the equipment and weather.

Radiometric data were also taken during the total lunar eclipse of February 10, 1971. Data in the 10.0- to 12.5-μ band were recorded for seven regions, and cooling curves are presented here for each.

The results presented here represent a culmination of the efforts of a number of people. The author wishes to thank the following persons, without whose help these results would have been impossible. The first four named individuals especially have made major contributions.

Mr. W. F. Fountain has been the coordinator for NASA for the Project. He has worked tirelessly with the observational apparatus and the telescope. Mr. M. W. Segewitz assembled the complete data acquisition system, has helped in the acquisition of data, and has been responsible for the continued operation of the apparatus. Mr. J. A. Fountain has worked significantly at the telescope and with the lunar photographs. The computer-reduction program was written by Mr. J. Van Swearingen from flow charts supplied by the author, and he has been responsible for the complete computer reduction.

Mechanical design of the radiometer was performed by Mr. R. Norton. The camera synchronization unit was constructed by Mr. M. Deasy. Messrs. M. White, R. White, E. West, and Miss S. Sneed have analyzed many of the lunar photographs and have supplied the lunar reference point temperatures and the necessary ephemeral data. Messrs. E. George, D. Montgomery, and J. Sanders assisted in the compilation of the table of anomalies.

2. THE RADIOMETER

The radiometer has been previously described in detail (Ref. 16). Therefore, only a brief description is presented here.

An optical schematic of the instrument is shown in Figure 2-1. The radiometer was designed to accept a cone of radiation of about F/16, which is typical of Cassegrain telescopes. Radiation from the telescope enters at the top of the figure. The 10-hertz chopper alternately passes the lunar radiation into the dewar, or below to the visual section of the instrument. The sky mirror reflects sky background radiation into the dewar between chop cycles. The light entering the visual section of the instrument passes first through the thick glass image deflector plate, and is reflected by the focal plane mirror through a lens reimaging system to the eyepiece or camera. A visual photometer may be added as an accessory directly below the focal plane mirror. Light is passed to this unit through a small hole in the coating of that mirror.

The focal plane mirror has four fine wires glued to its surface to serve as a crosshair. When the instrument is in use, this mirror is carefully adjusted so that the crosshair is optically in precisely the same position as the infrared detector. An x-y screw motion serves as a coarse adjustment for this alignment, and the image deflector plate provides the fine adjustment. Photographs made with the camera, and also observation through the eyepiece, reveal the crosshair superposed on the lunar image, and these mark the exact position of the detector field.

The dewa contains dual germanium bolometric detectors cooled by liquid helium. These detectors are each 0.5 millimeter in diameter,

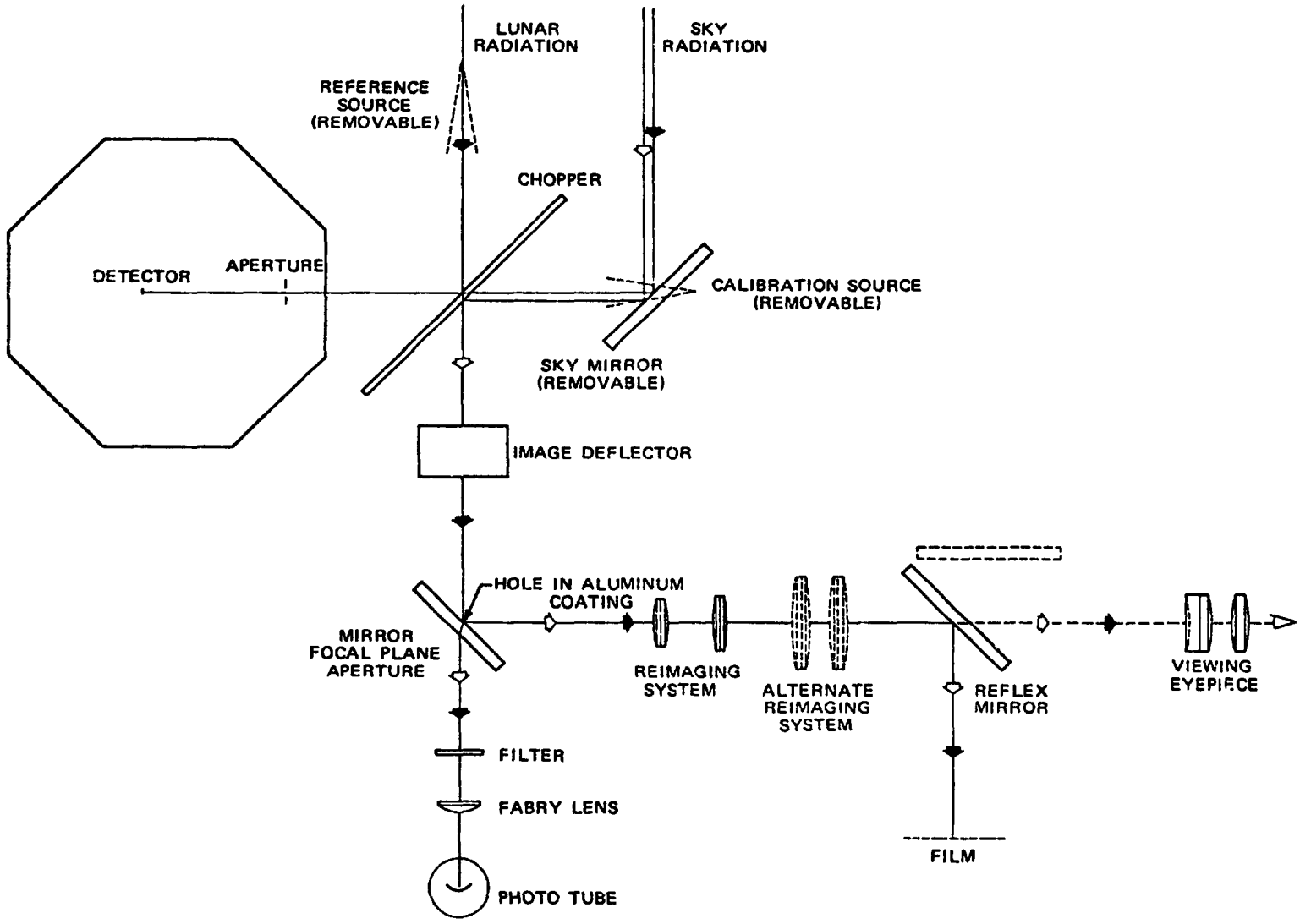

FIGURE 2-1. OPTICAL SCHEMATIC OF THE RADIOMETER

and correspond to an angular resolution of 22 arcseconds with the 30-centimeter telescope, and 4.5 arcseconds with the 1.5-meter telescope. Sensitivity of the detectors is enhanced by pumping on the liquid helium, which produces a temperature drop to less than 2°K. Filters provide response in the regions from 10 to 12 micrometers and 17.7 to 25.0 micrometers. The relative detector-dewar response curves are shown in Figures 2-' and 2-3. Cooled apertures inside the dewar limit the field of view so that the detectors see primarily mirror surfaces. The detectors may not be used simultaneously.

Since the instrument incorporates a chopper which chops alternately between lunar and sky radiation, the detector output is an ac signal. The preamplifiers for the two channels are mounted directly to the dewar. From the preamplifier, the signal goes to an amplifier designed for this system by Dr. F. J. Low of the University of Arizona. A phase signal transmitted from the chopper to this unit also allows the amplifier to synchronously rectify the signal. The resultant dc voltage, which nearly represents the signal caused solely by transmitted radiation, is recorded by a Hewlett-Packard Data Acquisition System. The system consists of a scanner, digital voltmeter, clock, paper printer, counter, and magnetic tape recording system. For all of the data reported here, an integration time of 1 second has been used.

A separate, custom-built unit allows synchronization of the camera with the chopper. At the moment that a photograph is taken, the time and a frame number are recorded on the film by a unit attached to the camera back. This information is also simultaneously recorded on the paper printout and magnetic tape. The radiometer as attached to the 60-inch SSL-LPL telescope is shown in Figure 2-4.

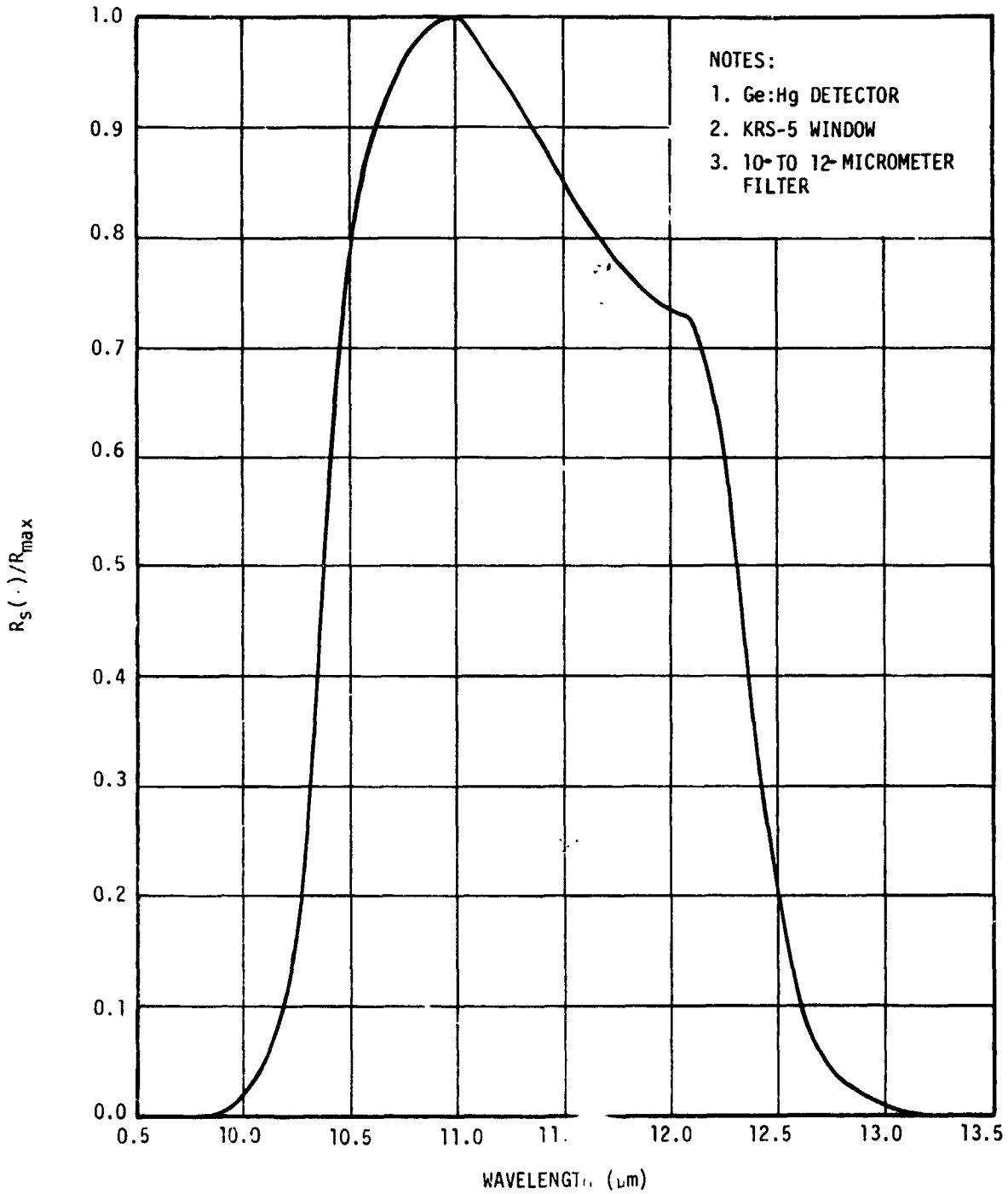

FIGURE 2-2. NORMALIZED RESPONSIVITY OF THE RADIOMETER IN THE 10.0- TO 12.5-MICROMETER SPECTRAL BAND

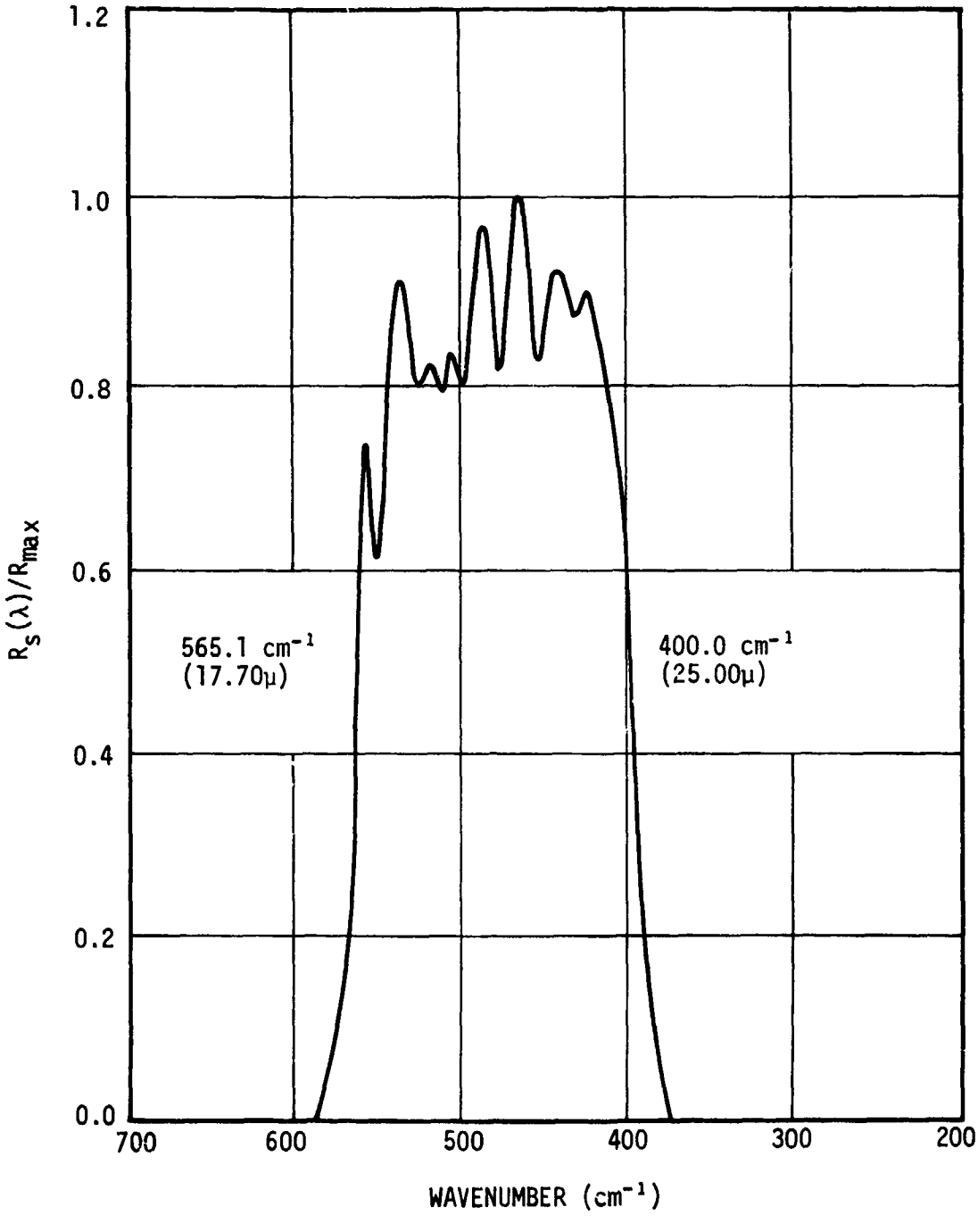

FIGURE 2-3. NORMALIZED RESPONSIVITY OF THE RADIOMETER IN THE 17.7- to 25.0-MICROMETER SPECTRAL BAND

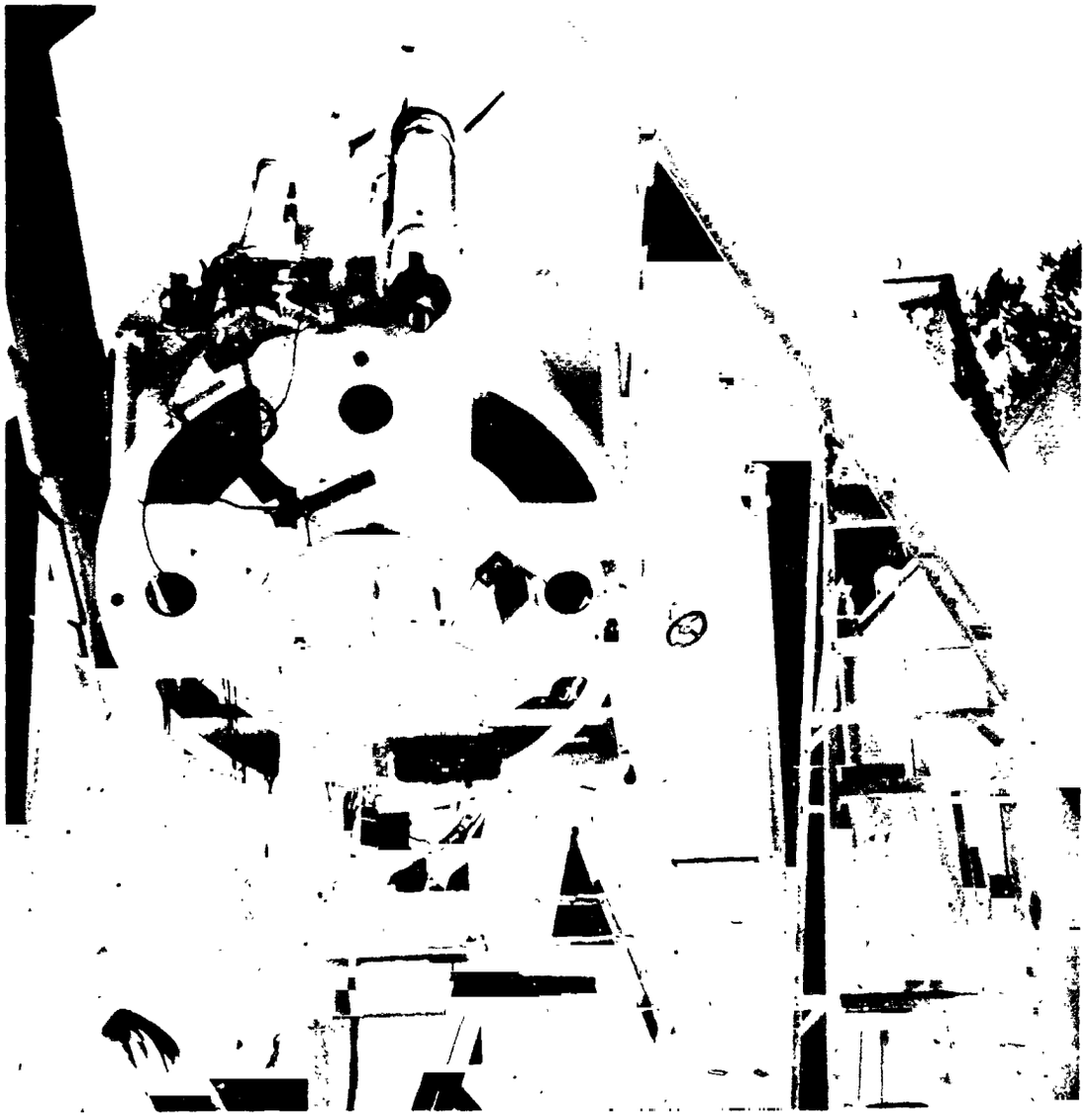

FIGURE 2-4. THE RADIOMETER AS ATTACHED TO THE 60-INCH SSL-LPL TELESCOPE

3. THE OBSERVATIONAL DATA

Regular observations with the infrared radiometer began in December 1970. Since that time, data have been obtained in numerous sessions. These data are from both the Huntsville and Arizona locations and are in the 10- to 12-micrometer band. For sites having reasonable atmosperic transmission at 20 micrometers, the longer wavelength is to be preferred, since the major portion of radiation from the cool lunar nighttime surface is at these wavelengths. However, because of the low altitude and relatively humid climate at Huntsville, it is dubious that any benefit would be gained by observing from Huntsville in the 17.7- to 25.0-micrometer band. The Arizona site, which is at an altitude of 8,500 feet in the Catalina Mountains near Tucson, is more suited to the longer wavelength band.

For scan data, the observational routine is as follows:

- At the beginning of the evening, a single point on the lunar surface, usually near the subsolar point, if possible, and in a maria region, is selected for measuring atmospheric attenuation. This "extinction point" is observed first.

- A series of calibration points, located away from the terminator or in rough highland regions, is observed next. These points are otherwise widely distributed over the surface.

- The acquisition of scan data is begun next. Usually, these are drift scans, i.e., the diurnal motion of the Earth is used to carry the lunar image past the detector. For shifting of the scans in declination, either the lunar motion in declination is used, or the scans are shifted by incremental movements of the telescope in declination. The latter is somewhat awkward, and spatial resolution is sometimes improved by quickly rescanning lunar regions. A portion of sky

is always included at each end of each scan. At least one photograph is recorded during passage across the illuminated portion. The extinction point is periodically measured during the scanning period.

- At the end of the scanning session, the calibration points are measured again.

- Finally, a measurement is made of the extinction point.

During periods in which extinction or calibration points are being measured, a sky background reading is taken with both radiometer beams. For each type of observation, a manually set code is entered on the tape. This code includes the wavelength (10 or 20 micrometers), the site (Huntsville or Arizona), the lunar calibration point for a calibration observation, the type of observation (extinction point, calibration point, sky reading, or scan data), and the date. Recording of this code is effected with the taking of a photograph, which is done for each type of observation. Photographs during scanning are necessary in order to carry out the astrometric analysis. The photographs of the extinction and calibration points are essential later in the determination of temperatures of these points from the Saari and Shorthill data. Photographs taken during the sky readings provided an additional check against stray radiation. The time is periodically recorded automatically on the tape.

The reader will note that separate observations are made for extinction and calibration points. These could be combined, but the opportunity of holding one of the two basic independent variables (source temperature or air mass) constant for each determination affords greater accuracy. In determination of the attenuation coefficient, widely varying air mass values, but constant source temperature, are desirable; in determination of the calibration constant, a single air mass with widely varying source temperatures yields the most accurate value. Since the scans cross illuminated portions of the disc for which

the data of Saari and Shorthill may be interpolated, the separate measurement of extinction or calibration points might even be ignored completely. However, use of this scan data for calibration and extinction correction would needlessly complicate the data reduction routine.

Table 3-1 presents a summary of the observational data obtained to date. Included in this table are the date, wavelength region of the observations, the site (Huntsville or Arizona), the number of scans recorded, and the solar selenographic colongitude. The reader will note that these observations are incomplete, which is due to difficulties with the instrumentation or the weather.

Planetary data have also been obtained. Sufficient data for a low resolution thermal map of Jupiter were recorded on May 31, 1971, at Huntsville in the 10.0- to 12.5-micrometer band. Measurements for higher resolution thermal maps of Mars were obtained in the same band at the Arizona observatory. These data were recorded during the recent favorable opposition, on September 11 and again on September 16, 1971. Time has not yet allowed reduction of these data.

Radiometric measurements of Saturn were also attempted during September 1971, from the Arizona station. The planet could not be detected in the 10.0- to 12.5-micrometer band due to noise. A later noise analysis indicated an upper limit brightness temperature of 100°K. This is in agreement with the previous estimate of 95°K for the planet (Ref. 15).

TABLE 3-1. SUMMARY OF LUNAR SCAN OBSERVATIONS

DATE (GREENWICH)	WAVELENGTH (μ)	SITE	NO. SCANS	SOLAR SEL. COL.	REMARKS
12/18/70	10 to 12	H	13		Tape unit malfunction
12/24/70	10 to 12	H	16		Tape unit malfunction
1/16/71	10 to 12	H	70	143°	Darkside data
1/20/71	10 to 12	H	12		
2/6/71	10 to 12	H	34		
2/15/71	17 to 25	A	6		
2/19/71	10 to 12	A	33		No photos, but recoverable
5/31/71	10 to 12	H	50		No darkside data, 13 Jovian scans
6/1/71	10 to 12	H	50		
9/11/71	10 to 12	A	45	168°	Darkside data, 8 Martian scans
9/12/71	10 to 12	A	62	181°	Darkside data
9/13/71	10 to 12	A	19		Darkside data
9/14/71	10 to 12	A	37		Darkside data, 10 Martian scans on 16th
10/30/71	10 to 12	H	55		No darkside data
11/4/71	10 to 12	H	87		Full moon data
11/5/71	10 to 12	H	62	116°	Darkside data
11/8/71	10 to 12	H	50	154°	Darkside data
11/11/71	10 to 12	H	30		Darkside data
11/14/71	10 to 12	H	40	206°	Darkside data
11/21/71	10 to 12	H	7		
11/22/71	10 to 12	H	21		
1/24/72	17 to 25	A	56		No darkside data
1/25/72	10 to 12	A	71		No darkside data
1/27/72	10 to 12	A	72		No darkside data
9/26/72	17 to 25	A	44		Darkside data
9/29/72	10 to 12	A	41	170°	Darkside Data
9/30/72	10 to 12	A	50	182°	Darkside Data
10/1/72	10 to 12	A	55	194°	Darkside Data
10/2/72	10 to 12	A	33	207°	Darkside Data

NOTES: A - Arizona Data, H - Huntsville Data

4. DATA REDUCTION

4.1 REDUCTION OF THE MEASUREMENTS TO BRIGHTNESS TEMPERATURES

For several reasons it was decided to effect absolute calibration of the entire radiometer-telescope system upon the Moon. These are as follows:

- Fresnel diffraction occurs at the baffling apertures inside the dewar (Ref. 17). Diffraction affects the focusing of the radiation upon the detector and therefore the geometrical factors occurring in the equations for absolute calibration and radiation measurement. Even with an electronic computer, calculation of these diffraction-modified constants would be arduous in practice.

- The precise alignment of the dewar-detector system with the telescope required for laboratory calibration would be difficult to achieve. Inaccuracy of this alignment would degrade the accuracy of the results.

- Calibration of the entire radiometer-telescope system upon the Moon eliminates the necessity of knowledge of optical parameters such as emissivities and mirror reflectivities. The geometrical arrangement may be any whatever. The method is also less sensitive to errors in atmospheric attenuation correction.

The reader may recall that relative radiometry is not uncommon in astronomy. It has been used, for example, by Saari and Shorthill (Ref. 4) and by Low (Ref. 6).

Our procedure is the determination of an absolute calibration constant for the entire telescope-radiometer system. The extensive data of Saari and Shorthill, after correction for the local solar zenith angle and distance, are suitable for this purpose. At each observing

session a series of calibration points, including an extinction point, is selected on the lunar surface. These are selected in maria regions well removed from the terminator. This is done since the temporal and spacial variations in brightness temperature are the least in these regions, and the approximate procedure used for solar zenith angle correction is invalid in the terminator region. In addition, use of warmer regions for calibration produces smaller fractional errors in the measured temperatures, as shown by examination of the factor $[D(T_C)]^{-1}$, which appears in Equations 6-5 and 6-6. Otherwise, these points are widely selected over the illuminated surface.

The signal voltage V_m due to detected lunar radiation is related to the lunar surface temperature T_m by

$$V_m = G_T \int_C^\infty \tau_a(\lambda)\, \rho_T^3(\lambda)\, \epsilon_m(\lambda)\, R_s(\lambda)\, N(\lambda,\ T_m)\, d\lambda \quad . \quad (4\text{-}1)$$

The constant G_T is a geometrical factor which depends upon telescope and detector system parameters such as telescope collecting area, focal length, detector and baffling aperture sizes and separation. Variation of G_T with wavelength due to diffraction effects is small. All other parameters on the right side of Equation 4-1 are wavelength dependent and are included in the integrand. These are the atmospheric transmission $\tau_a(\lambda)$, the mirror reflectivity $\rho_T(\lambda)$, the lunar surface emissivity $\epsilon_m(\lambda)$, the responsivity $R_s(\lambda)$ of the complete detector-dewar system including the filter and optical window, and the blackbody radiance $N(\lambda,\ T_m)$ corresponding to the lunar surface temperature, T_m.

It is anticipated that the quantities $\rho_T(\lambda)$ and $\epsilon_m(\lambda)$ will remain fairly uniform over the wavelength ranges of interest (10.0 to 12.5 micrometers and 17 to 25 micrometers). Although there is some

variation of τ_a with λ in the 10.0- to 12.5-micrometer band, this wavelength region corresponds to an excellent atmospheric "window". The window in the 17- to 25-micrometer band is not nearly as good, and the variation of τ_a with λ is more pronounced there. If average values for ρ_T, ϵ_m, and τ_a over wavelength are used, these quantities may be taken outside the integral and Equation 4-1 may be rewritten as

$$V_m = G_T \bar{\rho}_T^3 \bar{\epsilon}_m R_{max} \bar{\tau}_a Q(T_m) \quad . \qquad (4\text{-}2)$$

Here R_{max} represents the maximum value of $R_s(\lambda)$ in the wavelength interval, and the function $Q(T_m)$ is defined by

$$Q(T_m) = \int_0^\infty \frac{R_s(\lambda)}{R_{max}} N(\lambda, T_m)\, d\lambda \qquad (4\text{-}3)$$

and is seen to be the integrated lunar surface radiance weighted by the normalized radiometer responsivity.

The infrared atmospheric absorption spectrum is largely characterized by molecular absorption bands which are composed in turn of multitudes of absorption lines. In order to facilitate the calculation of the infrared transmission of gases over broad wavelength regions band model approximations have been devised. Two important models consider the absorption lines in the band as uniformly spaced (Elsasser model, Ref. 19), or as randomly spaced (Goody model, Ref. 20). These models have been further simplified in the case of weak lines, or of strong lines. Since the wavelength region from 10.0 to 12.5 micrometers corresponds to an excellent window, $\bar{\tau}_a$ has been represented in this band by the weak line case (Ref. 21) for these models with air mass as argument. Here $\bar{\tau}_a$ is given by

$$\bar{\tau}_a = \exp(-k_1 X) \quad , \tag{4-4}$$

where the constant k_1 is an extinction coefficient and X is the air mass. The stronger attenuation in the 17- to 25-micrometer region is dominated by H_2O absorption, which consists of randomly spaced lines. Consequently, for this band, the strong-random band model approximation (Ref. 21) has been chosen. This approximation predicts the functional form of $\bar{\tau}_a$ to be

$$\bar{\tau}_a = \exp(-k_2 \sqrt{X}) \quad , \tag{4-5}$$

where k_2 is the attenuation coefficient and the air mass is again used as argument. Although the band-model approximations for both bands have been incorporated into the computer-reduction program, only data in the 10.0- to 12.5-micrometer band have been reduced to date.

Because of the radiation chopping method employed, the actual signal voltage V_m' recorded during lunar observation is very nearly equal to the signal voltage V_m due solely to detected lunar radiation. However, due to slight imbalances in the two radiometer beams, a residual background component ΔV_b may be present in V_m'. Periodic sky observation with both beams provides this component. The corrected signal V_m is then obtained from

$$V_m = V_m' - \Delta V_b \quad . \tag{4-6}$$

Since the variation of $\bar{\epsilon}_m$ with the lunar topography is not known, the product $G_T \bar{\rho}_T^3 \bar{\epsilon}_m R_{max}$ in Equation 4-2 may be represented by a single symbol. Let

$$K = G_T \bar{\rho}_T^3 \bar{\epsilon}_m R_{max} \quad . \tag{4-7}$$

After substitution of Equations 4-6 and 4-7 into Equation 4-2, Equation 4-2 becomes

$$V_m' - \Delta V_t = K \bar{\tau}_a Q(T_m) \quad . \tag{4-8}$$

Equations 4-8, and 4-4 or 4-5, and the definition of $Q(T_m)$ given by Equation 4-3 are the basic relationships used in reduction of the measurements to temperature values.

In order to effect absolute calibration and to facilitate determination of the extinction coefficient, the lunar surface reference point temperatures are needed. These are read from the Saari and Shorthill data and are corrected for differences in local solar zenith angle and the solar-lunar distance. At the lunar surface, the condition

$$\text{Absorbed solar flux} = \text{Flux conducted inward} + \text{Radiated flux}$$

must be met. Symbolically, this condition is expressed by

$$(1 - A) F_\odot \frac{\cos Z_\odot}{d_\odot^2} = F_c + \bar{\epsilon}_m \sigma T_m^4 \tag{4-9}$$

where

A - lunar albedo

$F_\odot$ - total solar flux at a distance of 1 A.U. (the solar constant)

$Z_\odot$ - lunar local solar zenith angle

$d_\odot$ - solar-lunar distance, A.U.

F_c - inwardly conducted flux.

For lunar daytime regions not near the terminator, previous studies (Ref. 22) indicate that the term F_C is small. In this case

$$(1 - A)\, F_\odot \frac{\cos Z_\odot}{d_\odot^2} \approx \bar{\epsilon}_m \sigma T_m^4 \quad . \tag{4-10}$$

The quantity $\cos Z_\odot$ may be expressed in terms of the orthographic coordinates ξ, η, ζ, of any point and the coordinates $\xi_\odot$, $\eta_\odot$, $\zeta_\odot$, of the subsolar point by

$$\cos Z_\odot = \xi \xi_\odot + \eta \eta_\odot + \zeta \zeta_\odot \quad . \tag{4-11}$$

Under two different conditions of illumination, Equations 4-10 and 4-11 indicate that the lunar surface temperatures T_{m1} and T_{m2} are related by

$$T_{m2} = T_{m1} \left[\frac{\xi \xi_{\odot 2} + \eta \eta_{\odot 2} + \zeta \zeta_{\odot 2}}{\xi \xi_{\odot 1} + \eta \eta_{\odot 2} + \zeta \zeta_{\odot 1}} \right]^{\frac{1}{4}} \left[\frac{d_{\odot 1}}{d_{\odot 2}} \right]^{\frac{1}{2}} \quad . \tag{4-12}$$

For each calibration point or extinction point, temperature values are read from the Saari and Shorthill charts having phase angles straddling the phase angle of the observations. These are corrected to our conditions by Equation 4-12. The difference in these corrected values is usually small (a few K degrees or less), and an interpolation over phase angle is used to obtain the final value. Presently this procedure has not been incorporated into the computer-reduction program, but rather is done by hand.

The atmospheric attenuation coefficient is obtained as the first stage of the computer-reduction program. Let T_R be the lunar surface extinction point temperature. Expressions 4-4 and 4-5 may be substituted, in turn, into Equation 4-8 which is then rewritten as

$$\ln \left[\frac{V_R' - \Delta V_b}{Q(T_R)} \right] = -k_1 X + \ln K \qquad (4\text{-}13)$$

for the weak line model, and as

$$\ln \left[\frac{V_R' - \Delta V_b}{Q(T_R)} \right] = -k_2 \sqrt{X} + \ln K \qquad (4\text{-}14)$$

for the strong-random line model. Observations of the reference point should be made for various values of air mass X. A straight line fitted to a plot of the left side of Equation 4-13 as a function of X yields $-k_1$ as slope for the weak line model. For the strong-random line model, $-k_2$ is the slope of a straight line fitted to a plot of the left side of Equation 4-14 as a function of $\sqrt{X}$. Note that in both cases the plots yield $\ln K$ as the $X = 0$ intercept. However, use of nearly simultaneous multiple calibration points as described above is to be preferred for the determination of K.

Observation of a single calibration point of known temperature T_c is sufficient for the determination of K. A more accurate determination is possible if several points are measured. The well-known method of least squares may be used to fit the observations of $V_c' - \Delta V_b$ as a function of $\bar{\tau}_a Q(T_c)$ with a line passing through the origin. The value of K is then given by

$$K = \frac{\sum_{i=1}^{N} \bar{\tau}_{ai} Q(T_{ci}) (V_{ci}' - \Delta V_b)}{\sum_{i=1}^{N} [\tau_{ai} Q(T_{ci})]^2} \qquad (4\text{-}15)$$

for N calibration points. Because of a possible slight variation of K, values of this calibration parameter are obtained from observations at the beginning of an observing session and again from observations at the end of the session. The value used in the data reduction is interpolated from these observations.

Note that a constant value for K is assumed in determination of the attenuation coefficient. Although this may produce a small error in this coefficient, only a much smaller error is produced in the determined temperature values, since the measurements are relative. Interpolation of the K values still provides a good correction.

The value of K obtained is correct, regardless of diffraction effects, and the telescope-radiometer geometry may be any whatever. The method is also independent of the alignment of the optics, provided it is unchanged.

The value of $Q(T_m)$, and, therefore, T_m, is then determined for any unknown point by evaluation of the quantity

$$Q(T_m) = \frac{V_m' - \Delta V_b}{K \bar{\tau}_a} \quad . \tag{4-16}$$

Early in the project, in an effort to increase effective resolution in the advance direction, successive rescanning of the lunar disc was tried. Trouble with this procedure was encountered due to lunar surface temperature variations with phase change and atmospheric transparency variations during the several-hour time period required for scanning. A procedure, which is based on thermophysical lunar surface models, was devised for making adjustments to surface temperatures for phase changes which would be valid over small time periods. This procedure is described in the appendix. In practice, the maximum amount of the adjustment has been about 10 K° with the

bulk of the adjustments less than 1 K°. This procedure satisfactorily solved the phase change problem, but the more significant atmospheric transparency variation problem remained. Subsequent data have been taken in single scannings of the lunar disc with a larger number of scans recorded. However, because of its success the adjustment procedure has remained in the program.

4.2 THE COMPUTER REDUCTION PROGRAM

The procedure for the astrometric analysis of the data is that of Ingrao, et al and has been previously described in detail (Refs. 18, 14, and 16). The procedure for reduction of the measurements to temperatures is presented in Section 4.1. This section, therefore, presents only a brief description of the computer reduction program, as shown in the accompanying flow charts.

The data, which is entered on magnetic tape, is divided into separate files on the tape. Each file consists of an integral number of records, each of which consists, in turn, of 24 signal values and a time value (in hours, minutes, and seconds). The files are used for separation of the types of data recorded, and also to separate the individual lunar disc scans. For lunar work, four file types are used: calibration files, extinction point files, sky files, and a data point file for each disc scan. Each file is identified by a manually set code within the file. After reading these codes, the computer may call the file when needed. All signal values in each calibration file, extinction point file, and sky file are averaged by the computer. One of these files, therefore, constitutes a single observation, and the sky files are used for the correction of the calibration and extinction point files.

A summary of the entire reduction program is shown in Figure 4-1. The detailed flow charts are divided into eight sheets. Five of these sheets present the basic program, and the three remaining

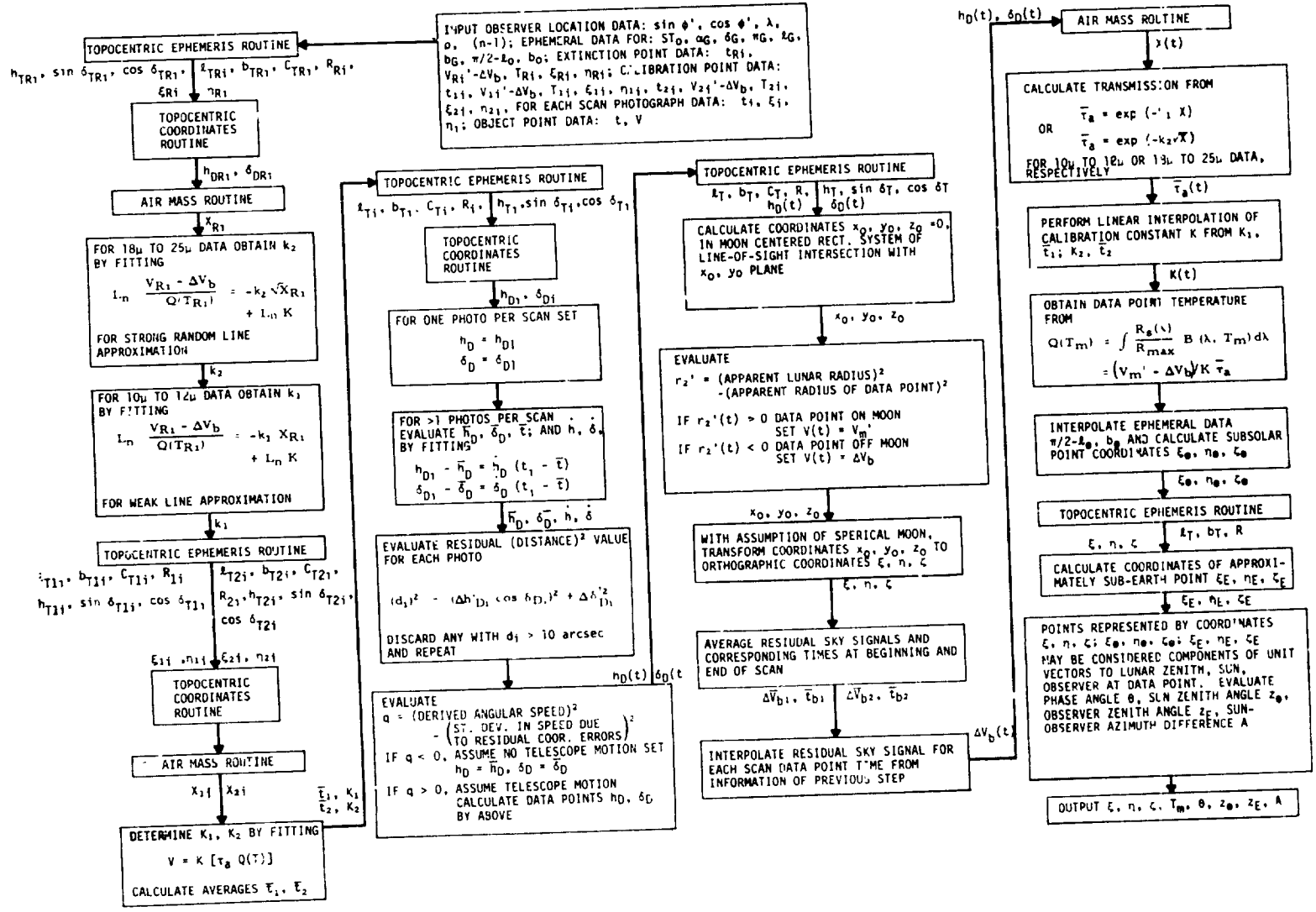

FIGURE 4-1. OUTLINE OF THE COMPLETE SCAN REDUCTION PROGRAM

sheets outline routines which are used repeatedly in the program. These routines will be described first, followed by a description of the main program.

The topocentric ephemeris routine is outlined in Figure 4-2. The Ephemeris (Ref. 23) presents data as geocentric quantities, and this routine is used for conversion of these data to topocentric quantities. In the flow charts, the numbers on the blocks show the order of the calculations, and the arrows show the flow of quantities. The routine is entered with the ephemeral data, the observer's coordinates, and the time. Interpolation of the ephemeral data is followed by calculation of the geocentric hour angle and zenith angle, the observer's position angle, and the topocentric parallax. Other auxiliary quantities are calculated which allow translation of the geocentric lunar coordinates and distance to topocentric values. The outputs of this routine are the topocentric librations in selenographic longitude and latitude, the topocentric lunar position angle, the topocentric lunar distance in units of the lunar radius, and the topocentric coordinates of the lunar center.

The topocentric coordinates routine is shown in Figure 4-3. This routine describes the calculation of topocentric hour angle and declination for any point on the lunar surface from the input orthographic coordinates. The quantities input to the routine are the lunar orthographic coordinates ξ and η, topocentric ephemeral data computed in the topocentric ephemeris routine, the sine and cosine of the observer's latitude, and the differential refractive index between the visual and infrared wavelengths. The first portion of the routine transforms the orthographic coordinates in succession through three other rectangular coordinate systems. These coordinate systems are described fully in Reference 16. This is followed by conversion to topocentric hour angle and declination. These are the coordinates of the photographed point. The final conversion of the routine transforms these coordinates to the

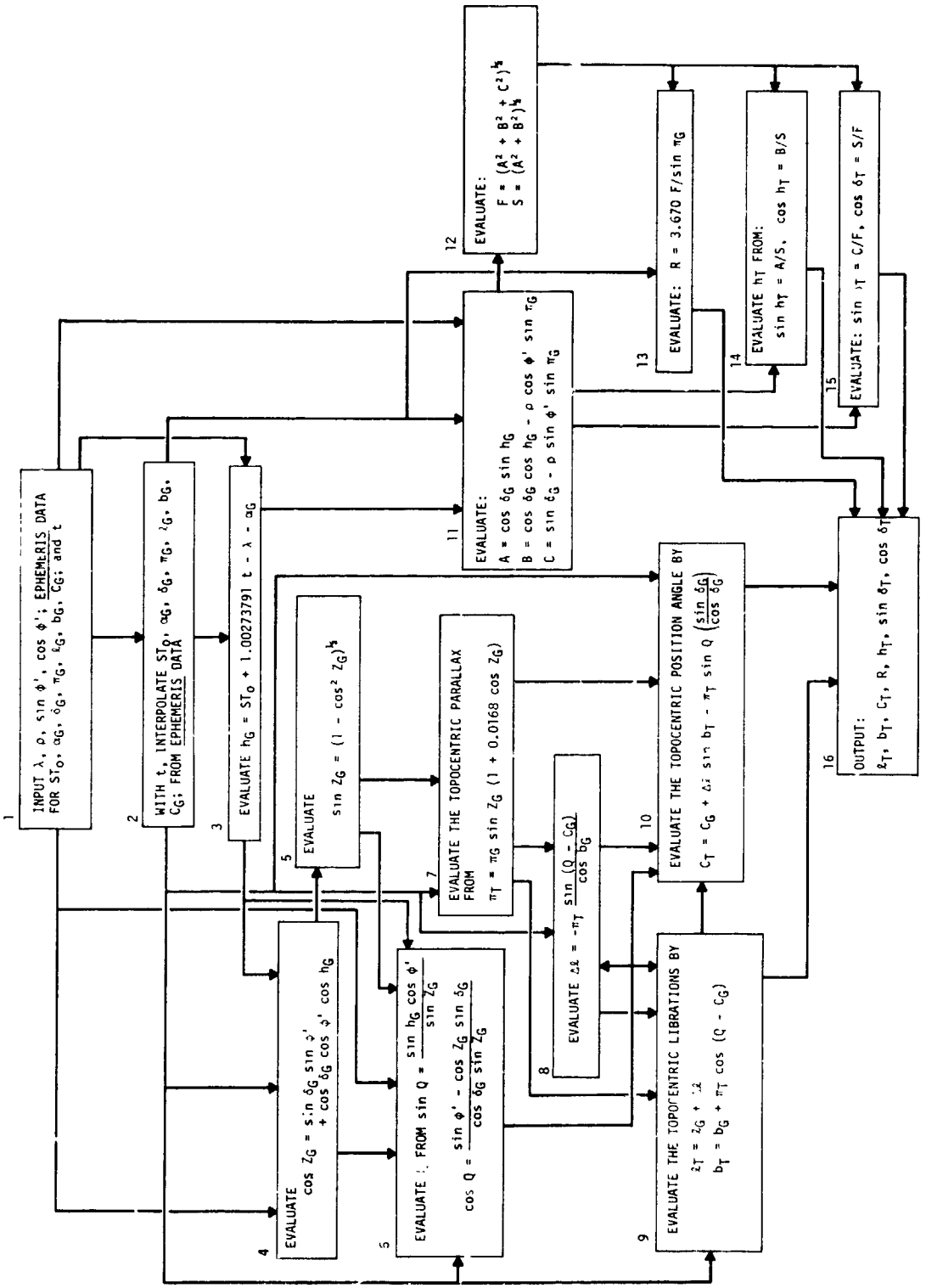

FIGURE 4-2. TOPOCENTRIC EPHEMERIS ROUTINE

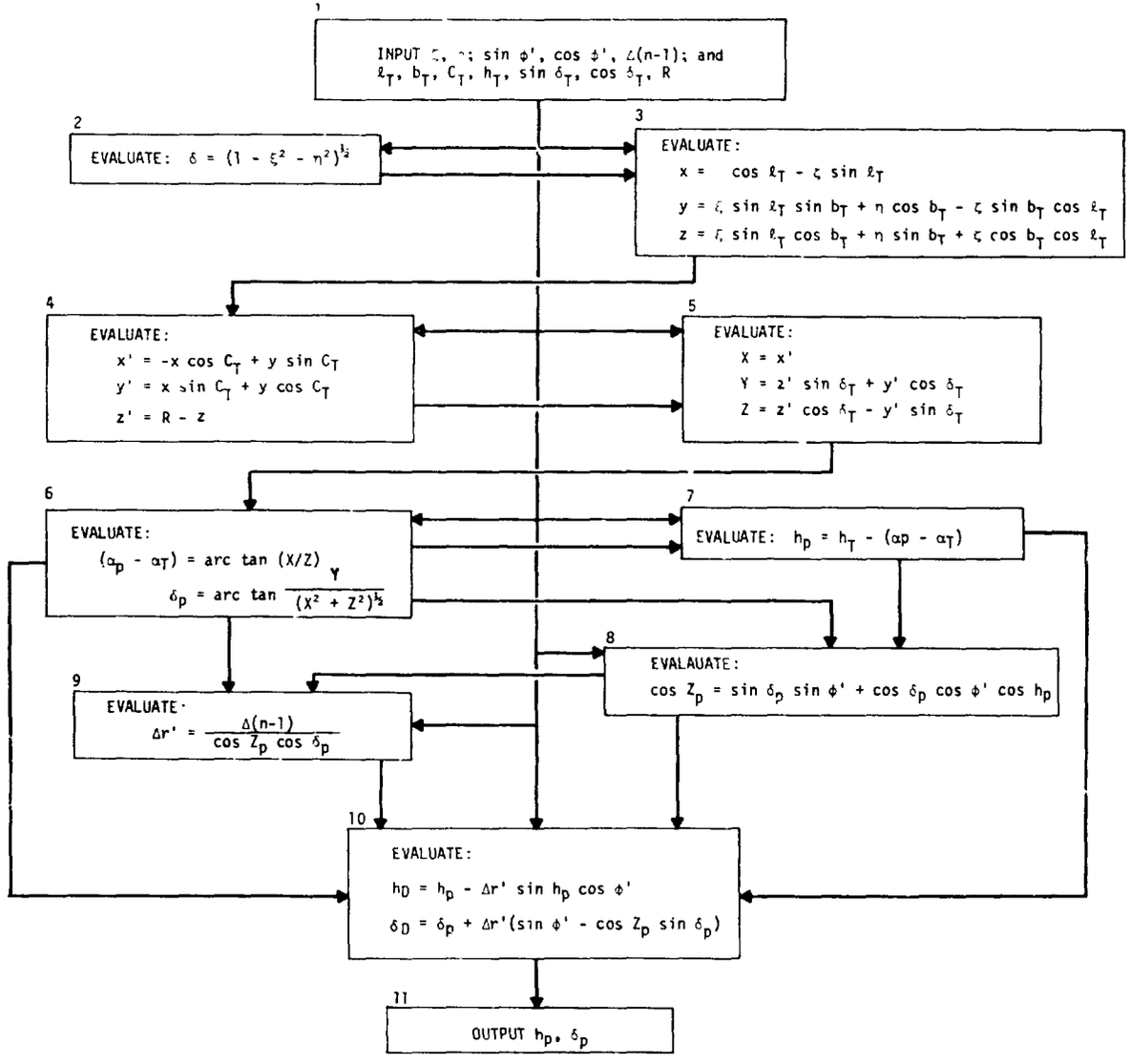

FIGURE 4-3. TOPOCENTRIC COORDINATES ROUTINE

coordinates seen by the infrared detector by taking differential refraction into account.

The air mass routine, shown in Figure 4-4, takes as input these topocentric detector coordinates and the sine and cosine of the observer's latitude. A calculation of the secant of the zenith angle is performed, and this is followed by a correction for curvature of the atmosphere and refraction. Correction for altitude is not needed for the method of atmospheric attenuation correction used in the program.

The basic program is outlined in Figures 4-5 through 4-9. The first step is the calculation of the attenuation coefficient, shown in Figure 4-5. The computer selects all of the extinction point files and corresponding sky files. Also input are the ephemeral data, coordinates describing the observer location, and the lunar orthographic coordinates and temperatures of the lunar surface extinction points. The air mass values for the observations are computed following recourse to the topocentric ephemeris routine, the topocentric coordinates routine, and the air mass routine. The attenuation coefficient k_1 or k_2 is obtained by fitting a line by the least squares method to the data according to Equation 4-13 for observations at 10 micrometers and according to Equation 4-14 for observations at 20 micrometers. These equations correspond to the weak and strong random line absorption band approximations, respectively.

The next step of the program is the calculation of the calibration constants. This is shown in Figure 4-6. Two calibration constants are calculated, one each for the beginning and end of the evening. Corresponding times are also obtained for the beginning and end of the evening, so that each value of the calibration constant used in the program may be time-interpolated. This portion of the program is entered with the calibration and sky files for the beginning and end of the evening, data describing the location of the observer, and the lunar orthographic

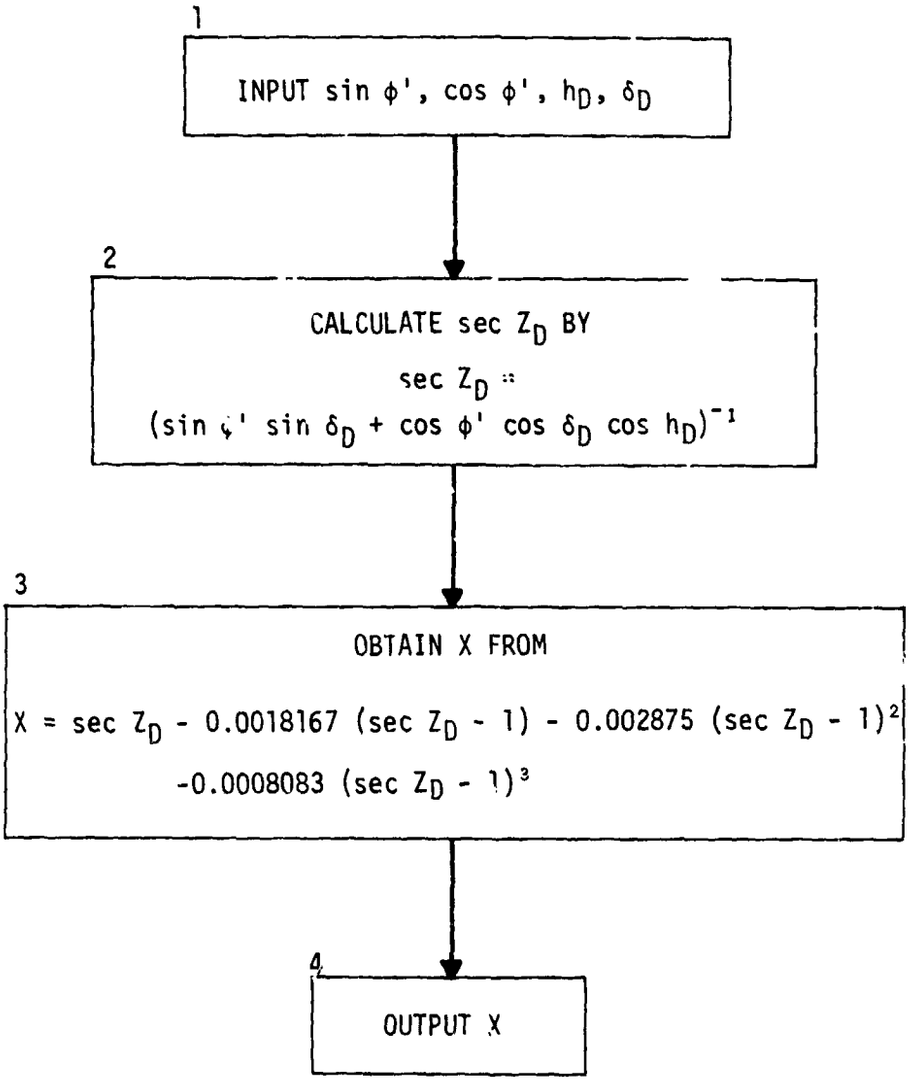

FIGURE 4-4. AIR MASS ROUTINE

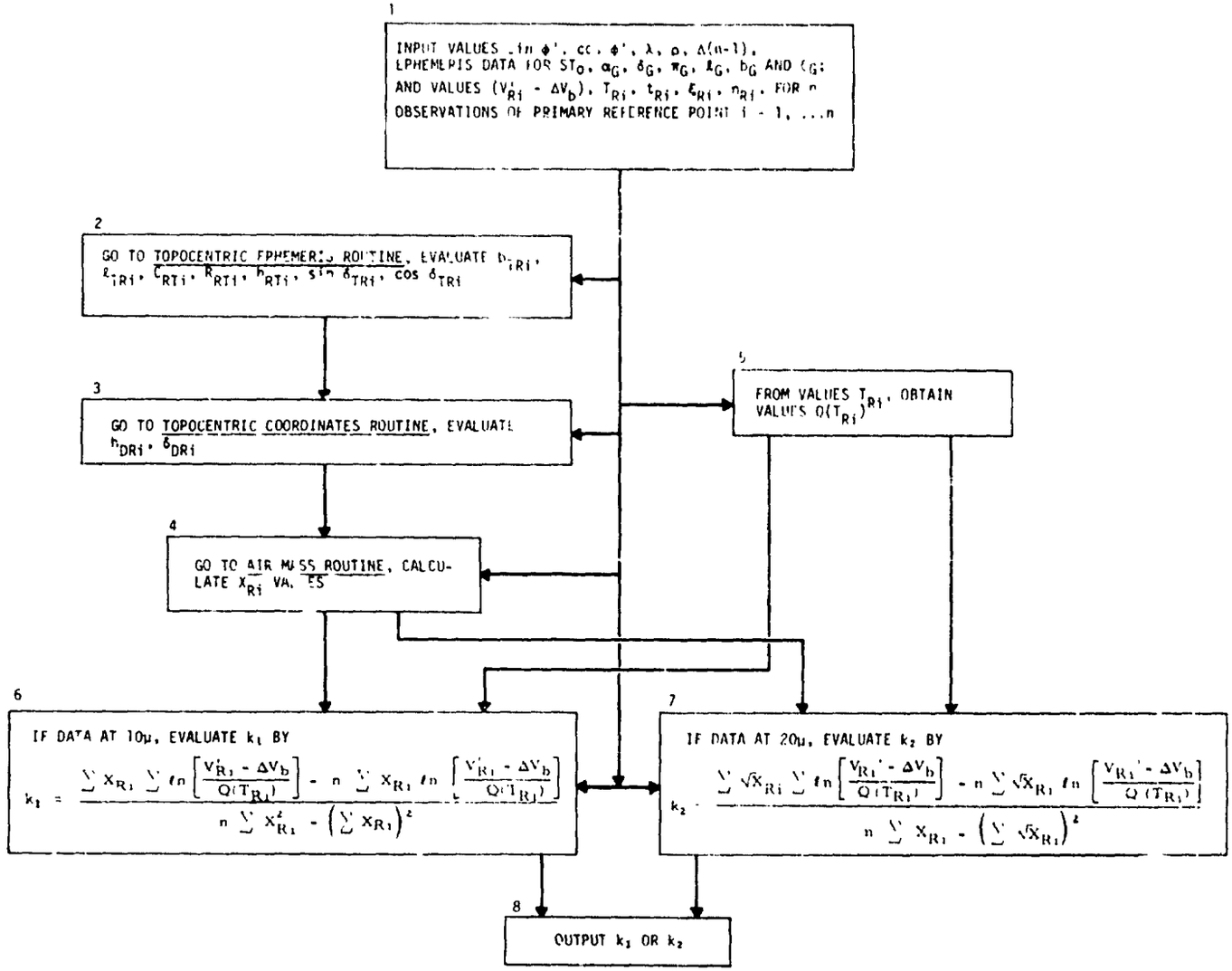

FIGURE 4-5. ATTENUATION COEFFICIENT PROGRAM

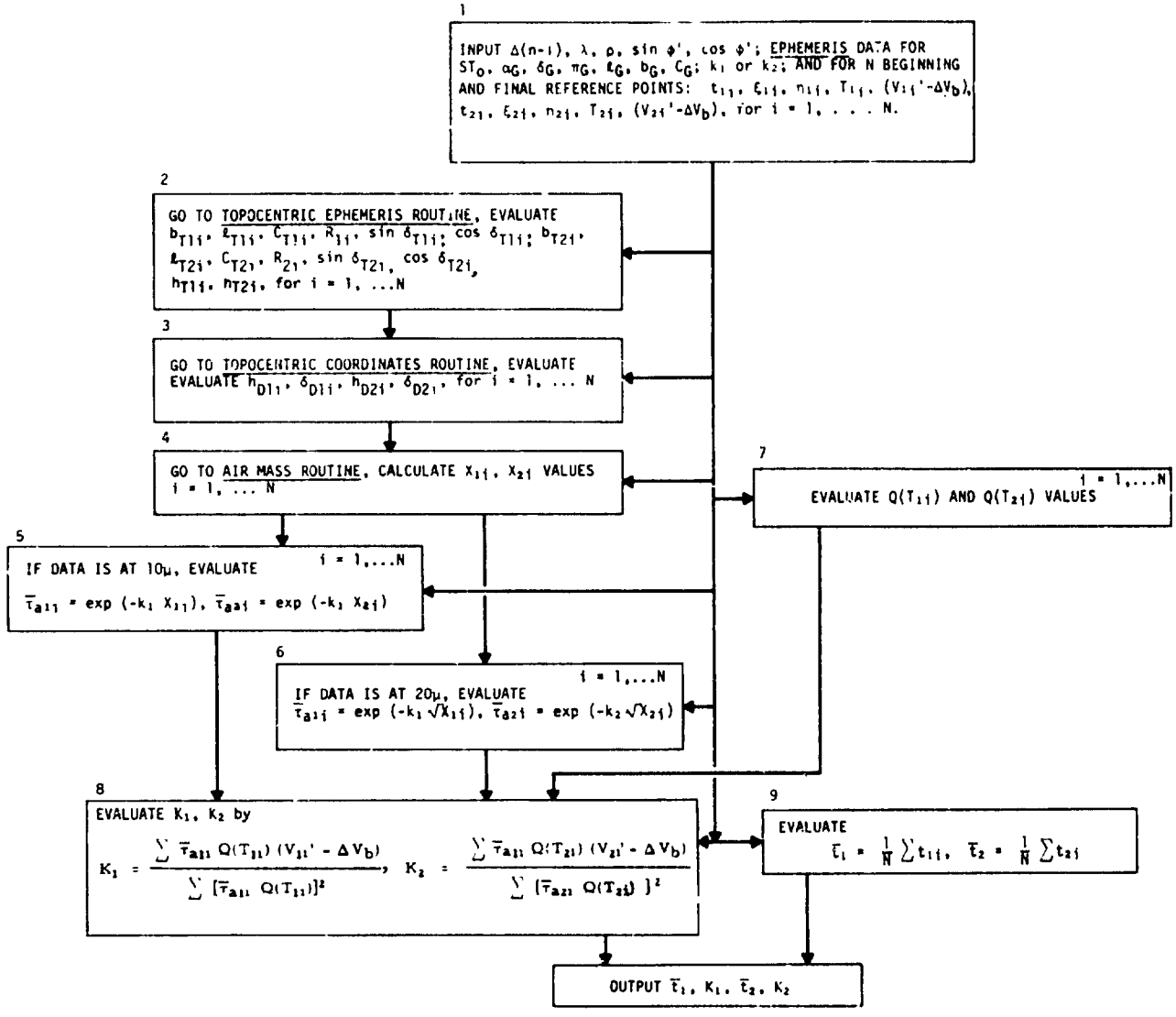

FIGURE 4-6. CALIBRATION PROGRAM

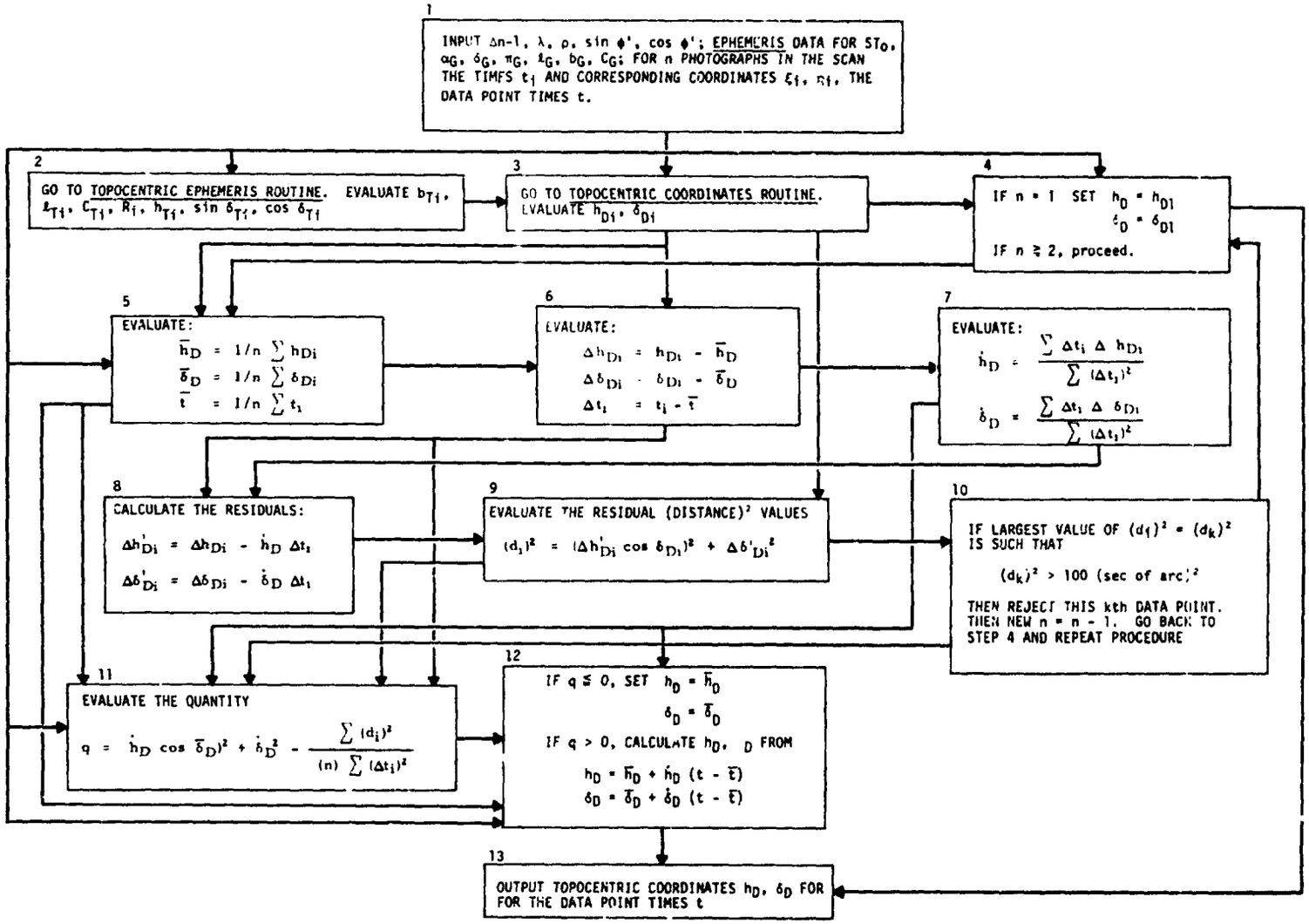

FIGURE 4-7. SCAN REDUCTION PROGRAM I, CALCULATION OF TOPOCENTRIC COORDINATES OF DATA POINTS

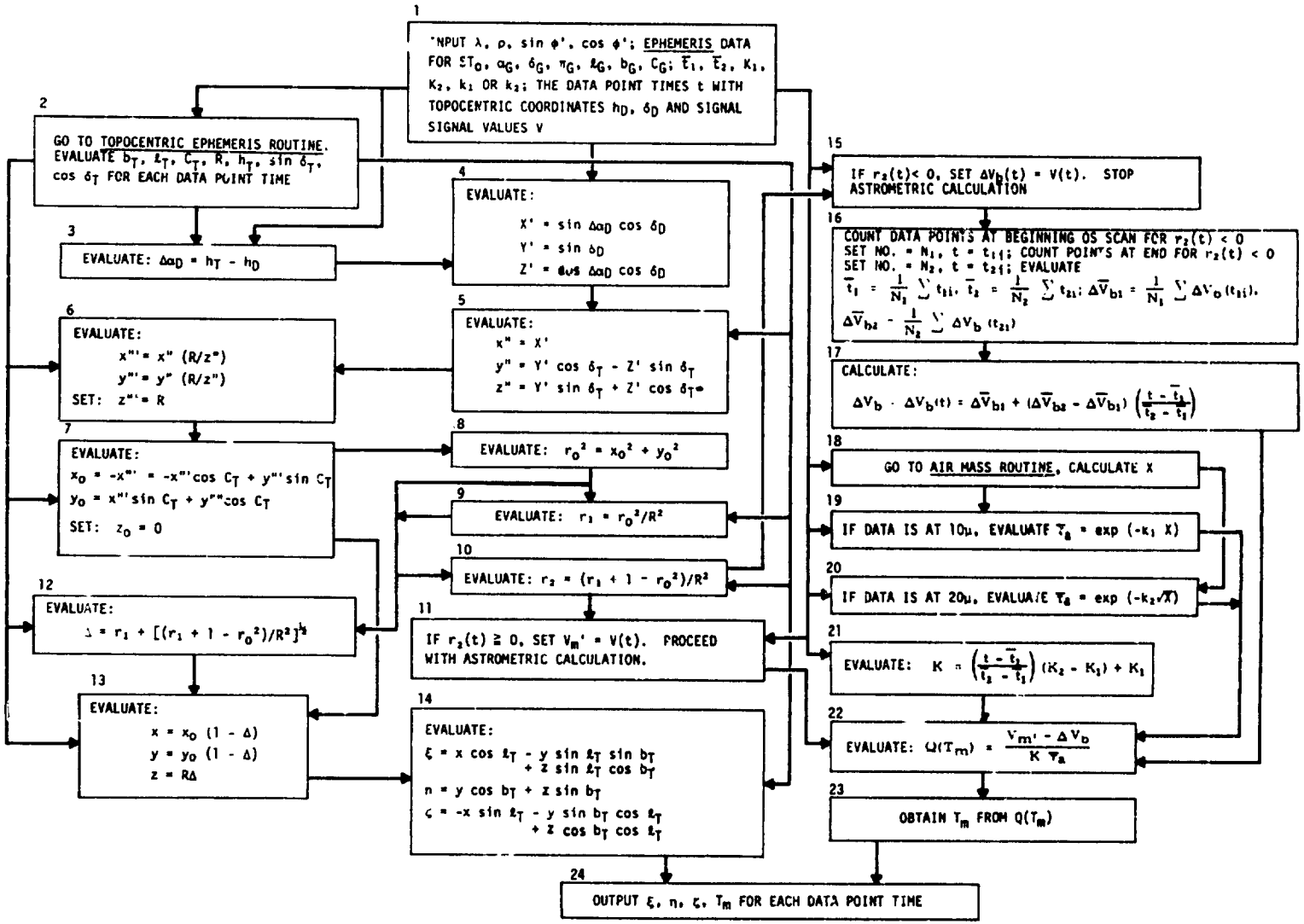

FIGURE 4-8. SCAN REDUCTION PROGRAM II, CALCULATION OF ORTHOGRAPHIC COORDINATES AND TEMPERATURES OF OBJECT POINTS

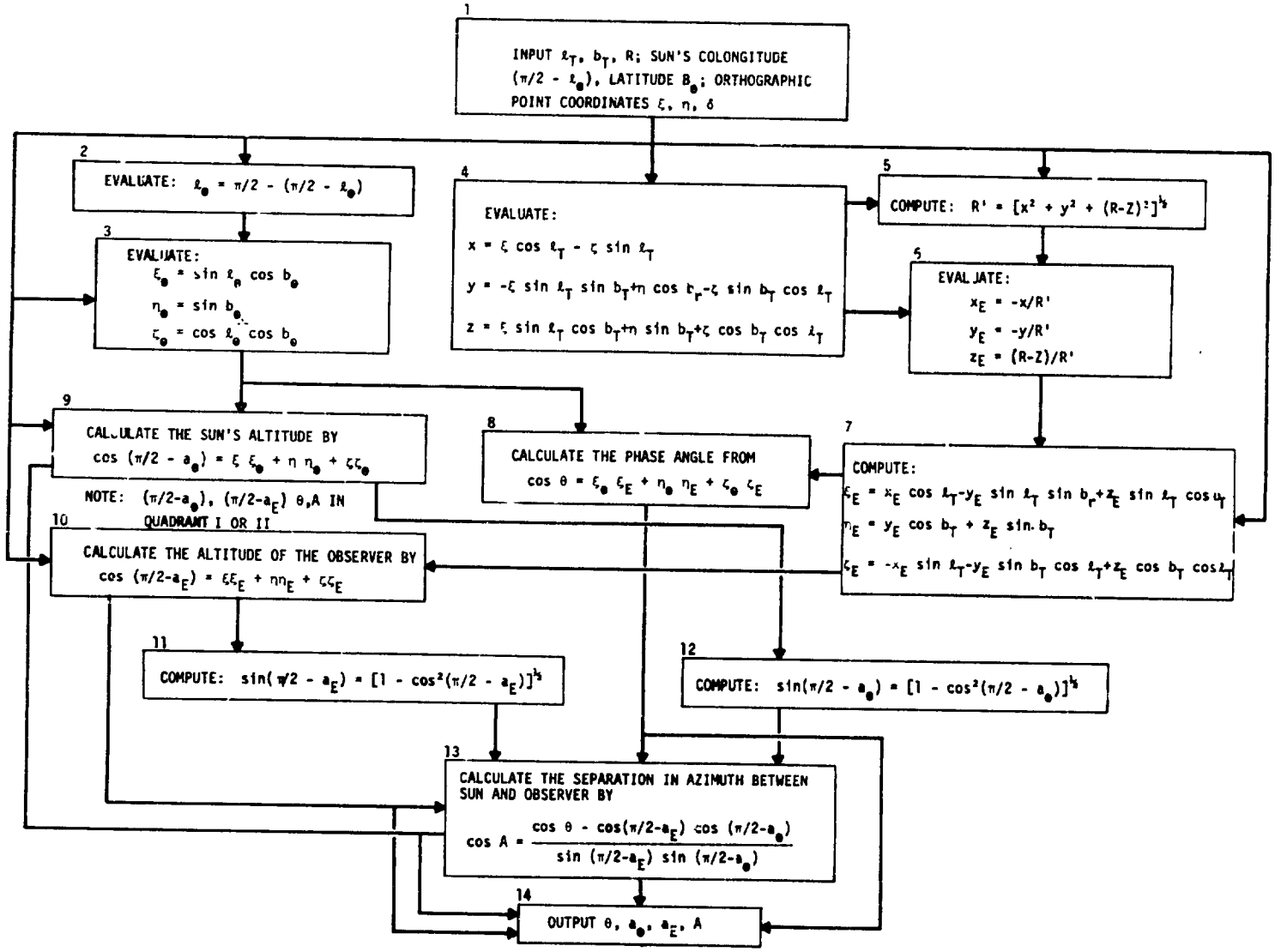

FIGURE 4-9. ILLUMINATION - RADIATION PARAMETERS PROGRAM

coordinates and temperatures for the chosen lunar surface calibration points. Air mass values are computed following use of the topocentric ephemeris routine, the topocentric coordinates routine, and the air mass routine. The attenuation coefficient obtained in the proceding step is used with the air mass values for determination of atmospheric transmission values. The values of K are next obtained by evaluation of Equation 4-15. The corresponding times are averages over the times of the calibration files.

Each lunar disc scan is handled separately; Figure 4-7 shows the first phase of the scan reduction. This phase describes the calculation of the topocentric coordinates of the object points in the scan. The section begins with the calculation of the topocentric hour angle and declination coordinates of the detector field at the times of the photographs in the scan. If there is only one photograph, the program assumes no telescope motion. If more than one photograph has been recorded, the program calculates the rates of telescope motion in hour angle and declination, with the assumption that these rates are uniform. From each set of coordinates, residual distance values are calculated, and these are tested for erroneous coordinates. If any such point is found having a residual distance from the predicted position more than 10 arcseconds, this point is rejected and the procedure is again performed with the remaining points. Finally, the data are tested for telescope motion by comparison of the derived rates with the standard deviations in these rates, as obtained from the calculated residuals. For no telescope motion, the topocentric coordinates during the scan are taken as averages of the coordinates computed from the photographs. If telescope motion is included, the topocentric data point coordinates are computed from their times and the derived motion.

Figure 4-8 shows the calculation of the orthographic coordinates of the object points and their temperatures from the observational

data. The transformation from topocentric coordinates to lunar orthographic coordinates is not a strict reversal of the topocentric coordinates routine, since the direction to an object point is known and not its distance. After calling the topocentric ephemeris routine, the topocentric coordinates of an object point are transformed through three successive sets of rectangular coordinates to a set x_o, y_o, z_o. This system has its origin at the lunar center, with the z_o axis passing through the observer, the y_o axis in the plane of the north lunar pole, and the x_o axis directed westward. The coordinates calculated are of the intersection of the line of sight with the x_o, y_o plane. By assumption of a spherical Moon, the coordinates x, y, z of the intersection of the line of sight with the lunar surface in the x_o, y_o, z_o system are obtained. An auxiliary quantity r_2 is calculated and provides a test for the intersection of the line of sight with the Moon. If, as a result of this test, the line of sight does not intersect the Moon, the astrometric calculation is stopped and the associated signal value is added to the values of sky background. For points on the lunar surface, the orthographic coordinates are obtained by transformation from the coordinates x, y, z.

The readings of sky signal at each end of a scan are treated separately. Each of these groups is averaged, and an average time is computed for each. These values are then used for performance of a linear interpolation of sky signal throughout the scan, which is used for the lunar signal correction. After calling the air mass routine, the atmospheric transmission value at each object point is computed. The final step of this phase of the program is the calculation of the temperature by Equation 4-16. The value of T is obtained from the function Q(T) by a recursive routine. The temperature adjustment previously described is then calculated.

From quantities already determined, it is convenient, at this time, to calculate additional quantities which may be useful for a future study of directional effects of illumination and reradiation. Since the radiometer includes a facility for photometry in the visual region, consideration of scattering of sunlight from the surface is included. Solar heating is primarily due to the solar altitude, and heat radiation may depend upon altitude. Scattered sunlight depends also upon the phase angle and azimuth difference. The calculation begins with the orthographic coordinates of the subsolar and subobserver points being evaluated, as shown in blocks 3 and 7 of Figure 4-9. These coordinates, together with the orthographic coordinates for each object point, are used for the calculation of the altitudes of the Sun and Earth, the phase angle, and the difference in azimuth between the Sun and Earth at each object point.

5. RESULTS

To date, the computer reduction has been completed for data recorded on fourteen evenings in 1971 and 1972. Two of these sets may contain too few measurements to carry beyond the computer reduction stage. In two other sets the data were degraded by clouds. The result of the remaining ten sets are presented in this section.

The computer printout of a typical lunar scan is shown in Figure 5-1. The columns from left to right show the time in seconds, the topocentric detector hour angle and declination in radians, the lunar orthographic coordinates, ξ, η, and ζ, the temperature, the adjusted temperature, the air mass, and four angular quantities measured at the observed point in radians. These are the angle between the Sun and Earth, the solar zenith angle, the Earth's zenith angle, and the difference in azimuth between the Sun and Earth.

The results of the project are generally too extensive for inclusion of this form of printout for the entire mass of data. A convenient form for presentation is as a set of isothermal contour maps. Such maps have been constructed by hand from the data of November 5, and 8, January 16, September 11, 12, and 14, 1971, and September 29 and 30, and October 1 and 2, 1972. These maps are shown in Figures 5-2 through 5-11. The data of the September and October evenings were recorded with the 1.5 meter telescope in Arizona; the other three sets were recorded with the 0.3 meter telescope in Huntsville. Measurements for these maps were made in the 10.0- to 12.5-micrometer band. and the number of data points used for each full disc map is of the order of 4,200.

For the Huntsville data, the detector size of 0.5 mm diameter indicates the maximum resolution at 22.5 arc seconds.

TIME	MD	UD	ORTHOGRAPHIC COORDINATES			TEMP	TEMPA	AMV	SOLAR DATA			
26721.	6.18	0.46	0.407	-0.913	-0.030	153.8	163.8	1.01	0.59	1.76	1.48	0.54
26722.	6.18	0.46	0.396	-0.918	0.011	156.4	166.1	1.01	0.59	1.74	1.44	0.54
26724.	6.18	0.46	0.383	-0.923	0.042	159.6	169.0	1.01	0.59	1.69	1.41	0.54
26725.	6.18	0.46	0.370	-0.927	0.066	162.8	171.8	1.01	0.59	1.66	1.39	0.54
26726.	6.18	0.46	0.356	-0.930	0.087	166.0	174.7	1.01	0.59	1.63	1.37	0.53
26727.	6.18	0.46	0.342	-0.934	0.105	171.8	179.7	1.01	0.59	1.61	1.35	0.53
26728.	6.18	0.46	0.328	-0.937	0.120	177.7	185.0	1.01	0.59	1.59	1.34	0.53
26730.	6.18	0.46	0.314	-0.940	0.134	182.0	188.7	1.01	0.59	1.57	1.32	0.54
26731.	6.18	0.46	0.299	-0.943	0.146	187.4	193.4	1.01	0.59	1.55	1.31	0.54
26732.	6.18	0.46	0.284	-0.946	0.157	200.6	205.0	1.01	0.59	1.54	1.30	0.55
26733.	6.18	0.46	0.270	-0.948	0.167	218.3	221.2	1.01	0.59	1.52	1.29	0.55
26734.	6.18	0.46	0.255	-0.951	0.175	229.3	231.7	1.01	0.59	1.51	1.29	0.56
26736.	6.18	0.46	0.240	-0.954	0.183	237.0	239.1	1.01	0.59	1.49	1.28	0.56
26737.	6.18	0.46	0.224	-0.956	0.189	244.0	245.9	1.01	0.59	1.48	1.27	0.56
26738.	6.18	0.46	0.209	-0.958	0.195	253.3	254.9	1.01	0.59	1.47	1.27	0.57
26739.	6.18	0.46	0.194	-0.961	0.199	257.3	256.8	1.01	0.59	1.46	1.27	0.57
26741.	6.18	0.46	0.178	-0.963	0.203	255.7	257.2	1.01	0.59	1.45	1.27	0.57
26742.	6.18	0.46	0.163	-0.965	0.206	261.8	263.2	1.01	0.59	1.44	1.26	0.58
26743.	6.18	0.46	0.147	-0.967	0.208	268.1	269.3	1.01	0.59	1.43	1.26	0.58
26744.	6.18	0.46	0.131	-0.969	0.209	270.2	271.4	1.01	0.59	1.42	1.26	0.58
26745.	6.18	0.46	0.116	-0.971	0.210	273.2	274.3	1.01	0.59	1.41	1.26	0.59
26747.	6.18	0.46	0.100	-0.973	0.210	274.9	275.9	1.01	0.59	1.40	1.27	0.59
26748.	6.18	0.46	0.084	-0.974	0.208	276.2	277.2	1.01	0.59	1.40	1.27	0.59
26749.	6.18	0.46	0.068	-0.976	0.206	278.4	279.4	1.01	0.59	1.39	1.27	0.59
26750.	6.18	0.46	0.051	-0.978	0.203	282.7	283.5	1.01	0.59	1.39	1.28	0.60
26751.	6.18	0.46	0.035	-0.979	0.199	286.6	287.4	1.01	0.59	1.38	1.28	0.60
26753.	6.18	0.46	0.019	-0.981	0.194	287.2	287.9	1.01	0.59	1.38	1.29	0.60
26754.	6.18	0.46	0.002	-0.982	0.188	288.6	289.4	1.01	0.59	1.38	1.30	0.60
26755.	6.18	0.46	-0.014	-0.983	0.181	290.8	291.4	1.01	0.59	1.38	1.31	0.60
26756.	6.18	0.46	-0.031	-0.985	0.172	290.5	291.1	1.01	0.59	1.38	1.32	0.60
26757.	6.18	0.46	-0.048	-0.986	0.162	291.6	292.2	1.01	0.59	1.38	1.33	0.60
26759.	6.18	0.46	-0.065	-0.986	0.151	294.1	294.7	1.01	0.59	1.38	1.34	0.60
26760.	6.18	0.46	-0.083	-0.987	0.137	292.3	291.8	1.01	0.59	1.38	1.36	0.60
26761.	6.18	0.46	-0.100	-0.988	0.121	287.5	286.9	1.01	0.59	1.39	1.38	0.60
26762.	6.18	0.46	-0.118	-0.988	0.101	283.6	282.9	1.01	0.59	1.40	1.40	0.60
26763.	6.18	0.46	-0.137	-0.988	0.076	274.0	273.3	1.01	0.59	1.41	1.43	0.60
26765.	6.18	0.46	-0.157	-0.987	0.044	262.1	261.2	1.01	0.59	1.43	1.46	0.59
26766.	6.18	0.46	-0.179	-0.984	-0.013	249.2	248.1	1.01	0.59	1.47	1.52	0.59

FIGURE 5-1. COMPUTER PRINTOUT FOR A TYPICAL LUNAR DISC SCAN OF NOVEMBER 5, 1971

FOLDOUT FRAME

ISOTHERMAL LUNAR MAP FOR A CONTOUR SPACING OF 10 K°, THE COORDINATE SYSTEM IS THE STANDARD ORTHOGRAPHIC GRID. FROM RADIOMETRIC MEASUREMENTS TAKEN AT HUNTSVILLE, ALABAMA, AT 8.5 M.T., ON NOVEMBER 5, 1971, IN THE 10.0 μ - 12.5 μ BAND.

SOLAR SELENOGRAPHIC COLONGITUDE 116°

TEMPERATURES IN °K

⊕ SUBSOLAR POINT

⊕ APPARENT DISC CENTER DURING OBSERVATION

— — — TERMINATOR

NOISE TEMPERATURE 105 °K

○ DETECTOR SIZE

ADVANCE DIRECTION

SCAN DIRECTION

○ EFFECTIVE RESOLUTION AREA (BASED ON 9400 DATA POINTS)

53 SCANS

FOLDOUT FRAME

2

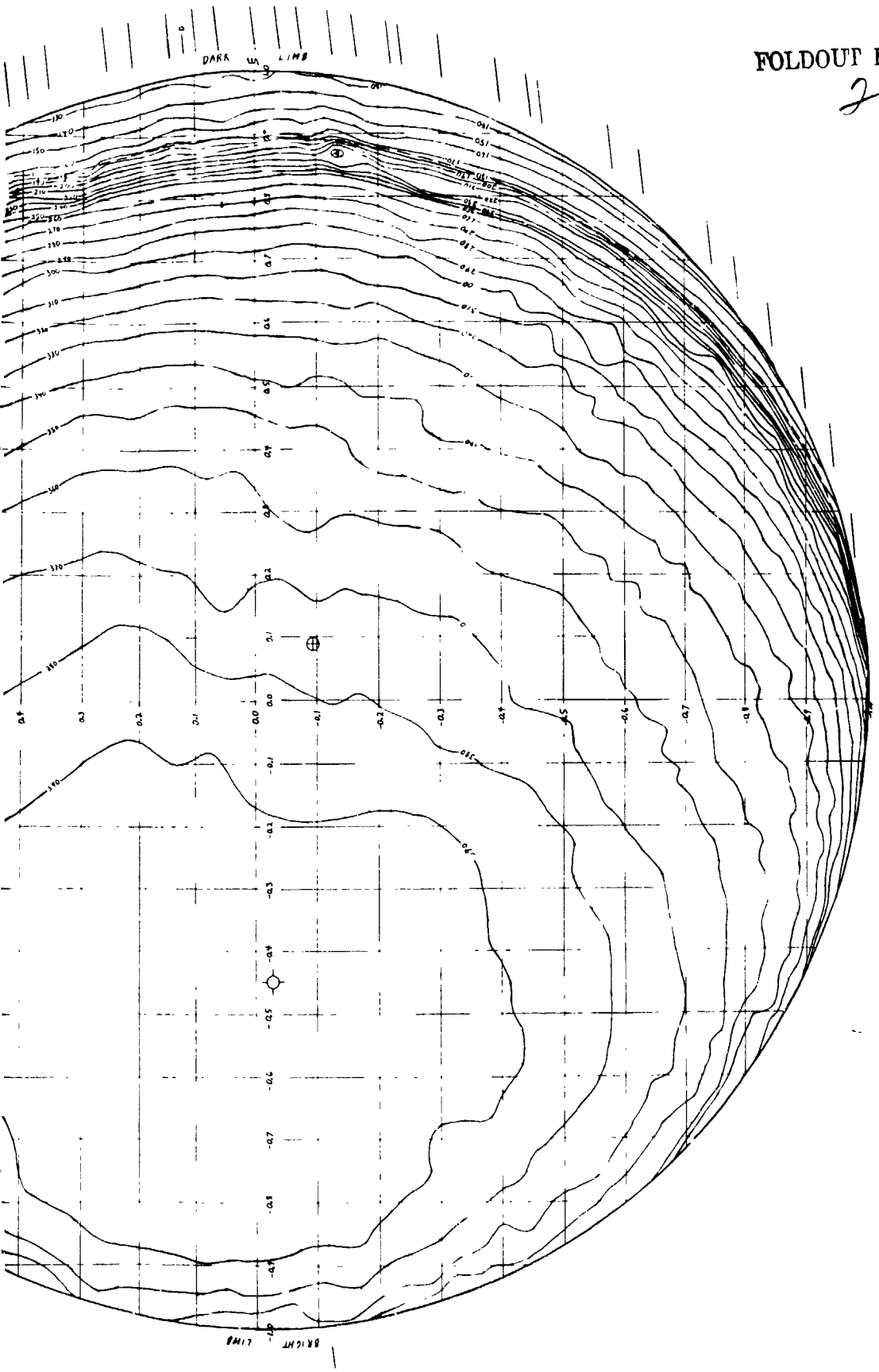

FIGURE 5-2. ISOTHERMAL LUNAR MAP FOR A SOLAR SELENOGRPAHIC COLONGITUDE OF 116 DEGREES

FOLDOUT FRAME

ISOTHERMAL LUNAR MAP FOR A CONTOUR SPACING OF 10 R°. SUCH AN EQUAL TEMPERATURE INCREMENT CONTOUR SPACING BEST ILLUSTRATES TEMPERATURE GRADIENTS OVER THE LUNAR SURFACE. THE COORDINATE GRID IS THE ORTHOGRAPHIC SYSTEM (FROM RADIOMETRIC MEASUREMENTS TAKEN AT HUNTSVILLE, ALABAMA ON JANUARY 16, 1971, AT 6^h U.T., IN THE 10.0μ - 12.5μ BAND).

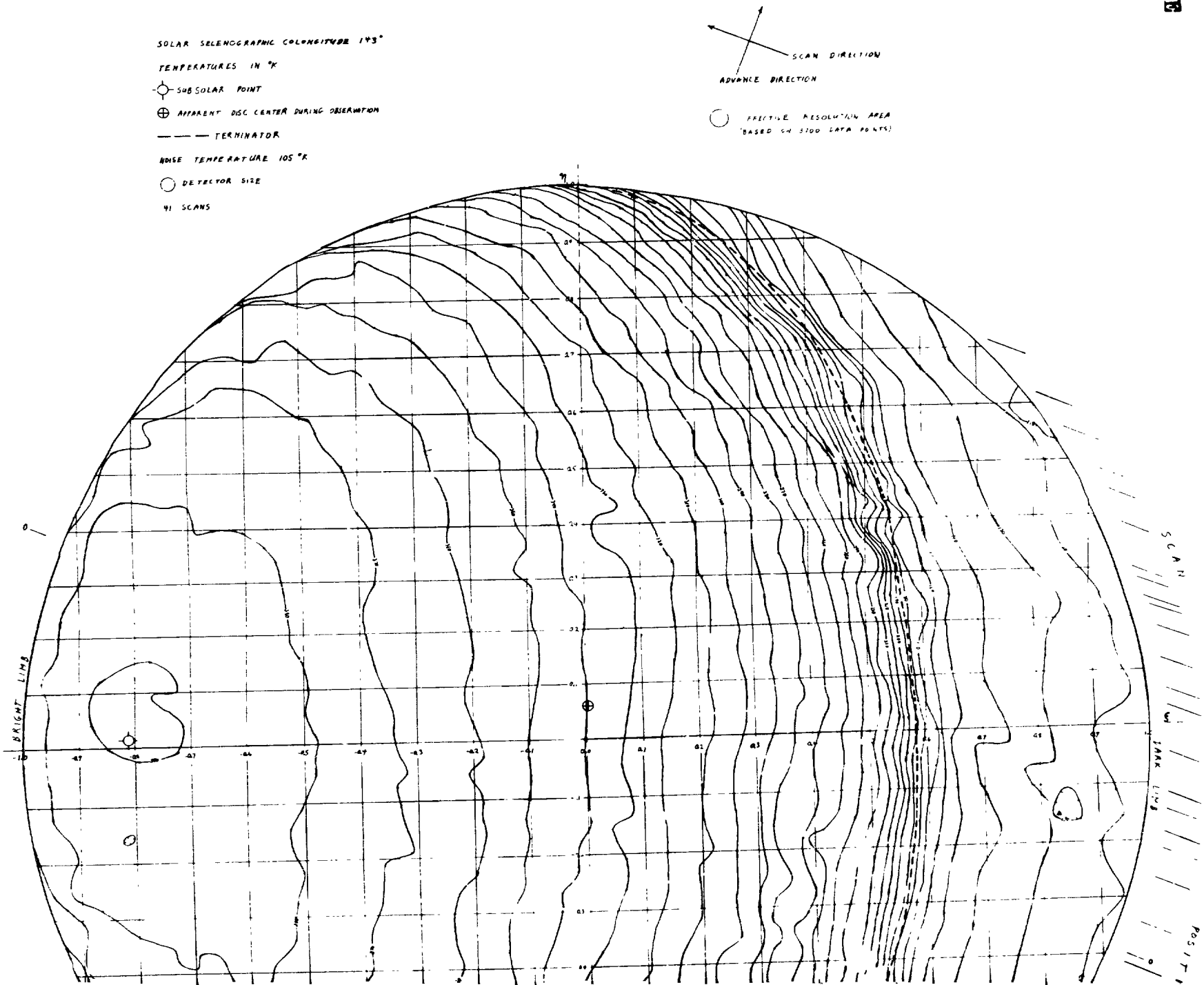

FOLDOUT FRAME

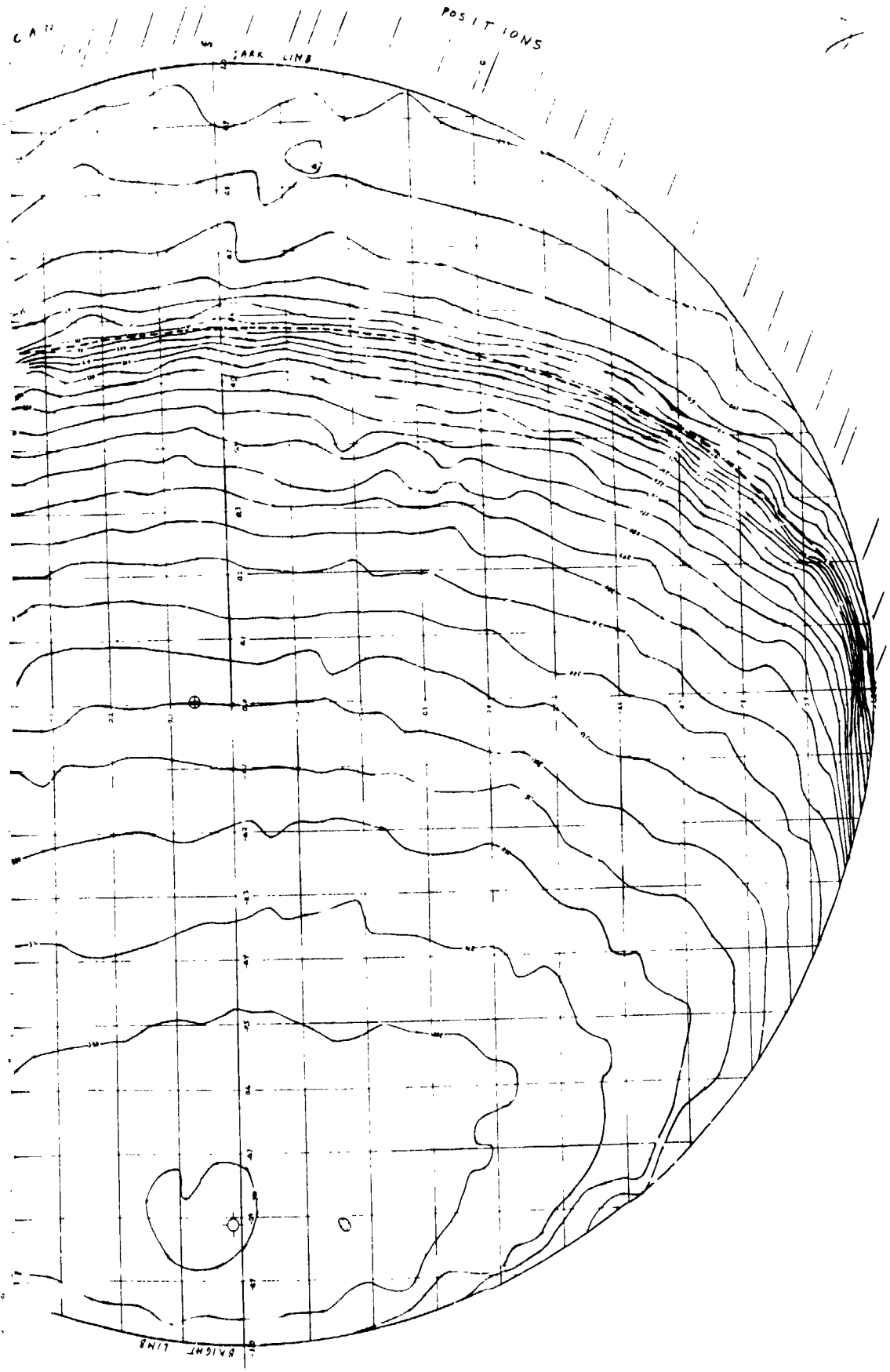

FIGURE 5-3. ISOTHERMAL LUNAR MAP FOR A SOLAR SELENOGRAPHIC COLONGITUDE OF 143 DEGREES

FOLDOUT FRAME

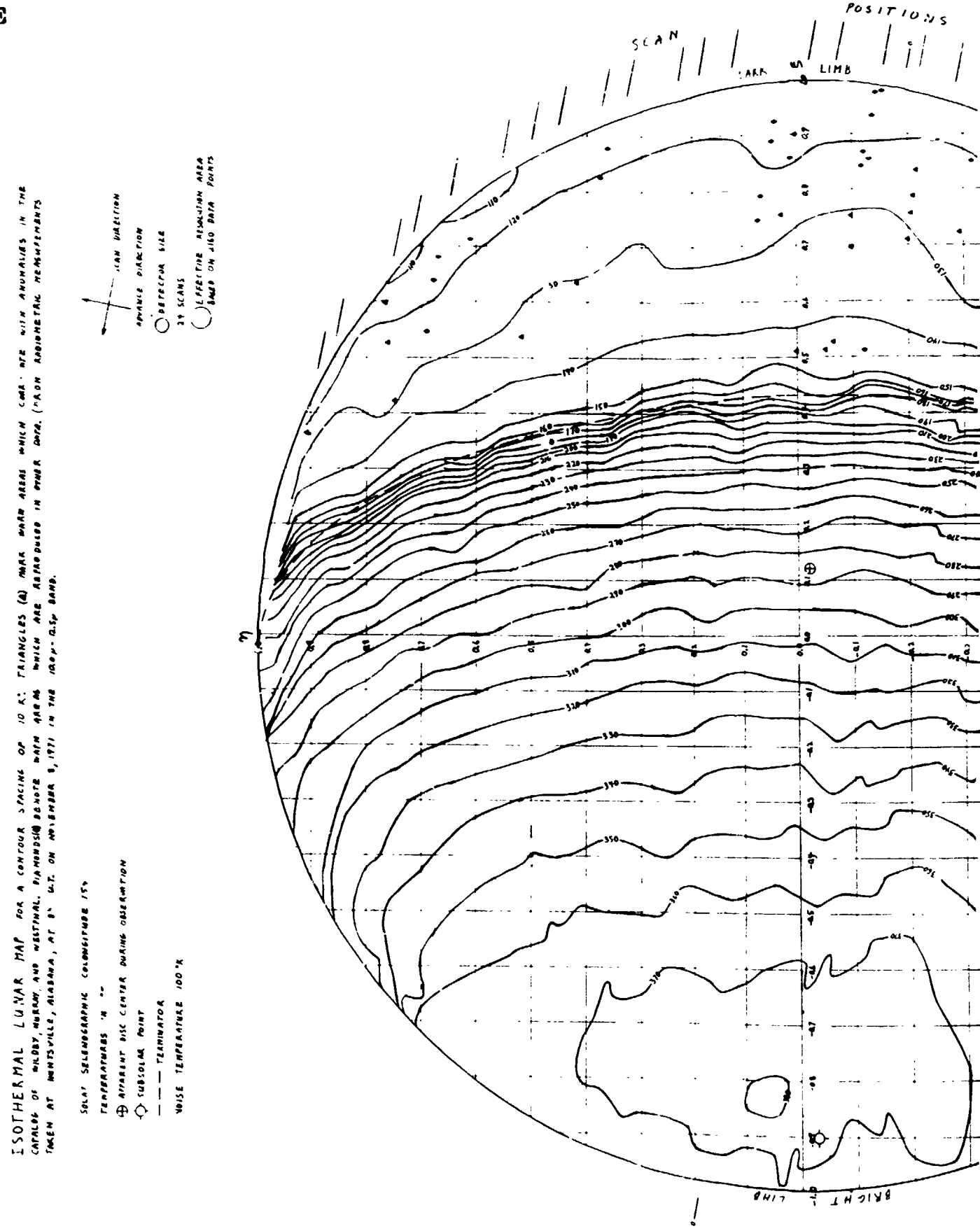

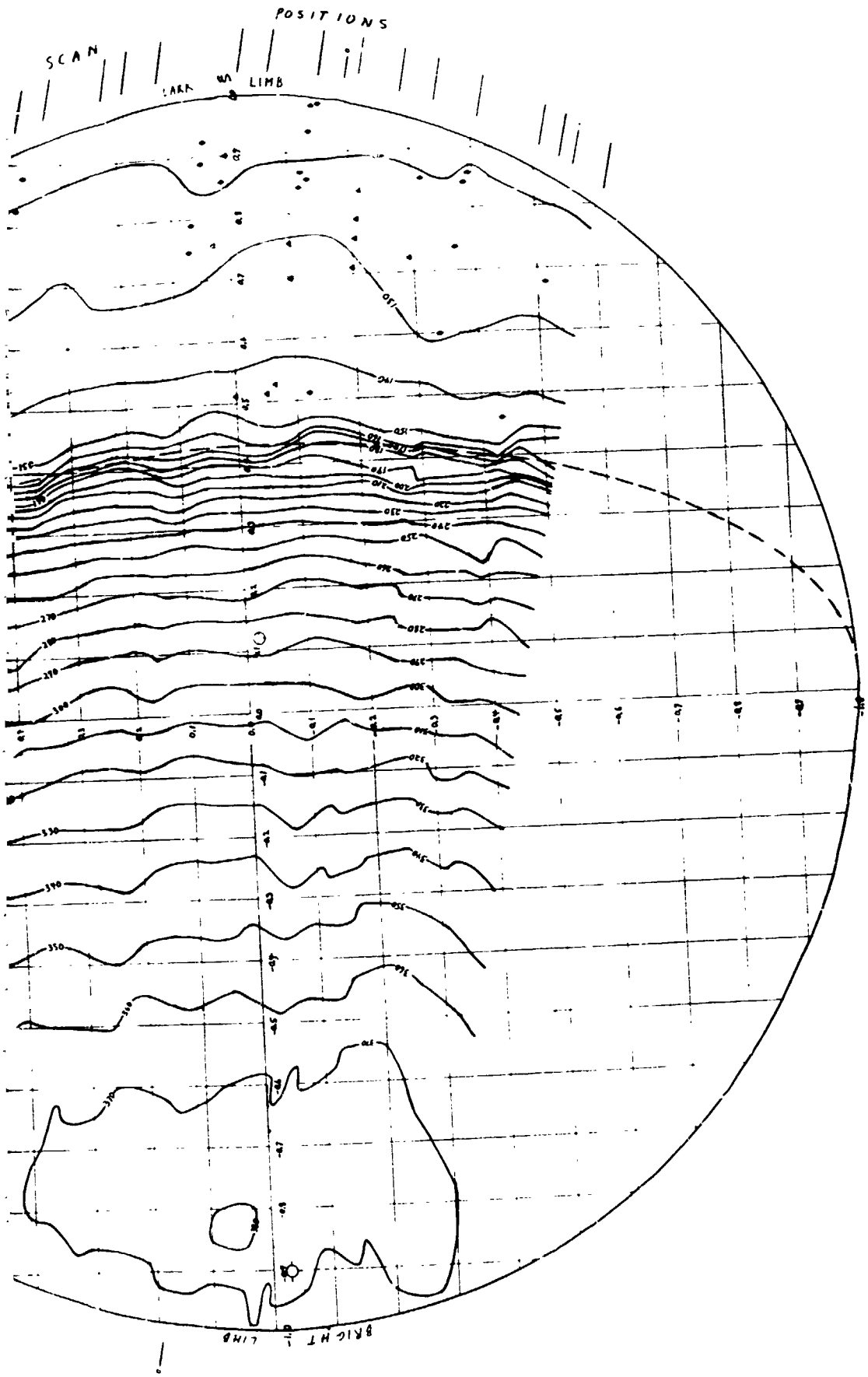

FIGURE 5-4. ISOTHERMAL LUNAR MAP FOR A SOLAR SELENOGRAPHIC COLONGITUDE OF 154 DEGREES

FOLDOUT FRAME

ISOTHERMA LUNAR MAP FOR A FULL-YEAR SPACING OF 10 AT TRIANGLES (a) HAS MANY AREAS WHICH CORRELATE WITH ANOMALIES IN THE CATALOG OF WILDEY, MURRAY AND WESTPHAL. DIAMONDS (◇) DENOTE AREAS WHICH ARE REDISCUSSED IN OTHER DATA, FROM RADIOMETRIC MEASUREMENTS TAKEN AT LOWELL STATION OBSERVATORY, FLAGSTAFF, ARIZONA, AT 9" O.T., ON SEPTEMBER 11, 1961. THE 10" x 13" SCALE

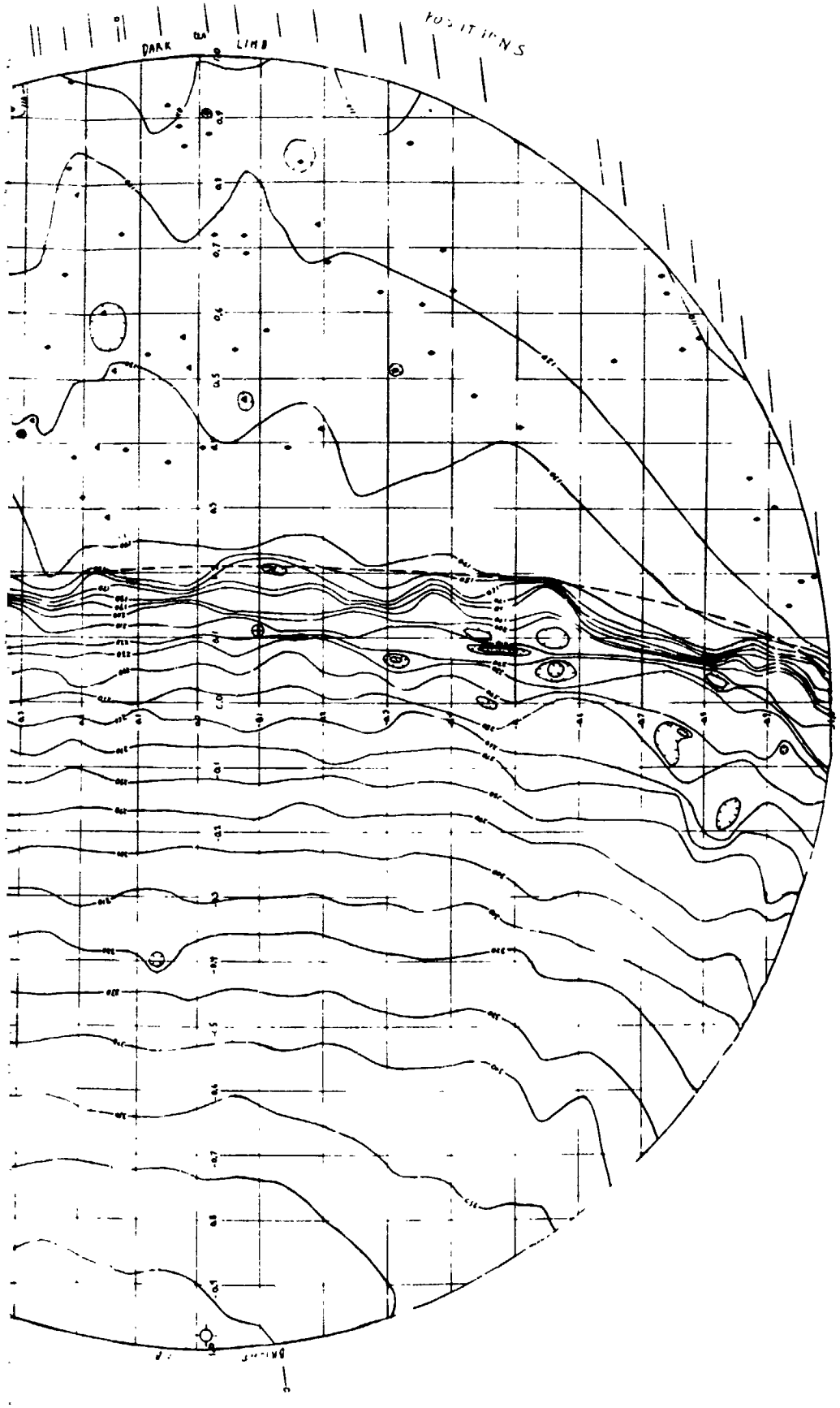

FIGURE 5-5. ISOTHERMAL LUNAR MAP FOR A SOLAR SELENOGRAPHIC COLONGITUDE OF 168 DEGREES

ISOTHERMAL LUNAR MAP FOR A CONTOUR SPACING OF 10 K° TRIANGLES (▲) DENOTE WARM AREAS WHICH CORRELATE WITH ANOMALIES IN THE CATALOG OF WILDEY, MURRAY, AND WESTPHAL. DIAMONDS (◆) MARK WARM AREAS WHICH CORRELATE WITH SIMILAR AREAS IN OTHER DATA. THE COORDINATE SYSTEM IS THE STANDARD ORTHOGRAPHIC GRID. (FROM RADIOMETRIC MEASUREMENTS TAKEN AT CATALINA STATION OBSERVATORY, ARIZONA AT 10.6° U.T. ON SEPTEMBER 29, 1972 IN THE 10.0μ – 12.5μ BAND.)

SOLAR SELENOGRAPHIC COLONGITUDE 170°

TEMPERATURES IN °K

NOISE TEMPERATURE 100°K

⊙ SUBSOLAR POINT

⊕ APPARENT DISC CENTER DURING OBSERVATION

+1 SCANS

MOVABLE DIRECTION

SCAN DIRECTION

○ DETECTOR SIZE

◯ EFFECTIVE RESOLUTION AREA (BASED ON 3700 DATA POINTS)

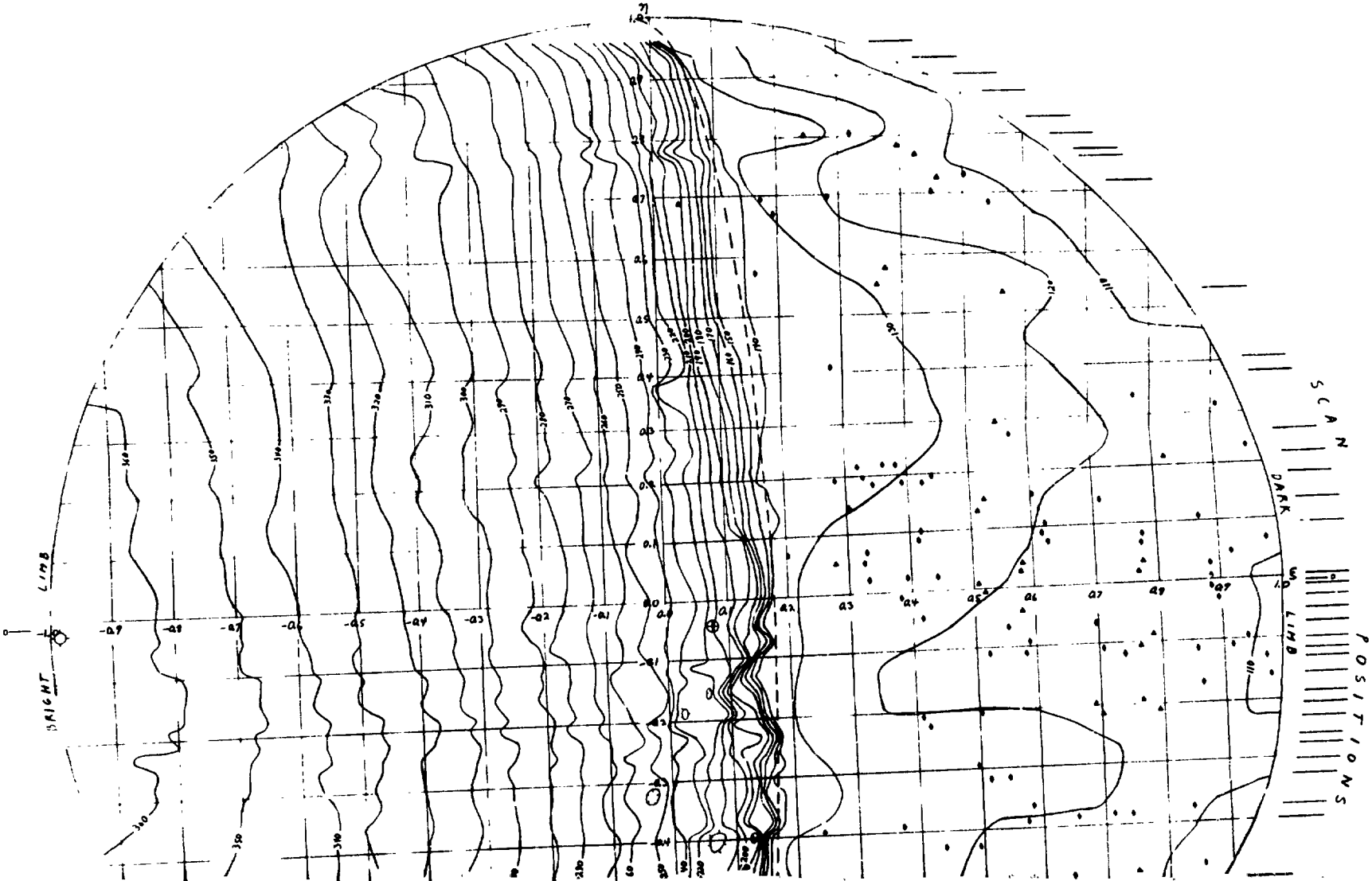

FOLDOUT FRAME

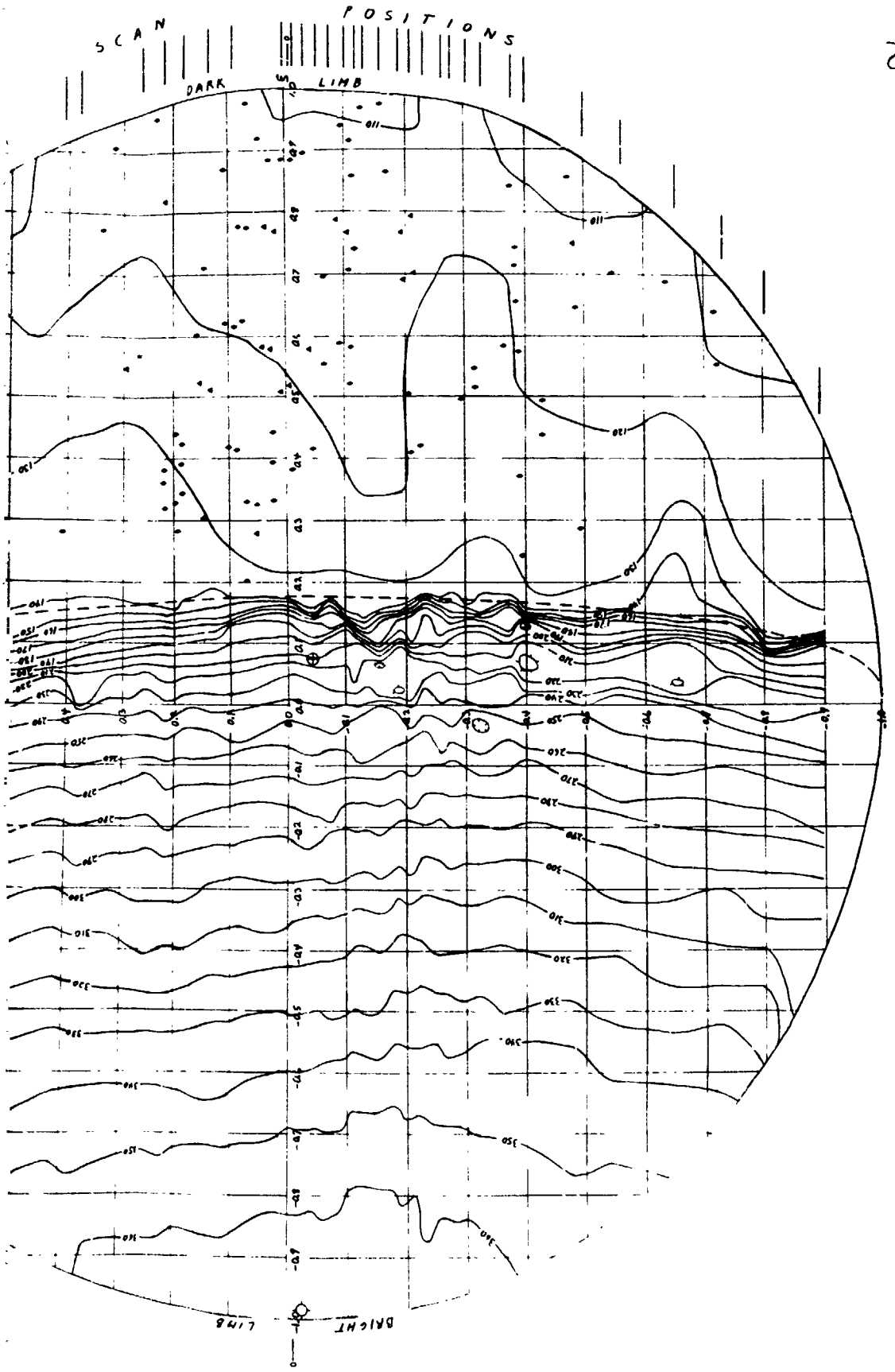

FIGURE 5-6. ISOTHERMAL LUNAR MAP FOR A SOLAR SELENOGRAPHIC COLONGITUDE OF 170 DEGREES

FOLDOUT FRAME

ISOTHERMAL LUNAR MAP FOR A CONTOUR SPACING OF 10 °K. TRIANGLES (△) MARK DARK AREAS WHICH CORRELATE WITH ANOMALIES IN THE CATALOG OF WILDEY, MURRAY, AND WESTPHAL. DIAMONDS (◇) DENOTE DARK AREAS FOUND AND REPRODUCED IN OTHER DATA, FROM RADIOMETRIC MEASUREMENTS TAKEN AT CATALINA STATION OBSERVATORY, ARIZONA, AT 08.5 HR, ON SEPTEMBER 12, 1971, IN THE 10.0 μ - 12.5 μ BAND.

SOLAR SELENOGRAPHIC COLONGITUDE 181°

TEMPERATURES IN °K

⊕ APPARENT DISC CENTER DURING OBSERVATION

— — — TERMINATOR

NOISE TEMPERATURE 100 °K

○ DETECTOR SIZE

57 SCANS

ADVANCE DIRECTION

SCAN DIRECTION

○ EFFECTIVE RESOLUTION AREA (BASED ON CIDS DATA POINTS)

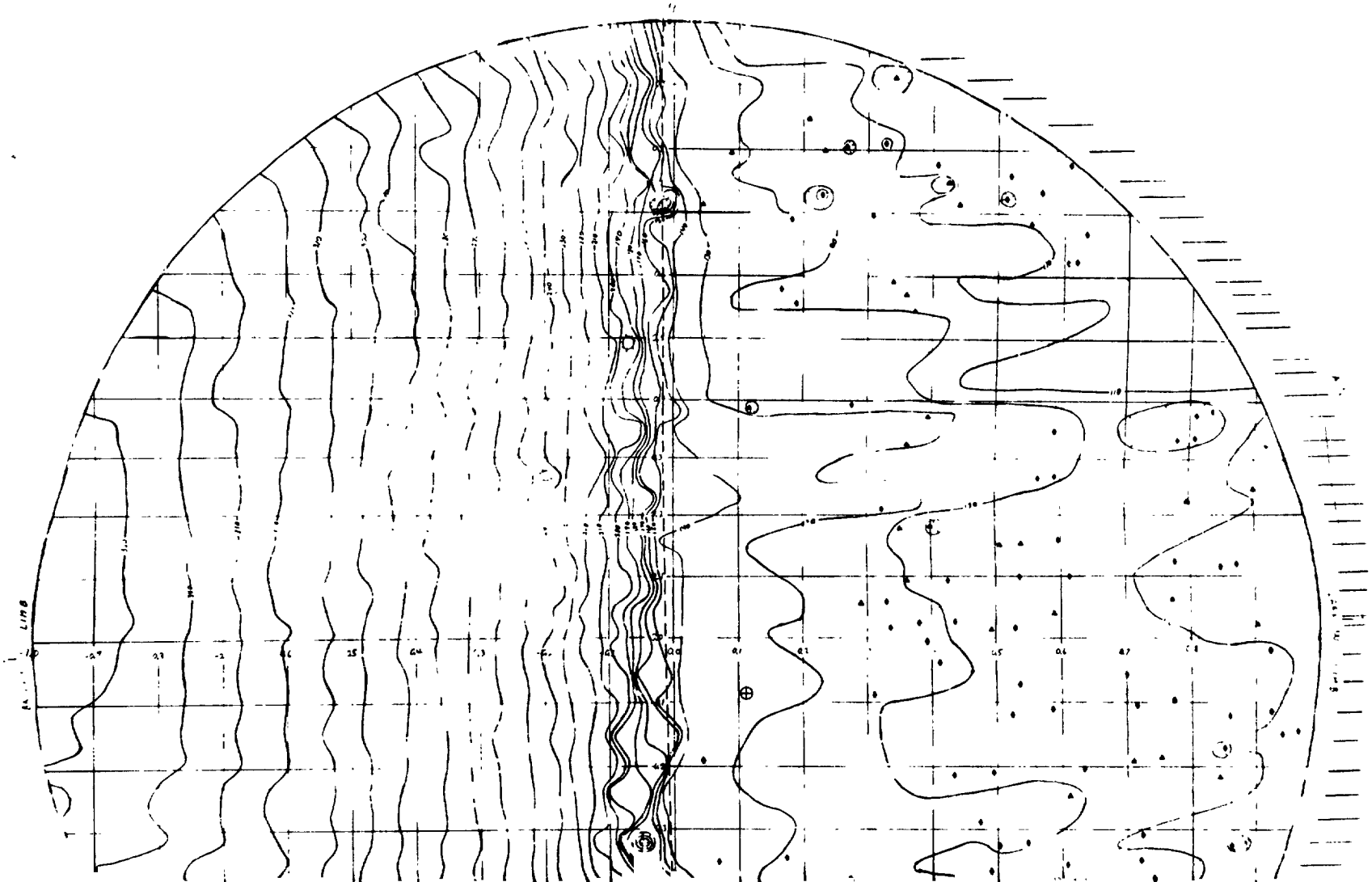

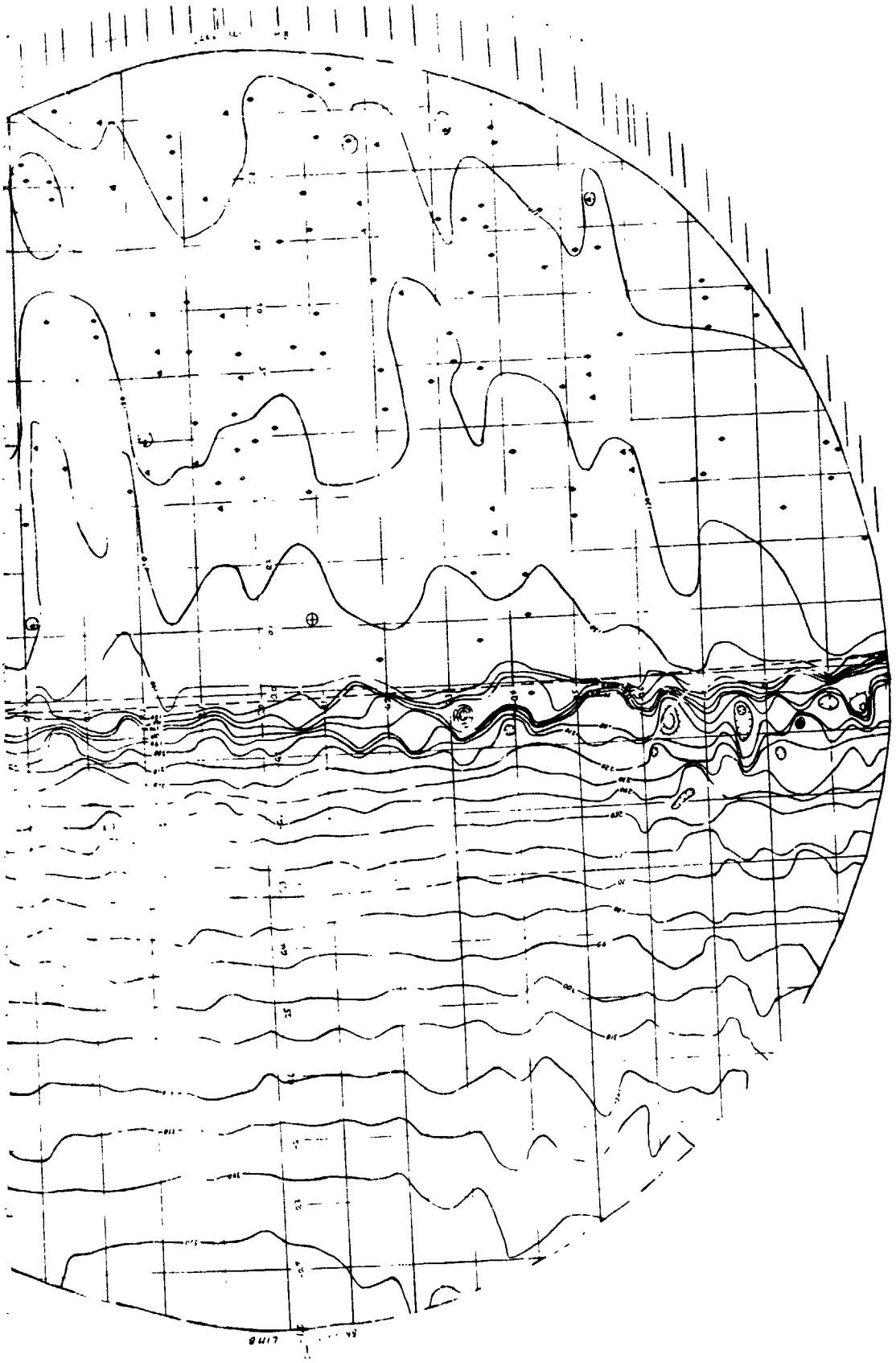

FIGURE 5-7. ISOTHERMAL LUNAR MAP FOR A SOLAR SELENOGRAPHIC COLONGITUDE OF 181 DEGREES

FOLDOUT FRAME

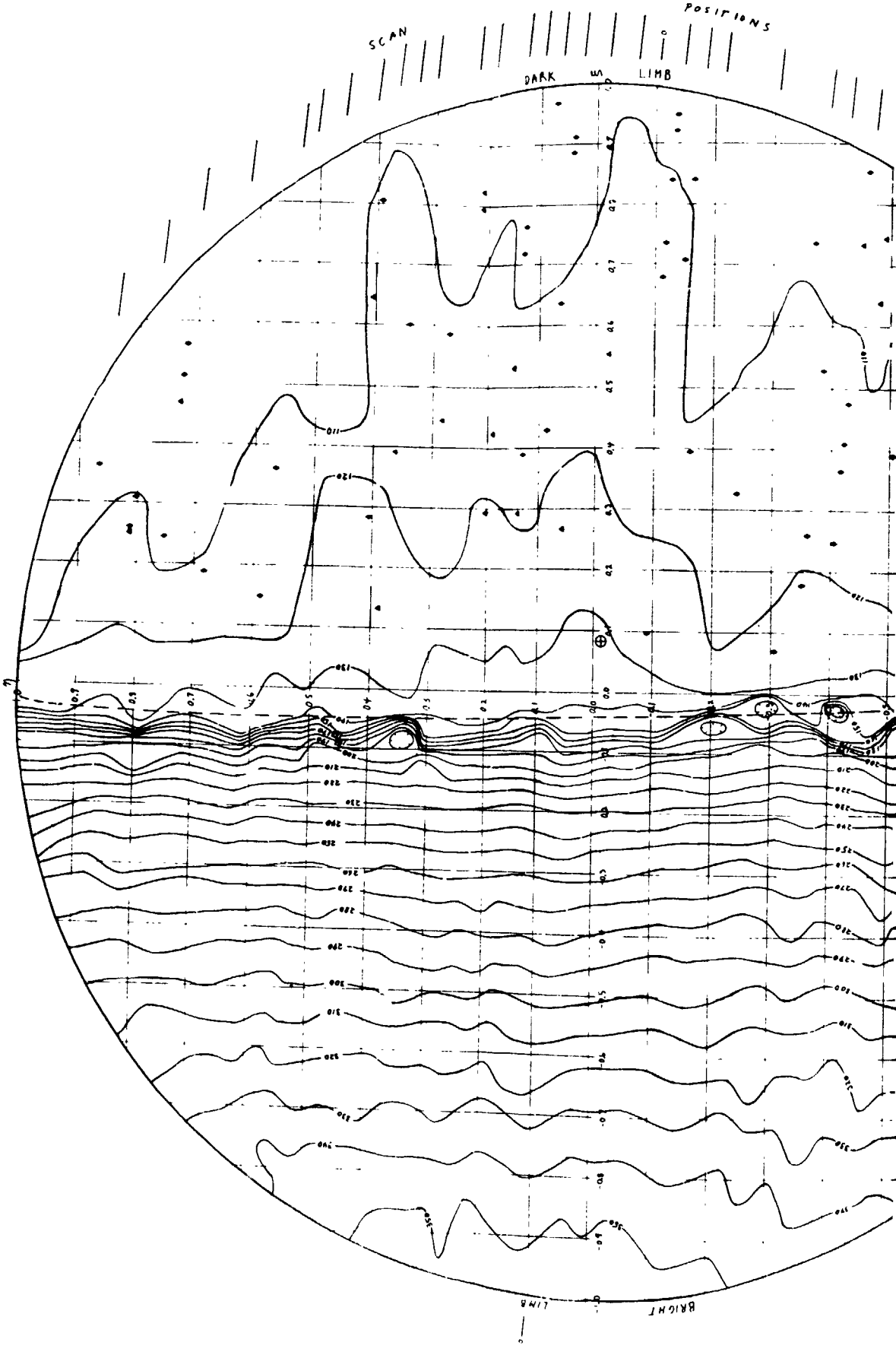

ISOTHERMAL LUNAR MAP FOR A CONTOUR SPACING OF 10 K°. TRIANGLES (▲) MARK MARE AREAS WHICH CORRELATE WITH ANOMALIES IN THE CATALOG OF WILDEY, MURRAY, AND WALKUP, AND DIAMONDS (◇) MINOR MARE AREAS WHICH ARE ASSOCIATED WITH ANOMALIES IN OTHER DATA. (MARE ABBREVIATIONS ARE AS USED IN THE CATALOG OF STEAM OBSERVATORY, ARIZONA AT 8^h U.T. ON SEPTEMBER 30, 1972, IN THE 10.6μ - 13.5μ BAND.)

SCAN DIRECTION

ARRAY DIRECTION

○ EFFECTIVE RESOLUTION AREA (BASED ON 4500 DATA POINTS)

SOLAR SELENOGRAPHIC COLONGITUDE 103°

TEMPERATURES IN °K

⊕ ANTIHEAT SUBSOLAR POINT DURING OBSERVATION

— — — — TERMINATOR

NOISE TEMPERATURE, 105°K

○ DETECTOR SIZE

50 SCANS

FOLDOUT FRAME

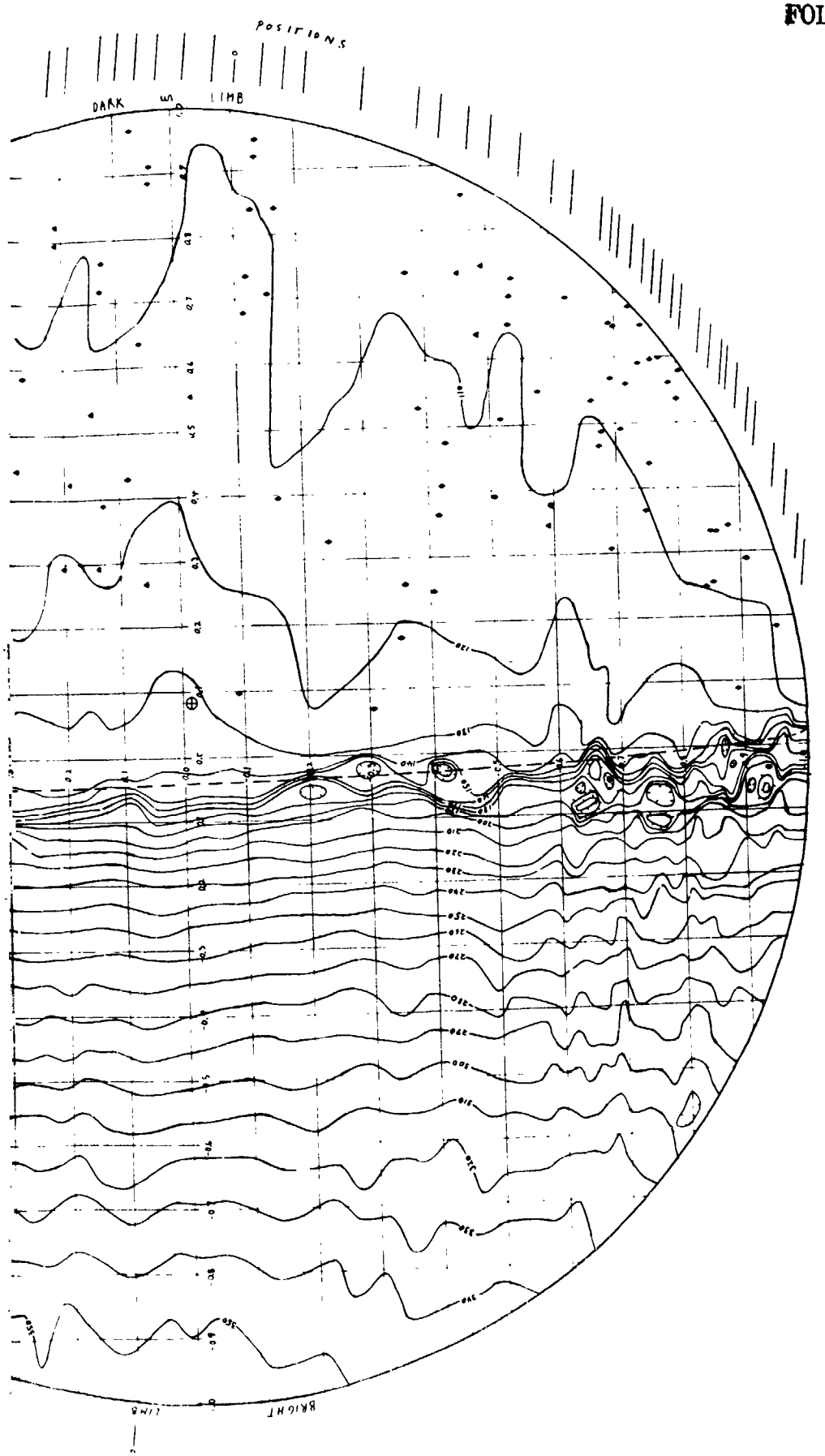

FIGURE 5-8. ISOTHERMAL LUNAR MAP FOR A SOLAR SELENOGRAPHIC COLONGITUDE OF 182 DEGREES

FOLDOUT FRAME

ISOTHERMAL LUNAR MAP FOR A CONTOUR SPACING OF 10 K° TRIANGLES & HARA WARM AREAS WHICH CORRELATE WITH ANOMALIES IN THE CATALOG OF WILDEY, MURRAY, AND WESTPHAL. DIAMONDS(◇) DENOTE WARM AREAS WHICH ARE TOO FAR PUCKED IN OTHER DATA. CIRCLES(○) DENOTE AREAS OF REDUCED EMISSION AND ERE CORRELATED WITH DATA OF ONE OTHER EVEN NO. | FROM RADIOMETRIC MEASUREMENTS TAKEN AT CATALINA STATION OBSERVATORY, ARIZONA, AT 11^h UT.) ON OCTOBER 1, 1972 IN THE 10.0 μ - 12.5 μ BAND.)

SOLAR SELENOGRAPHIC LONGITUDE 199°

TEMPERATURES IN °K

⊕ AMBIENT DISC CENTER DURING OBSERVATION

— — — TERMINATOR

NOISE TEMPERATURE 100°K

○ DETECTOR SIZE

55 SCANS

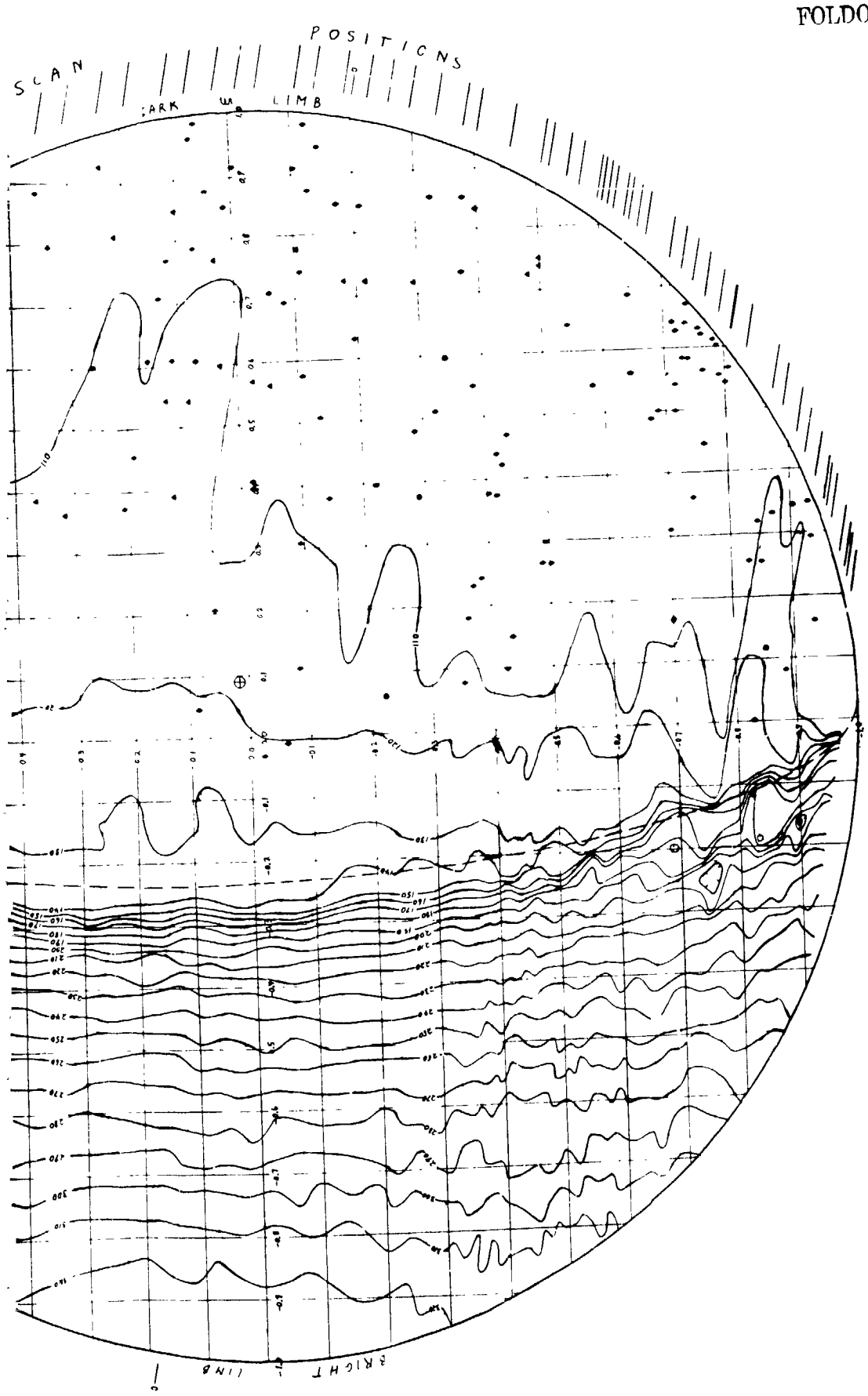

FIGURE 5-9. ISOTHERMAL LUNAR MAP FOR A SOLAR SELENOGRAPHIC COLONGITUDE OF 194 DEGREES

FOLDOUT FRAME

ISOTHERMAL LUNAR MAP FOR A CONTOUR SEPARATION OF 10 K°. TRIANGLES (▲) MARK MEAN VALUES WHICH CORRELATE WITH ANOMALIES IN THE CATALOG OF WILDEY, MURRAY, AND WESTPHAL. DIAMONDS (◆) DENOTE MEAN VALUES PUBLISHED IN OTHER DATA. APPROXIMATELY HALF OF THE RELATIVE DATA WAS SPOILED BY CLOUDS. FROM RADIOMETRIC MEASUREMENTS TAKEN AT CATALINA STATION OBSERVATORY, ARIZONA, AT 12 U.T., ON SEPTEMBER 19, 1971, IN THE 10.0μ-12.5μ BAND.

SOLAR SELENOGRAPHIC COLONGITUDE 206°

TEMPERATURES IN °K

⊕ APPARENT DISC CENTER DURING OBSERVATION

— — — TERMINATOR

NOISE TEMPERATURE 100°K

○ DETECTOR SIZE

27 SCANS

SUN DIRECTION

AZIMUTH DIRECTION

EXISTING RESOLUTION AREA (BASED ON 1971 DATA POINTS)

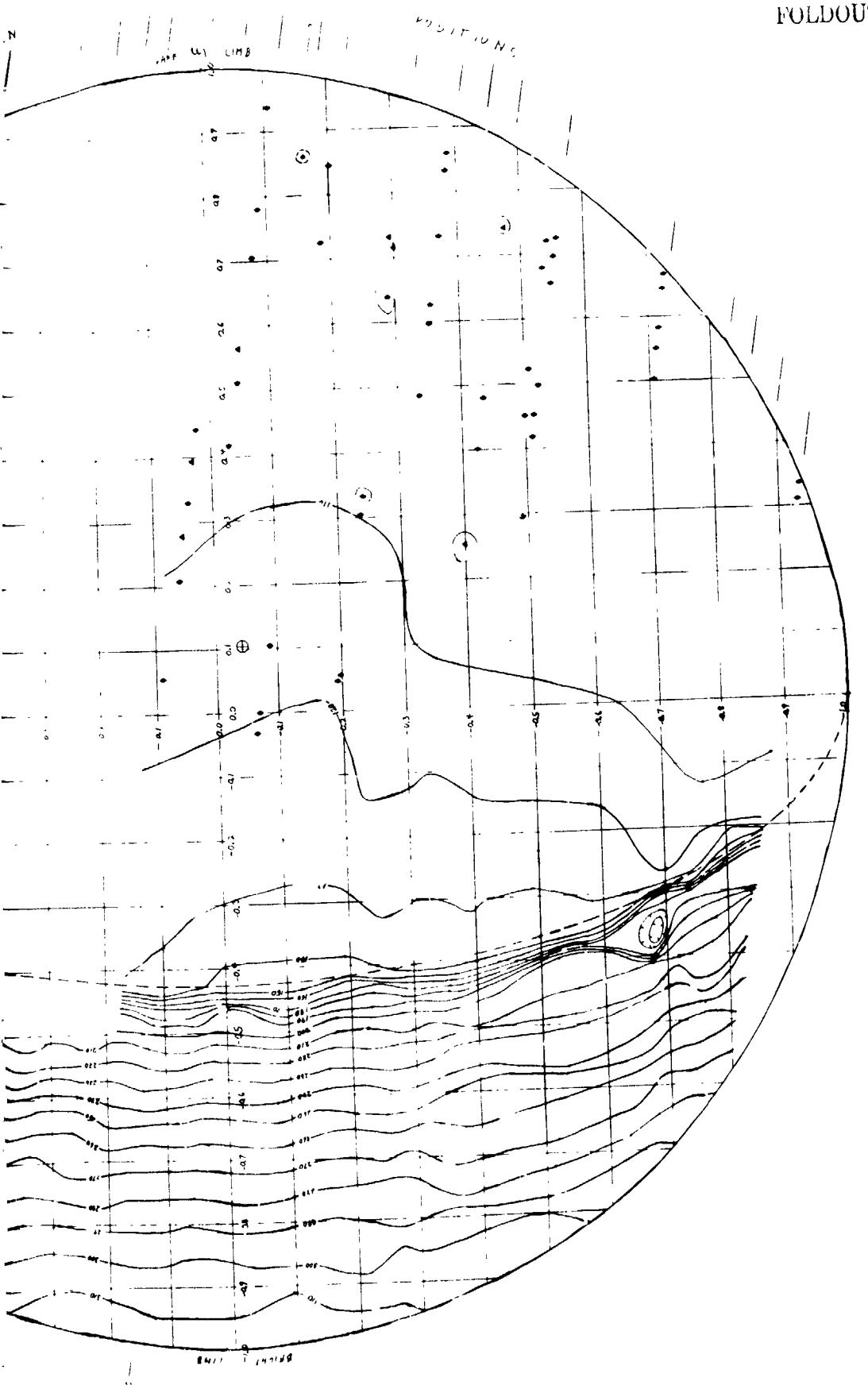

FIGURE 5-10. ISOTHERMAL LUNAR MAP FOR A SOLAR SELENOGRAPHIC COLONGITUDE OF 206 DEGREES

ISOTHERMAL LUNAR MAP FOR A CONTOUR SPACING OF 10 K° TRIANGLES(▲) MARK WARM AREAS WHICH CORRELATE WITH ANOMALIES IN THE CATALOG OF WILDLEY, MURRAY AND WESTPHAL. DIAMONDS(◆) DENOTE WARM AREAS WHICH ARE REPRODUCED IN OTHER DATA. (FROM RADIOMETRIC MEASUREMENTS TAKEN AT CATALINA STATION OBSERVATORY, ARIZONA, AT 11ʰ UT ON OCTOBER 2, 1972, IN THE 10.04-18.5μ-BAND.)

SOLAR SELENOGRAPHIC COLONGITUDE 287°

TEMPERATURES IN °K

⊕ APPARENT DISK CENTER DURING OBSERVATION

— — — TERMINATOR

NOISE TEMPERATURE 100 °K

◦ DETECTOR SIZE

33 SCANS

SCAN DIRECTION

ADVANCE DIRECTION

◯ EFFECTIVE RESOLUTION AREA (BASED ON 4500 DATA POINTS)

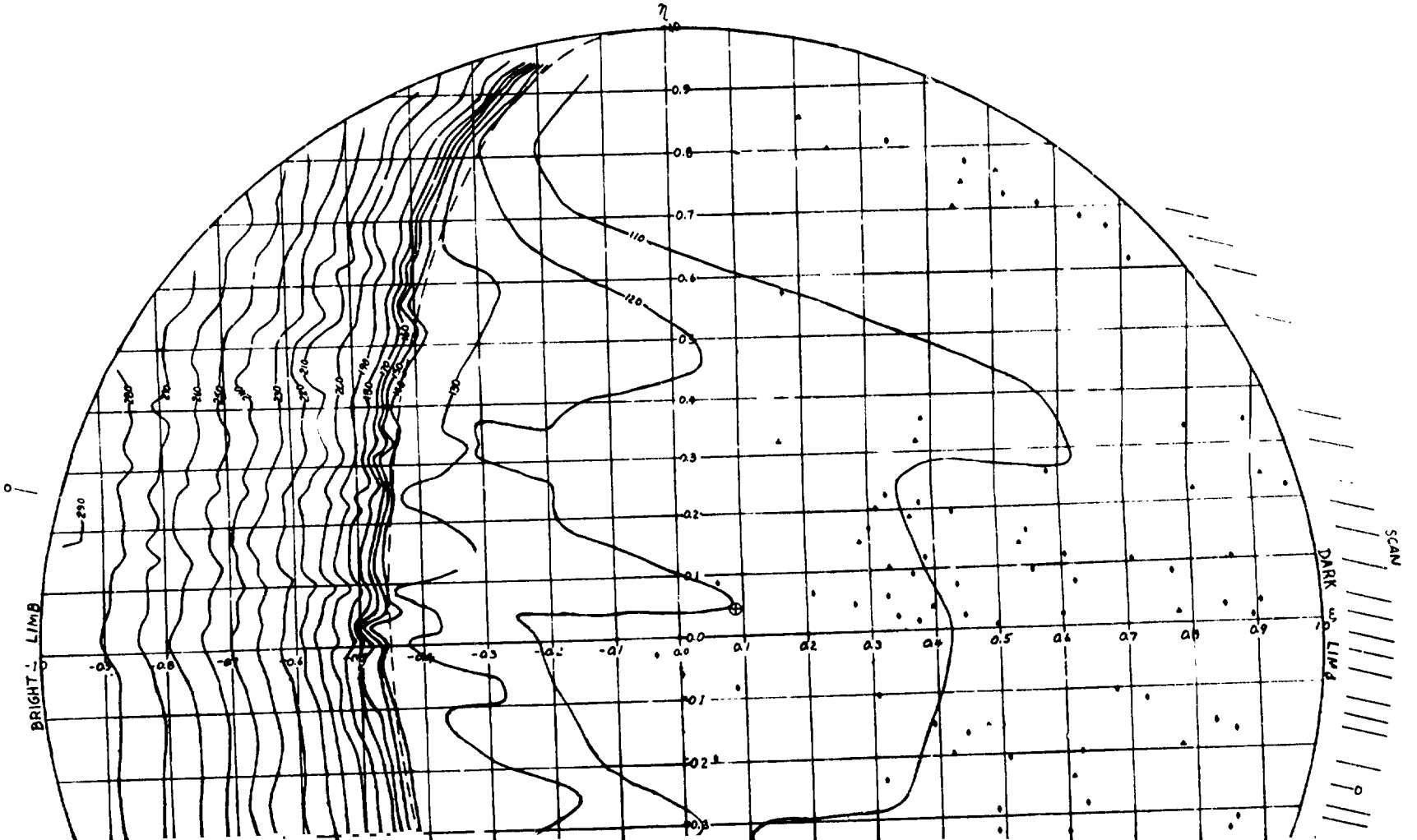

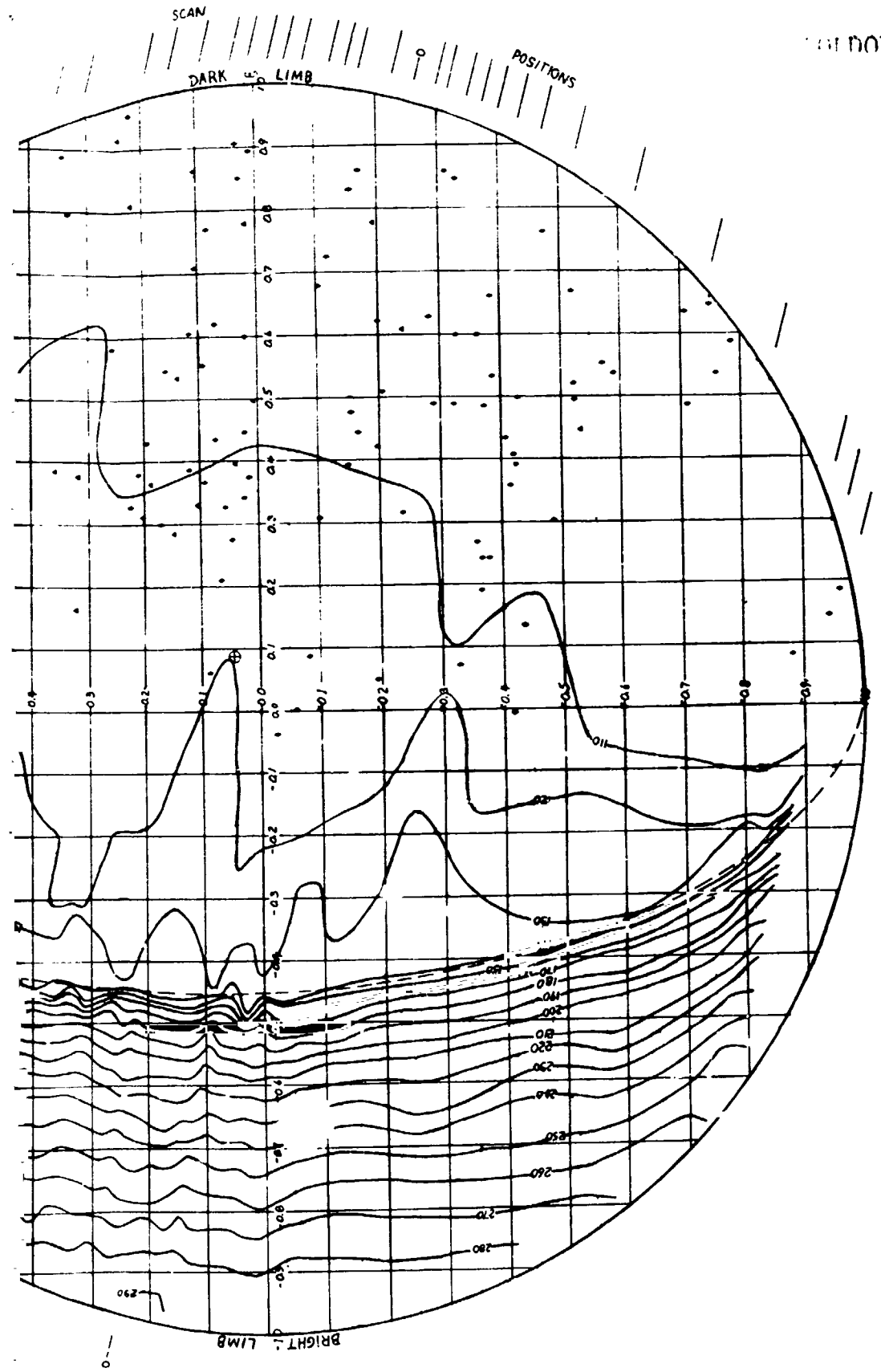

FIGURE 5-11. ISOTHERMAL LUNAR MAP FOR A SOLAR SELENOGRAPHIC COLONGITUDE OF 207 DEGREES

Because of chopper misalignment, this may be as high as 45 arc seconds. Due to this cause and also limited optical quality, the maximum achievable resolution with the 1.5 meter Arizona telescope is probably about 10 arc seconds.

As yet the 1.5 meter telescope resolution, although approached, has not been been achieved in construction of the maps. The map resolution is limited by data point separation. The drift scan method of scanning and the integration time of one second produce a data point separation in the scan direction of 15 arc seconds. The data point separation in the advance direction depends upon the number of scans, which in turn depends upon the time available for scanning. If several hours are available, about 60 scans may be recorded. In this case the data point separation in the advance direction is 30 arc seconds. The effective resolution area drawn on the maps is based upon the number of data points indicated.

The reader may note somewhat greater structure in the maps constructed from the Arizona data. This is due largely to the 5 times smaller angular detector size with this telescope. The Arizona data are also of better quality.

Many areas of infrared signal enhancement have been noted in the data of the dark lunar surface. Because of the presence of noise in the data, these must be viewed as being due to noise fluctuations as well as true lunar nighttime surface anomalies. As part of this project, a study was carried out to identify, as best as possible, true lunar nighttime surface anomalies. As the first step, the locations of all areas of signal enhancement corresponding to a detected temperature increase of at least 0.5 K° for all data sets were plotted on the standard lunar orthographic grid. The loci of all lunar darkside scans were also plotted on this same graph. A plot of these locations only is shown in

Figure 5-12. While these points cover the entire eastern quadrisphere of the lunar surface, they are not uniformly distributed. Numerous clumps of points may be identified here and there on the plot. Many of these clumps are associated with thermal anomalies in the catalog of Wildey, Murray, and Westphal (Ref. 9). The procedure which was followed was the establishment of a criterion for the identification of such clumps, and the assumption that these clumps are associated with true lunar darkside anomalies.

It was first necessary to define a criterion for membership of any point in a clump. A study made earlier in the project had indicated an average size of the anomalous regions of the order of 30 arc seconds (measured on the sky, Ref. 26). For the Arizona data, which constitutes the bulk of our lunar darkside data, the effective lunar surface area sensed for any data point is an oblong area approximately 10 arc seconds wide and 15 arc seconds long oriented parallel to the scan direction. The membership criterion chosen was that any candidate point must lie within 20 arc seconds of at least one other clump member point to be considered as belonging in the clump. The next step was establishment of a criterion for the minimum number of points which would constitute a clump, with account taken of the possibility of scans passing through a clump which do not show a signal enhancement corresponding to the chosen temperature increase threshold of 0.5 K°. This could happen in the case of a true lunar surface anomalous area if a signal decrease occurred as a result of noise or if the area had cooled to a temperature difference less than the chosen threshold. Let N be the number of points belonging to a given clump, and let n be the number of scans passing through the region which do not show the threshold increase. The criterion chosen was that

$$N - n \geq 3$$

FOLDOUT FRAME

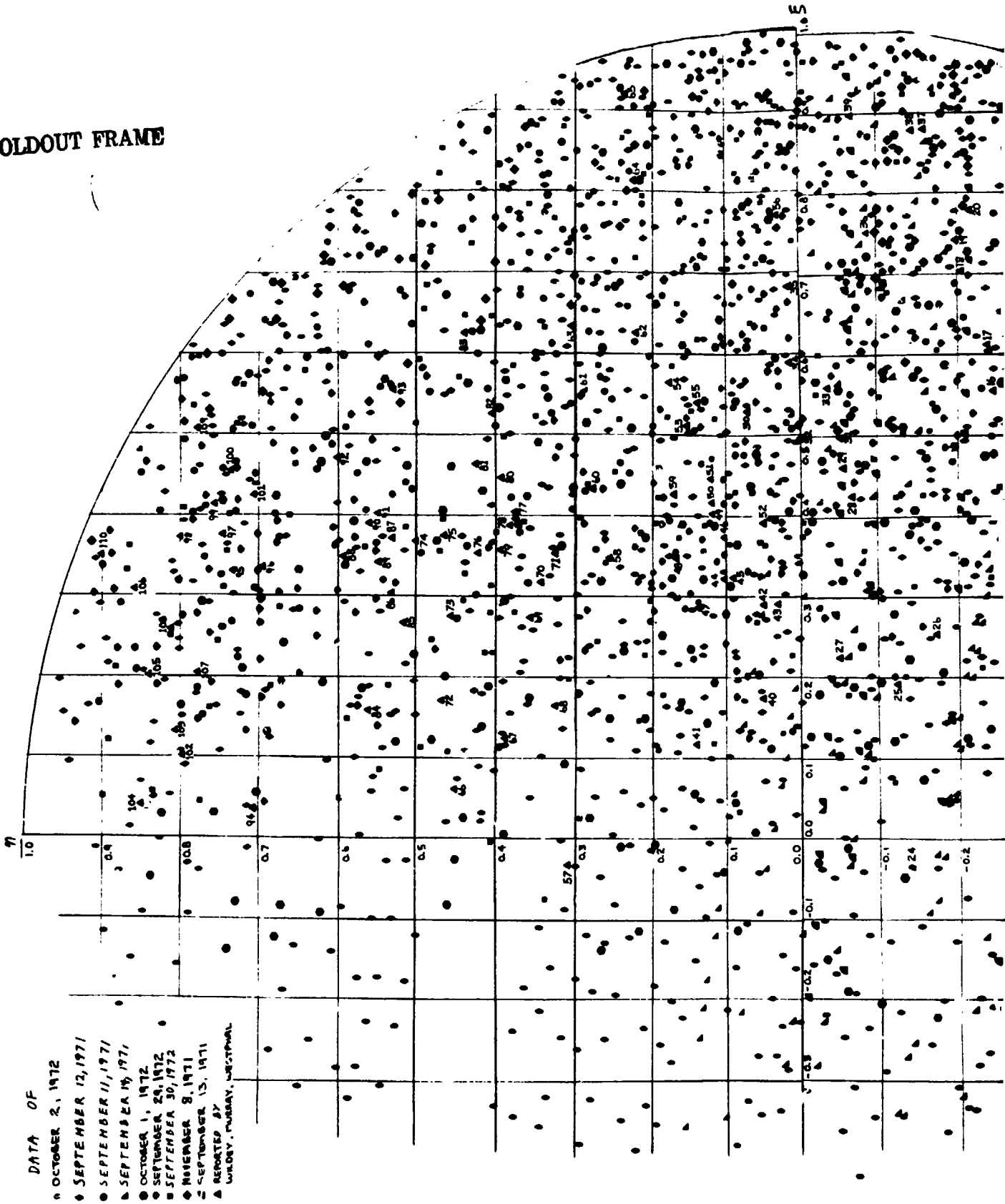

FIGURE 5-12. LOCATIONS OF PEAK LUNAR DARK SURFACE SIGNAL ENHANCEMENTS. Numbers have been assigned to the anomalies listed by Wildey, Murray, and Westphal.

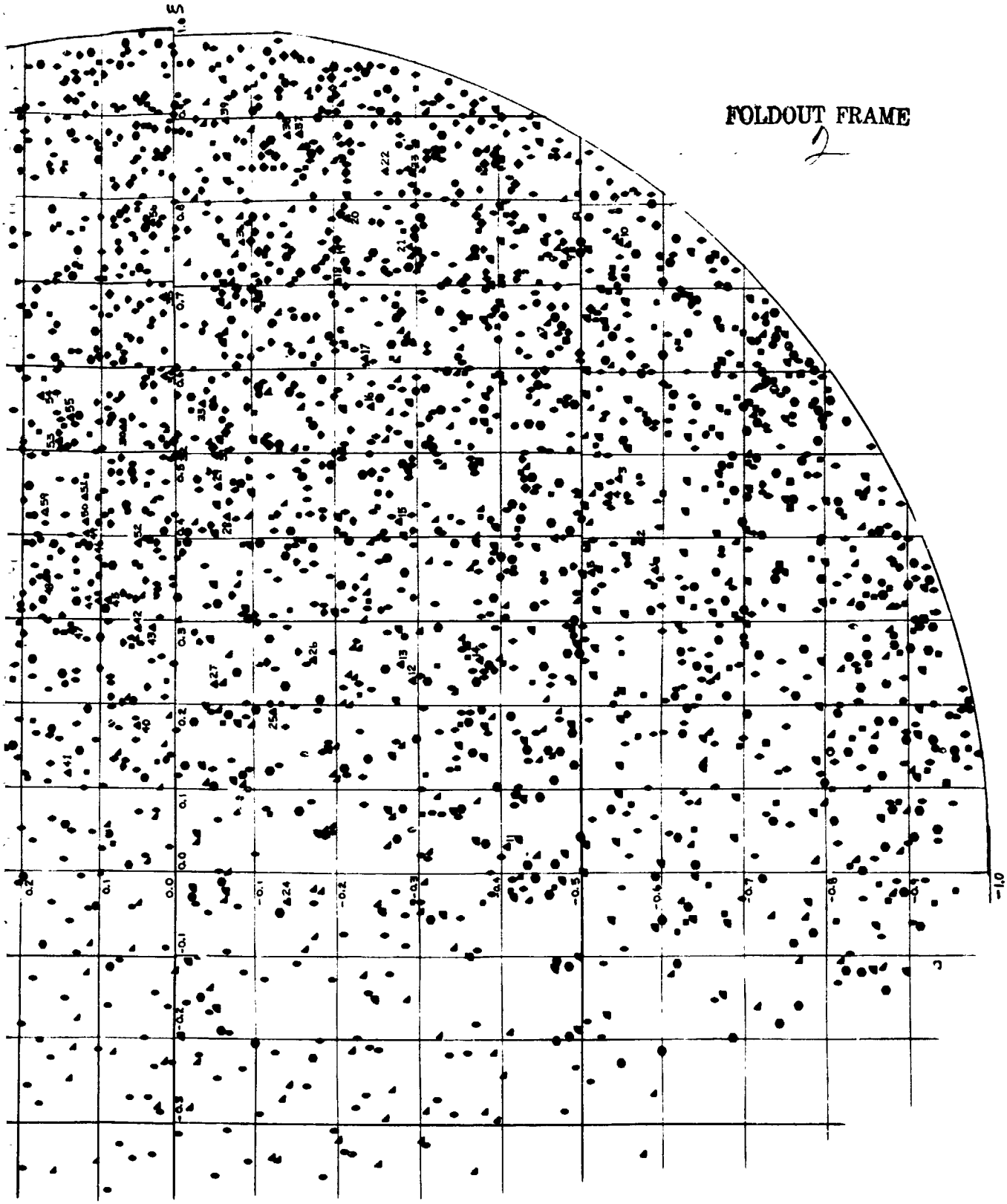

FOLDOUT FRAME 2

NHANCEMENTS.
sted by

for any clump to be identified as an anomalous region. The locations of anomalies listed by Wildey, Murray, and Westphal (Ref. 9) were also taken into account. In their paper, they state that most of the thermal anomalies they list are based on detection in each scan of identical scan pairs. The locations listed by these workers have therefore been counted twice in determination of the total number N of points. The clumps of points identified by these criteria are shown in Figure 5-13. Many of these clumps contain eight points or more and cover a considerable area.

The large number of lunar darkside scans accumulated in the project offers an opportunity for an attempt to determine the appearance (shape and thermal structure) of the anomalous areas. Any such determination must be viewed considering the noise level and the fact that the data have been taken over various phases, and at best, probably represents only a crude approximation. For all of the identified clumps, temperature enhancements were read from the data points in scans passing through the clumps and these were marked on a plot constructed on the standard orthographic grid. They were then used for drawing of contours of constant temperature difference above the background. These contours are shown in Figure 5-14. This procedure of combining data over various phases assumes that as a first approximation, the temperature difference structure of an anomalous area remains relatively fixed in comparison with the absolute temperature structure.

All of these areas are listed in Table 5-1. For each area, the table lists the coordinates, name, peak temperature difference ΔT from the surrounding region, temperature T of the surrounding region at the time of observation of the peak ΔT, time of observation of the peak ΔT after lunar sunset expressed in lunar days, size in arc seconds, dates of observation of the area, and existence in the Wildey, Murray,

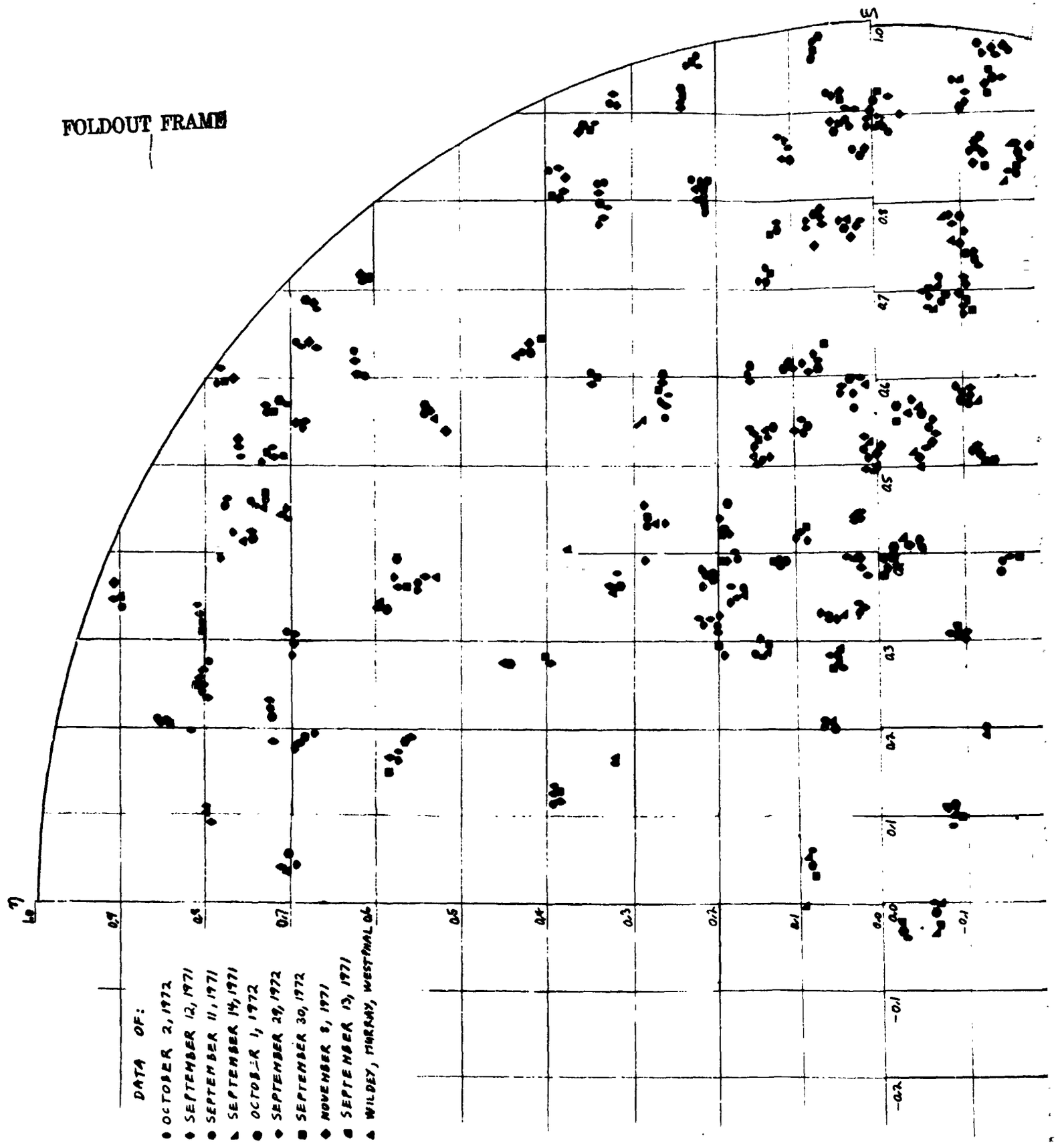

FIGURE 5-13. LOCATIONS OF PEAK LUNAR DARK SURFACE SIGNAL ENHANCEMENTS WHICH ARE ASSOCIATED WITH PROBABLE THERMAL ANOMALIES.

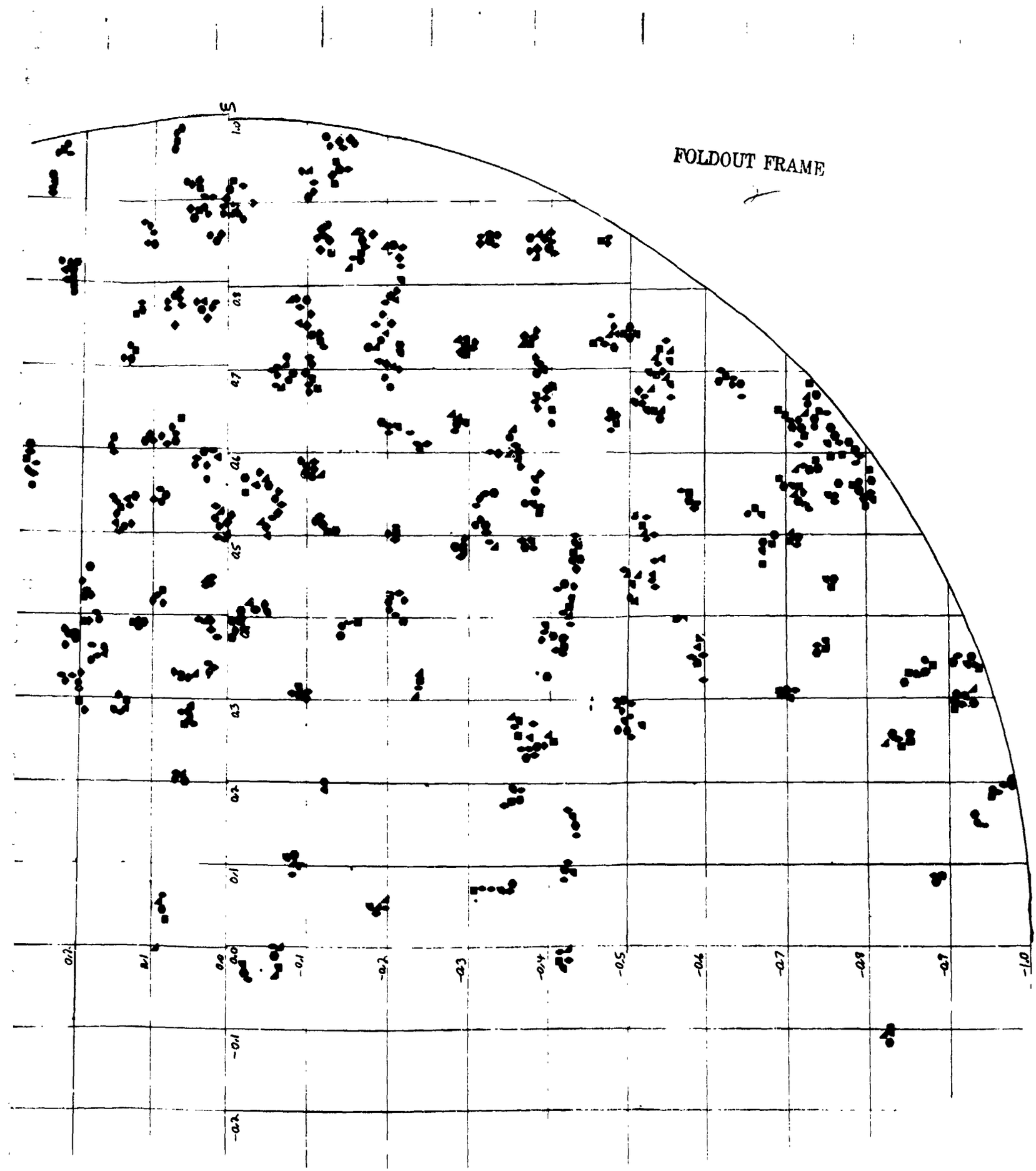

EMENTS
ES.

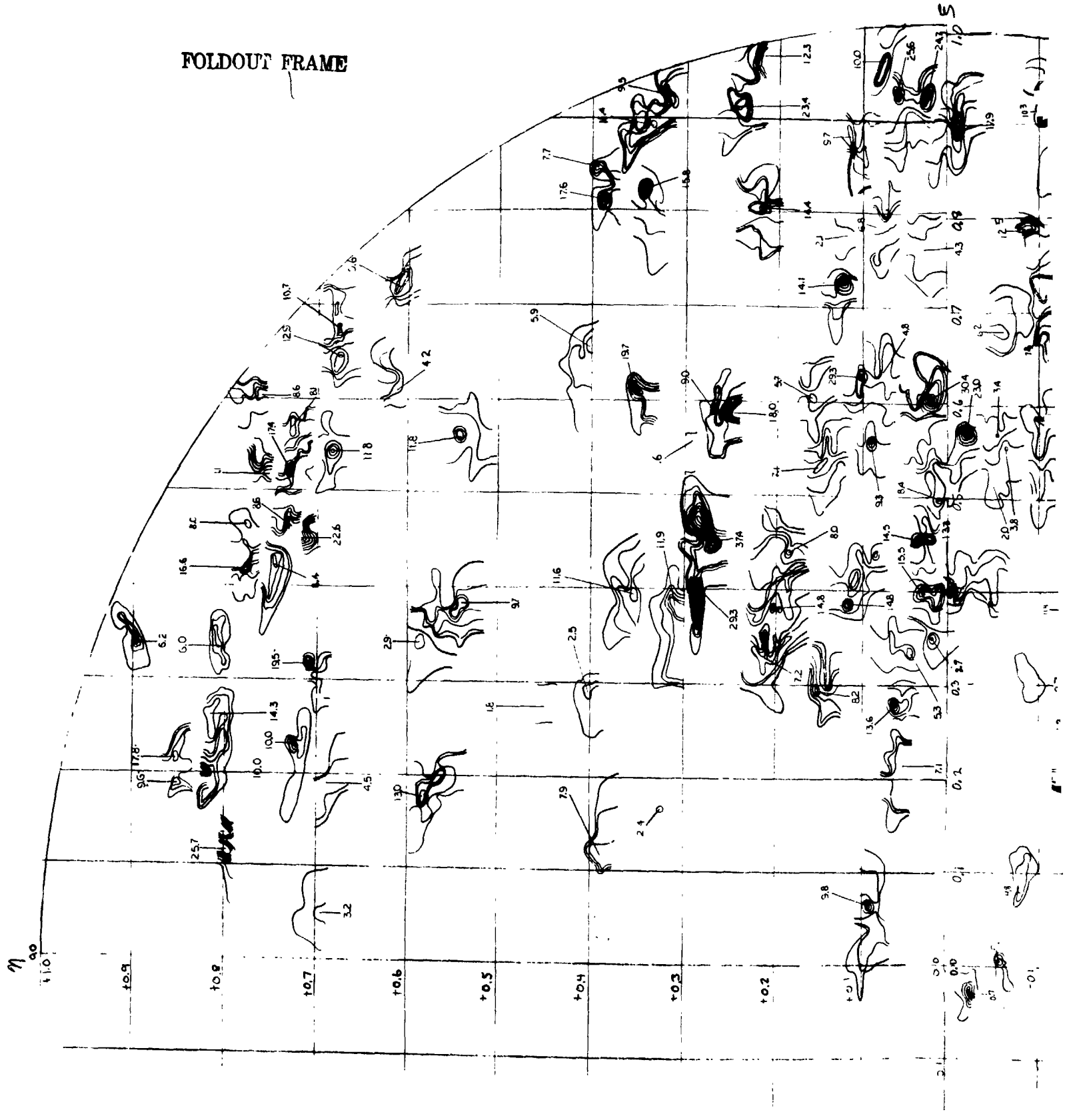

FIGURE 5-14. THERMAL STRUCTURE OF LUNAR NIGHTTIME THERMAL ANOMALIES AS INDICATED BY THE SCAN DATA. The contours represent temperature enhancement above the background, and are spaced at intervals of 2.5 K°. The peak enhancement observed for each area is marked on the map in units of K°.

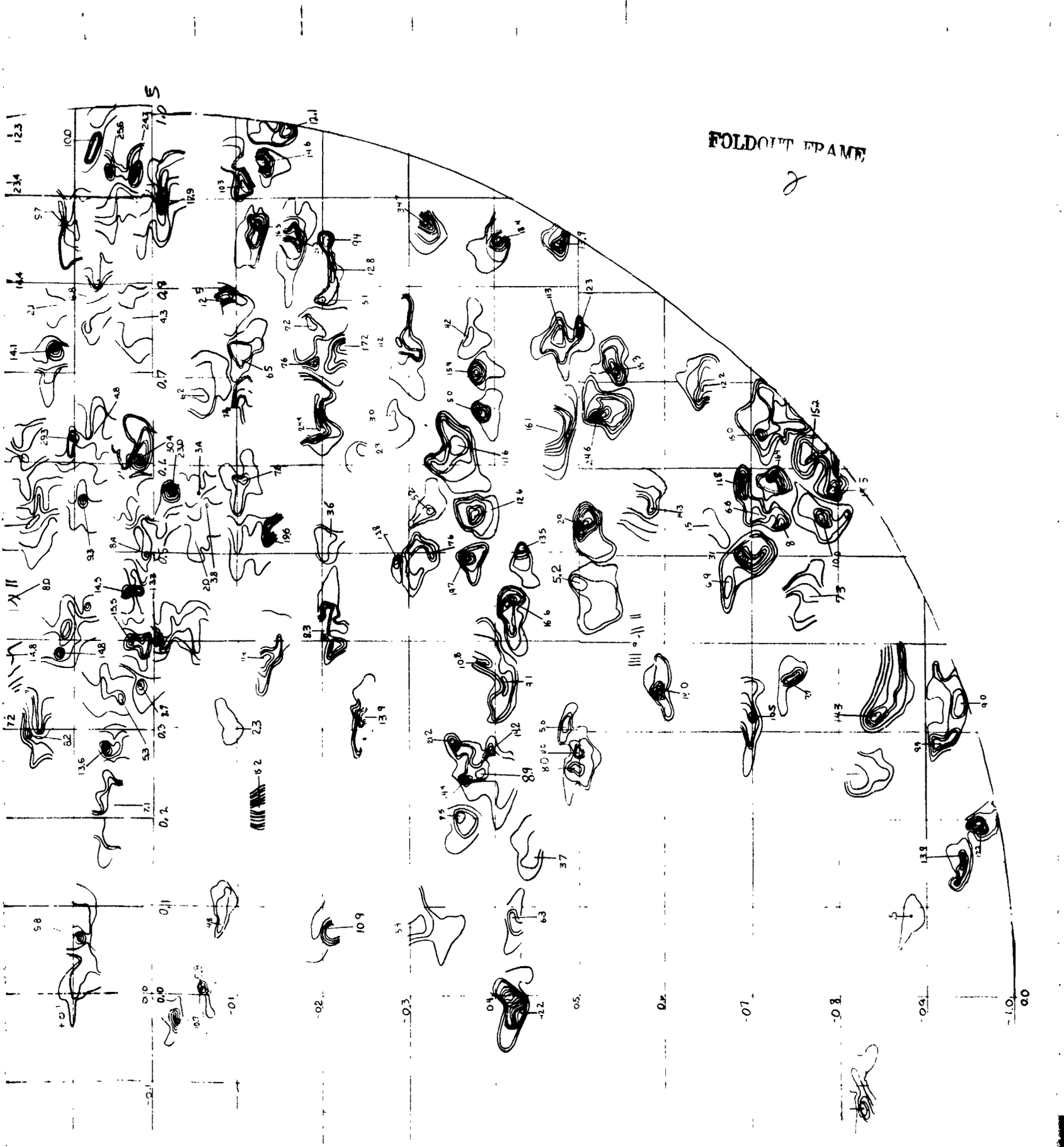
FOLDOUT FRAME

TABLE 5-1. LUNAR NIGHTTIME THERMAL ANOMALIES

COORDINATES		LOCATION	ΔT (K°)	T (°K)	DATES OF OBSERVATIONS									SIZE (arc sec)	t (Lunar Days)	WMW
					9/11/71	9/12/71	9/13/71	9/14/71	11/8/71	9/29/72	9/30/72	10/1/72	10/2/72			
+0.190	-0.965	Between Boguslawsk, and Demonex	17.2	97	xx	x					x	x	X	35	0.183	
+0.160	-0.945	Between Manzinus and Boguslawsky	13.9	98	x							x	X	45	0.153	
+0.335	-0.940	5° East Neumayer	9.0	106		xx	x	x				xx		35	0.233	
+0.290	-0.920	Northwest rim of Boussingault	9.4	115		x	x			x		x		25	0.123	
+0.125	-0.835		10.9	218			x	x			X	x	x	30	0.042	
+0.010	-0.855	3° Northwest of Zach	1.5	100							x	x	X	30	0.081	
+0.245	-0.825	East rim of Hommel	5.6	109		x		X			xx	xx		45	0.144	
+0.315	-0.845	1° South Southwest of Hearch	14.3	110	x						xxx	Yx		45	0.142	
+0.355	-0.745	Between Pitiscus and Lockyer	7.7	105		x	x				x	X		30	0.131	
+0.445	-0.760	2° Southwest of Steinheil	7.3	105			x				x	X		45	0.159	
+0.540	-0.780	5° South of Reimerus	10.0	102	x	xx	x				xx	Xxx	x	50	0.21	
+0.575	-0.790	3° South of Brisbane	19.5	110	X		x				xxx	xxxx	xxx	40	0.169	
+0.610	-0.770	4° Southeast of Brisbane	15.2	95	x		x				xxx	xxxx	Xxx	45	0.28	
+0.535	-0.740	4° East of Steinheil	8.0	110		X	x	x		x	xx	xx	x	30	0.153	
+0.545	-0.715	8° North Northwest of Steinheil	6.6	102		x	x	X		x	xx		x	30	0.217	
+0.585	-0.735	East rim of Reimarus	16.4	108		X	x				x	xx		30	0.167	
+0.635	-0.715	East rim of Petrescius	15.0	100	xx	x	Xx	xx		x	xxxx	xxxx		85	0.215	
+0.315	-0.700	Between Spallanzani and Nicolai	10.5	106		xx	x				x	X		30	0.111	
+0.465	-0.675	West rim of Fabricius	6.9	111			x	x			Xxx	xxx	x	30	0.114	
+0.505	-0.685	East rim of Fabricius	31.0	103			x	x			xxx	Yxx	x	20	0.158	
+0.575	-0.690	West rim of Mallet	11.8	107		x	x	x		x	Xx		x	20	0.153	
+0.530	-0.655	South inside rim of metius	1.5	109	x		x				X			30	0.131	
+0.685	-0.645	3° Southeast of Furnerius	12.2	102		x	x			x	x	Xx	x	60	0.219	
+0.345	-0.590	Northwest rim of Riccius	14.0	113		xxx					X			40	0.078	x
+0.400	-0.565	6° Northeast of Riccius	9.6	111							X			15	0.086	x
+0.550	-0.585	Between Rheita, Neander, and Benner	14.3	104		x				x		x	xx	40	0.156	
+0.455	-0.490	2° South of Stiborius	5.2	119	x	Xxx	x	xxx						55	0.092	xx
+0.450	-0.510	South rim of Piccolamim	20.0	105		x	xx	Xx						40	0.161	
+0.655	-0.525	1° Southeast of Reichenbach	24.6	110		Xx	xxx	xx	xx		x		x	55	0.142	
+0.715	-0.545	2.5° Southeast of Stevinus	15.3	113		x		xxx		X	x			35	0.136	
+0.020	-0.430	East inside rim of Purbach	42.2	163		X	x	x			x		x	40	0.006	
+0.080	-0.425	West rim of Krusenstern	6.3	113		x	x					x	X	30	0.092	
+0.155	-0.425	Between Playfair and Apianus	3.7	108		x	x					X	x	45	0.67	
+0.255	-0.500	2° Southeast of Pontanus	8.0	107		xx	x			x		Xxx	xx	50	0.086	
+0.280	-0.500	Southwest rim of Wilkens	11.0	117		xx	X			x	x	xxx	xx	50	0.089	
+0.310	-0.490	Southeast rim of Wilkens	5.6	102		xx	x			x	x	xxx	Xx	50	0.133	
+0.350	-0.415	Between West slope of Rupes Altai and Pons	9.1	122		X	x					x	xx	60	0.067	

TABLE 5-1 - Continued

COORDINATES		LOCATION	ΔT (K°)	T (°K)	DATES OF OBSERVATIONS									SIZE (arc sec)	t (Lunar Days)	WWW
ξ	η				9/11/71	9/12/71	9/13/71	9/14/71	11/8/71	9/29/72	9/30/72	10/1/72	10/2/72			
+0.445	-0.420	4° Southeast of Polybius	16.6	105				x		x	x	Xx	xxx	35	0.122	
+0.505	-0.435	5° South of Fracastorius	13.5	99	x	x		x	x	x	x	x	Xx	20	0.169	
+0.535	-0.485	5° South of Borda	16.1	112		X				x	x	x	..	40	0.133	
+0.750	-0.480	2° East of Snellius	11.3	112		x	x	x		x	xx	xxx	xx	60	0.136	
+0.755	-0.500	2° Southeast of Hase	12.3	102		x	x	x		x	xx	Xxx	xx	60	0.206	
+0.845	-0.480	East rim of Legendre	3.9	107						X	x		x	30	0.183	
+0.850	-0.405	West rim of Humboldt	18.4	98		xx	X	xx	xx	x		xx		45	0.22.	
+0.700	-0.300	North inside rim of Arzachel	5.9	108		x	x				x	x	xx	60	0.136	
+0.205	-0.355	1° South of Geber	7.5	101		x					x	x	Xx	45	0.111	x
+0.250	-0.385	Sacrobosco	8.9	105		xx	x	xx		x	xx	xx	Xxx	80	0.119	x
+0.275	-0.395	Sacrobosco	14.2	106		xx	x	xx		x	xx	xx	Xxx	80	0.122	x
+0.290	-0.350	2° North Northeast of Sacrobosco	21.2	108		xx	x	Xx		x	xx	xx	xxx	80	0.122	x
+0.240	-0.370	2° East of Azophi	14.4	108		xx	x	Xx		x	xx	xx	xxx	80	0.114	x
+0.375	-0.385	2° West of Polybius	10.8	125		x	x			X	x	xx	xx	50	0.035	
+0.495	-0.370	Fracastorius	19.7	118		X	x					x	x	30	0.094	
+0.500	-0.330	North rim of Fracastorius	7.6	118	x	X	x			x		x	x	45	0.097	
+0.535	-0.380	East edge of Fracastorius	12.6	106	x		X				x	x	x	45	0.133	
+0.630	-0.360	West rim of Santbech	11.6	113	x	X	x	xx		xx	x	x	x	55	0.122	
+0.655	-0.385	1° Southeast of Santbech	15.0	97	x	x	xx		x	x	x		X	35	0.203	
+0.705	-0.380	1° Northwest of Biot	15.9	100	x	x	X			x			x	35	0.172	
+0.740	-0.375	3° Northeast of Biot	4.2	108		x		x		x	X	x		30	0.156	
+0.875	-0.320	2° South of Lame	34.7	104	x	X			x			x	xx	40	0.192	
+0.025	-0.210	Between Ptolemaeus, Alphonsus and Klein	10.9	118		x	x	Xx					x	40	0.078	
+0.310	-0.250	2° North of Tacitus	13.9	111			xx				x		X	30	0.125	
+0.410	-0.200	West rim of Theophilus	8.3	120	x	x	x			Xx		x	x	30	0.039	
+0.520	-0.210	North end of Mare Nectaris	3.6	106		x	x					x	X	30	0.167	
+0.495	-0.285	3° Northeast of Beaumont	13.8	124		x	x		x	x			x	45	0.061	
+0.545	-0.225	North end of Mare Nectors	5.2	105		x				x		X	x	10	0.133	
+0.620	-0.250	West slope of Montes Pyrenaeus	2.9	120		X							x	25	0.114	x
+0.640	-0.280	East slope of Montes Pyrenaeus	3.0	104	x		x	Xx					x	30	0.192	
+0.740	-0.285	1° South of McClure	11.2	103		x	x	Xx		x		x		40	0.214	x
+0.735	-0.230	Between Crozier and Bullot	17.2	102		x	x		x	x		X		45	0.172	x
+0.785	-0.200	Mare Frecunditatis	5.1	101		x	x	x	xx	x		x	Xx	20	0.222	x
+0.820	-0.215	East side of Mare Fecunditatis	12.8	100		x	x	x	xx	x		x	Xx	20	0.233	x
+0.850	-0.210	South rim of Langrenus	9.4	100		x	x	x	xx	x		X	xx	20	0.208	x
+0.200	-0.120	3° East North East of Hind	15.2	164	x									15	0.000	
+0.380	-0.140	1° East of Sollner	11.9	108		x	x			x		X		30	0.103	x
+0.640	-0.195	1° Southwest of Goclenius	24.4	120	x	X	x			x		x	x	45	0.117	
+0.715	-0.190	Near the creator Goclenius	7.6	112		X	x		x	x		x		45	0.133	
+0.755	-0.185	Central Mare Fecunditatis	7.2	111	x	X		x	x	x		x		50	0.142	x
+0.855	-0.170	Near West edge of Langrenus	21.3	110	x	X		xx	x	x	x	x		50	0.169	
+0.865	-0.125	Langrenus	16.5	110		x			xxx	x	x	X		40	0.206	

TABLE 5-1 Continued

COORDINATES		LOCATION	ΔT (K°)	T (°K)	DATES OF OBSERVATIONS									SIZE (arc sec)	t (Lunar Days)	WMW
					9/11/71	9/12/71	9/13/71	9/14/71	11/8/71	9/29/72	9/30/72	10/1/72	10/2/72			
+0.915	-0.105	7° Northeast of Langrenus	10.3	112		X		X		XX		X		40	0.189	
-0.940	-0.135	8° West of Maclaurin	14.6	118		X			X		XX	X		40	0.128	
+0.975	-0.160	Maclaurin	12.1	108		X			XX	XX		X		40	0.194	
-0.330	-0.035	Oppolzer	10.7	117			X					X	X	30	0.069	
-0.305	-0.005	1° North of Oppolzer	6.8	117			X	XX				X	X	15	0.375	
+0.080	-0.085	.5° Southwest of Horrocks	4.8	116				X			X	X	XX	25	0.089	
+0.300	-0.160	Northeast rim of Taylor	2.3	115		X	X		X			X		20	0.020	
+0.670	-0.160	5° South of Lubbock	7.3	106		X	X		X	XX	X		X	35	0.194	
+0.675	-0.130	1° Northeast of Lubbock	6.2	104	XX	X	XX	XX		X		X		50	0.156	
+0.875	-0.060	East side of Mare Fecunditatis	12.5	113		X		X	X	XX		X		45	0.144	X
+0.720	-0.110	Central Mare Fecunditatis	6.5	113		X			XX	XX	X		X	40	0.133	
+0.345	+0.035	In Thales	6.2	111	X	X			X					25	0.114	X
+0.330	+0.865	Northeast of Bail,	6.0	111		X				X	X		X	20	0.097	
+0.410	+0.780	Between Hercules and de la Rue	16.6	119	XX	X				XX				25	0.11	
+0.465	+0.770	Between Hercules and Endymion	8.0	95	X								X	20	0.200	
+0.310	+0.705	West of Bun,	19.5	117	X	X			X	X				25	0.039	
+0.430	+0.745	North rim of the crater Hercules	8.4	110		X						X		30	0.111	X
+0.465	+0.725	West rim of Atlas	8.6	105	X					X	X		X	15	0.120	X
+0.445	+0.710	South rim of Hercules	22.6	109		X				X			X	15	0.108	
+0.510	+0.760	Between Endymion and Atlas	11.1	95		X			X				X	20	0.214	
+0.515	+0.725	East of Atlas	17.4	104	X	X				X	X			30	0.136	
+0.600	+0.765	North of Mercurius	8.8	115		X			X	X	X			20	0.120	
+0.570	+0.730	Between Mercurius and Atlas	7.1	109	X	X					X		X	15	0.158	
+0.170	+0.830	In Mare Frigoris	25.7	100		X							X	15	0.103	X
+0.190	-0.860	East of Sheepshanks	9.6	120	X	X							X	15	0.067	X
+0.110	+0.855	North of Gable	17.8	98	X	X							X	15	0.142	X
+0.200	+0.830	Just West of Gable	10.7	98									X	20	0.133	X
+0.255	+0.820	East of Gable	14.3	113	X	X				X	X		X	25	0.078	X
+0.045	+0.690	North of Cassini	3.2	190		X				X		X		15	-0.019	X
+0.225	+0.730	Between Eudoxus and Mitchell	10.0	123	X	XX						X		15	0.016	
+0.180	+0.690	West rim of Eudoxus	4.5	122		X				XX	X			30	0.042	
+0.170	+0.580	South of Calippus	13.0	113		XX				X	X	X	X	30	0.039	
+0.340	+0.580	In Lacus Somniorum	2.9	112		X						X	X	30	0.136	
+0.375	+0.540	Northwest of Posidonius	9.7	115	X	XX				XX	X	X		40	0.078	
+0.545	+0.680	East rim of Gerasted	11.8	113		X			X	X				20	0.10	
+0.645	+0.675	In Mare Struve	12.9	117	X	X			X				X	25	0.10	
+0.670	+0.670	South end of Mare Struve	11.7	114						X		X	XX	20	0.108	
+0.545	+0.540	Between Kirchoff and Maury	11.8	118	X				X	X		X		50	0.078	X
+0.605	+0.610	Between Beryllius and Franklin	4.2	115	XX	XX								25	0.100	
+0.710	+0.615	South of Messala	9.6	99					X			X	X	30	0.25	
+0.75	+0.395	West edge of Mare Serenitatis	7.9	195	X	X					X			30	-0.011	X
+0.165	+0.325	In Montes Haemus	2.4	148									X	10	0.103	X
+0.275	+0.370	Middle of Mare Serenitatis	1.8	114								X		30	0.089	X
0.280	+0.410	Middle of Mare Serenitatis	2.5	123		X				X	X			20	0.056	

TABLE 5-1 - Continued

COORDINATES		LOCATION			DATES OF OBSERVATIONS								SIZE (arc sec)	t (Lunar Days)	WM
					8/11/72	8/12/72	9/13/72	9/14/72	11/8/72	9/	9/30/72	10/1/72	10/2/72			
+0.32	+0.355	Southern part of Mare Serenitatis		1		x					x	x	x	30	0.142	xx
	+0.330	Southern part of Mare Serenitatis	11.9	111	x							x	x	30	0.142	x
+0.648	+0.468	North of Macrobius		111	x	x					x	x		25	0.131	x
+0.670	+0.350	South of Macrobius	19.	135	x	x					x			20	0.081	
+0.610	+0.380	North edge of Mare Crisium	17.6	115	x	x					x			20	0.136	
+0.6	+0.345	North edge of Mare Crisium	7.	115	x	x			x					20	0.147	
+0.82	+0.4	North part of Mare Crisium	25.	114	xx	xx				x		x	x	30	0.133	
+0.8	+0.45	East rim of Mare Crisium	11.4	102					x		x	x	x	30	0.250	
+0.82	+0.320	East of Mare Crisium	6.8	109	x	x				x				25	0.214	
+0.39	+0.9	Just north of Filimus	29.3	133						x				15	0.039	
+0.44	+0.40	Between Tranquillitatis and Serenitatis	37.4	116	x					xx	x			30	0.081	x
+0.55	+0.09	North of Triesnecker	9.8	116				x			x	x	x	25	0.081	
+0.3	+0.2	Between Tranquillitatis and Serenitatis	7.	131	x	xx				xxxx	x		x	35	0.056	x
+0.375	+0.05	East of Ray	14.3	114	xx	x				xxx	x	x	x	35	0.103	
+0.43	+0.19	Middle of Tranquillitatis	8.0	109						xx	x	x	x	35	0.147	
+0.290	+0.155	West rim of Sosigenes	8.2	139	x					x	x		x	35	0.014	x
+0.375	+0.125	Northeast of Arago	14.9	110	x	x				xx	xx	x	x	4	0.136	
+0.580	+0.260	Northeast edge of Tranquillitatis		112	x	x				x	x	x	x	35	0.14	
+0.570	+0.265	Northeast edge of Tranquillitatis		105	x	x				x	x	x	x	35	0.175	
+0.550	+0.290	Northeast edge of Tranquillitatis		126										10	0.069	x
+0.530	+0.165	Middle of Tranquillitatis	7.1	114		x				xx	x		x	50	0.064	xx
+0.595	+0.1	East part of Tranquillitatis	5.7	115		xx				x		x		40	0.105	
+0.555	+0.	Middle of Tranquillitatis	4.3	108	x	x						x	x	50	0.169	
+0.62	+0.1	East edge of Tranquillitatis	7.	119						x		xx	x	30	0.080	
+0.6	+0.2	East edge of Tranquillitatis	4.	119		x				xx	x	x	x	40	0.067	
+0.5	0.22	South part of Mare Crisium	14.4	107	xx	x				x	xx	x	x	70	0.229	x
+0.96	+0.250	East edge of Mare Crisium	23.4	139		x						x	x	40	0.194	x
+0.960	+0.215	East of Condorcet	1.3	100	x					x			x	25	0.09	
+0.725	+0.130	Between Taruntius and Da Vinci	4.1	109	x					x	x	x		35	0.136	
+0.775	+0.120	North edge of Fecunditatis	2.1	109		x					x	x		25	0.108	
+0.875	+0.115	West of Firmicus	9.7	109		xx				x		x	x	40	0.175	
+0.270	+0.060	Between Dionysius and De Morgan	13.6	123		x		x		x	x		x	30	0.050	x
+0.205	+0.050	South edge of Taruntius	7.1	114				x		x		x	x	30	0.072	
+0.330	+0.040	Northeast rim of Fitton	7.3	109		x		x		xx				35	0.125	
+0.345	+0.030	North rim of Goldine	7.	113		x				x			x	27	0.136	
+0.395	0.040	Southwest part of Tranquillitatis	1.	108		x		x		x			xx	30	0.136	
+0.395	-0.035	Southwest rim of Tranquillitatis	13.3	131	x	x	x	x		xx	x	xx		35	0.030	
+0.450	-0.030	South part of Tranquillitatis	14.9	109				x		x			x	30	0.122	
+0.495	+0.005	South rim of Tranquillitatis	8.	109	x	xx		x	x	xx			x	30	0.131	x
+0.600	+0.020	South rim of Tranquillitatis	30.4	108		x				xx		x	x	35	0.150	x
+0.560	-0.030	Southeast of Censorinus A	24.0	108							x			25	0.133	x
+0.510	-0.050	South of Censorinus A	2.0	146	x	x	x	x	xx	x				30	0.011	x
+0.540	-0.060	Southeast of Censorinus A	3.8	118	x	x	x	x	xx	x				30	0.064	x
+0.560	-0.050	Southeast of Censorinus A	3.4	107				x		x		x		20	0.133	

TABLE 5-1 - Concluded

COORDINATES		LOCATION	T (K°)	T (°K)	DATES OF OBSERVATIONS									SIZE (arc sec)	t (Lunar Days)	WRM
					9/11/71	9/12/71	9/13/71	9/14/72	11/8/71	9/29/72	9/30/72	10/1/72	10/2/72			
+0.510	-0.130	West of Isidorus	19.6	106		x	x		x	x	x	x		35	0.125	
+0.575	-0.105	Northeast of Capella	7.6	107	x		x	x		xx		x		35	0.136	
+0.780	+0.080	North rim of Ferunditatis	6.8	115		x			xx	xx		x	x	45	0.117	
+0.755	+0.025	North part of Ferunditatis	4.3	127					x	xx		x	x	50	0.069	x
+0.960	+0.070	Just west of Schubert	10.0	105						x	x	xx		35	0.246	
+0.925	+0.050	Northeast of Mare Spumans	25.6	114	x	x			x	x	x		x	70	0.156	
+0.905	+0.030	In Mare Spumans	24.7	105	x	x			x	x	x		x	70	0.258	
+0.885	-0.020	Southeast of Webb	17.9	113	xx	x			xx	xx	xx	xx	x	60	0.144	

and Westphal catalog. Our data seems to be comparable in quality to theirs, and all of their more intense anomalies which lay in our scan paths were recorded.

An attempt was also made to find cool anomalous areas in the October 1, 1972 data which would correlate with data of other nights. Several candidate areas were noted, but each of these correlated with data of only one other evening. Their existence seems dubious. Our data indicates that if such areas exist, they are much less abundant than the warm anomalies.

6. DISCUSSION OF ERRORS

Since the lunar surface temperatures are location-dependent, as well as time-dependent, errors in the temperature values are inevitably linked with errors in positioning and time of measurement of the contours. However, it is convenient to attempt separate treatment of these cases.

6.1 TIME ACCURACY

The time error of measurement of an individual value is negligible. However, it should be noted that the recording of data sufficient for a single contour map may require several hours to accomplish.

6.2 SPATIAL ACCURACY

Probably the greatest uncertainty in the positioning of the contours occurs in the focal plane mirror alignment, which is done just prior to observation. For the data presented here, this is estimated to produce a probable error of 0.005 lunar radii. Error also arises in the identification of the photograph coordinates, and this is estimated here as 0.004 lunar radii. The astrometric calculations are done to the accuracy of the data in the Ephemeris (Ref. 23), and the error should be an order of magnitude smaller. In summary, the contours are estimated to have a probable spatial error of 0.006 lunar radii, and a maximum spatial error of 0.018 lunar radii.

6.3 TEMPERATURE ACCURACY

Implicit differentiation of Equation 4-16 yields the fractional variation in the measured temperature T_m as a function of variations of the parameters. This differentiation gives

$$\frac{dT_m}{T_m} = D(T_m)\left(\frac{dV_m}{V_m} - \frac{d\bar{\tau}_a}{\bar{\tau}_a} - \frac{dK}{K}\right) \qquad (6\text{-}1)$$

where

$$D(T) = \frac{Q}{T}\left(\frac{dQ}{dT}\right)^{-1} \quad . \qquad (6\text{-}2)$$

The value of dK/K is obtained by differentiation of Equation 4-15. To obtain a fairly simple expression, it is necessary to assume that all lunar calibration points have identical temperatures and that the signal and atmospheric transmission values are the same. This is not an unreasonable assumption for this type of order-of-magnitude calculation. If the calibration observations are all recorded at approximately the same time, the transmission values will, in fact, be approximately identical. The quantity dK/K is then given by

$$\frac{dK}{K} = \frac{1}{N}\sum\frac{dV_{ci}}{V_c} - \frac{1}{N}\sum\frac{1}{D(T_c)}\frac{dT_{ci}}{T_c} - \frac{d\bar{\tau}_{ac}}{\bar{\tau}_{ac}} \qquad (6\text{-}3)$$

for N observations. The subscript c refers to these calibration point observations. Combination of Equations 6-1 and 6-3 yields

$$\frac{dT_m}{T_m} = D(T_m)\left[\frac{dV_m}{V_m} - \frac{1}{N}\sum\frac{dV_{ci}}{V_c} - \frac{d\bar{\tau}_a}{\bar{\tau}_a} + \frac{d\bar{\tau}_{ac}}{\bar{\tau}_{ac}} + \frac{1}{N}\sum\frac{1}{D(T_c)}\frac{dT_{ci}}{T_c}\right]. \qquad (6\text{-}4)$$

Equation 6-4 may be used to obtain an expression for the maximum fractional error in T_m. It is

$$\left(\frac{\Delta T_m}{T_m}\right)_{max} = D(T_m)\left[\left|\frac{\Delta V_m}{V_m}\right| + \left|\frac{\Delta V_c}{V_c}\right| + 2\left|\frac{\Delta \bar{\tau}_a}{\bar{\tau}_a}\right| + \left|\frac{1}{D(T_c)}\frac{\Delta T_c}{T_c}\right|\right] . \tag{6-5}$$

Here, each term in the brackets on the right side is the maximum fractional error in that quantity. The replacements $\sum|\Delta V_{ci}|_{max} = N|\Delta V_c|$ and $\sum|\Delta T_{ci}|_{max} = N|\Delta T_c|$ have been made.

If the probable error of measurement is defined as the standard deviation, the square of the probable fractional error in the resultant temperature will be the sum of squares of the probable fractional errors in the components for random error distributions (Ref. 24). In Equation 6-4, each deviation dV_{ci} and dT_{ci} must be treated as an individual component. The probable fractional error in T_m is then

$$\left(\frac{\Delta T_m}{T_m}\right)_{prob} = D(T_m)\left\{\left(\frac{\Delta V_m}{V_m}\right)^2 + \frac{1}{N}\left(\frac{\Delta V_c}{V_c}\right)^2 + 2\left(\frac{\Delta \bar{\tau}_a}{\bar{\tau}_a}\right)^2 + \frac{1}{N}\left[\frac{1}{D(T_c)}\frac{\Delta T_c}{T_c}\right]^2\right\}^{\frac{1}{2}} . \tag{6-6}$$

Here, the replacements $\sum(\Delta V_{ci})^2_{prob} = N(\Delta V_c)^2$ and $\sum(\Delta T_{ci})^2_{prob} = N(\Delta T_c)^2$ have also been used. The quantities ΔV_c and ΔT_c, as above, represent average values for these errors. Each term in the braces on the right side represents the square of the probable fractional error in the quantity. The first term in braces represents the noise error during an object point measurement. The second quantity represents the noise error during measurement of the calibration points. The third term is the error in the value of atmospheric transmission. The last term in braces represents the error in the calibration temperatures. It is of interest to note that the probable error in the determined temperature values

which is due to errors associated with the measurement of the calibration points is inversely proportional to the square root of the number of these points for a random distribution of these errors.

The requirement of random error distributions for Equation 6-6 suggests a more detailed examination of the nature of the errors of the various components. The fractional errors in the signal values are due to instrumental noise, sky noise, and errors in residual sky background correction. The first two sources are random, and the last includes both random and systematic variations. However, the errors in the residual sky background correction should be small because of the simultaneous background correction employed. The errors in atmospheric transmission are due to random fluctuations, systematic error due to error in the determined attenuation coefficient, and systematic error inherent in the band model approximation employed. Since calibration is effected on the Moon, systematic errors in the computed transmission will tend to cancel. In addition, the excellent quality of the 10- to 12-micrometer window will result in small transmission errors for data taken in this region. The largest cause of error lies in the calibration temperatures, T_c. Error in these temperatures may be divided into two sources: error in the Saari and Shorthill data used for calibration, and error in the approximation used to convert the Saari and Shorthill temperatures to our observation conditions. Except for zero-point error in the Saari and Shorthill data, trial calculation indicates that these errors are largely random. T error distributions of the parameters, for which each component in Equation 6-6 represents the probable error, should, therefore, be largely, although not entirely, random. This equation is, therefore, approximately correct. Since the values of the component errors are estimated, additional accuracy of Equation 6-6 achieved by increased complexity is not warranted.

Estimates have been made of the accuracy of the various parameters used in the temperature reduction. With these values, Equations 6-5 and 6-6 have been evaluated to obtain an indication of the order-of-magnitude error to be expected in the temperature values presented. The author has taken a probable noise voltage equivalent to that signal voltage for a noise temperature of 105°K. The maximum noise voltage is taken as twice the probable value. The quantity $(\Delta\tau/\tau)_{prob}$ is assumed to be 0.02 and $(\Delta\tau/\tau)_{max}$ was taken as 0.04. Ten calibration points were assumed, each having a temperature of approximately 350°K. The probable error in the calibration point temperatures was chosen to be 8 K°, with a maximum error of 16 K°. This takes into account the probable error of approximately 4 K°, indicated by Saari and Shorthill for their data points at 350°K. The results of the evaluation of Equations 6-5 and 6-6 are shown in Figure 6-1. The curves exhibit a minimum error around 150°K. For very low lunar surface temperatures, the first term inside the brackets becomes large because of the sharp decrease in the signal voltage V_m. In this case, the same noise signal value will correspond to a larger temperature difference than at higher temperatures. For temperatures above 150°K, the factor $T_m D(T_m)$, which increases with temperature, dominates. Here, the error in the signal is approximately proportional to that signal. Towards higher temperatures, the decrease in temperature change for given signal change is insufficient to offset this proportionality.

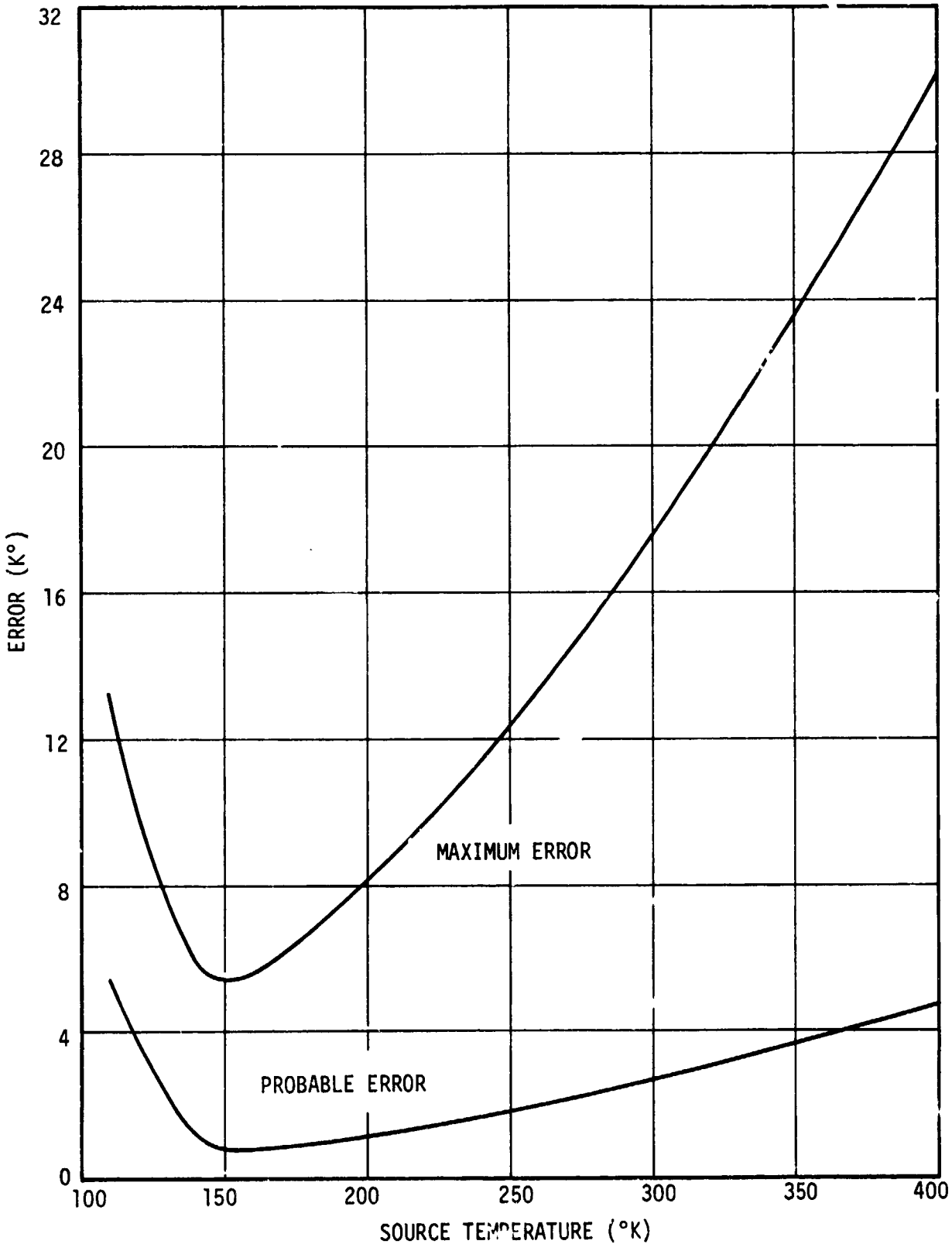

FIGURE 6-1. ESTIMATED ERROR OF THE SCAN OBSERVATIONS

7. MEASUREMENT OF THE MOON DURING THE TOTAL ECLIPSE OF FEBRUARY 10, 1971

Thermal measurements of the Moon during an eclipse are, in addition to such measurements of the dark surface, essential data for the distinction between the various proposed surface models. Measurements showing the variation of the absolute surface temperature as a function of time throughout the duration of an eclipse constitute the most desired information. For maximum utility, such cooling curve observations should be taken for as many different regions as possible.

The total lunar eclipse of February 10, 1971, provided an ideal opportunity for the acquisition of such data. The entire duration of the eclipse was visible from the Huntsville site and, in fact, throughout much of the Western Hemisphere. At Huntsville, the Moon was not far from the zenith during mid-totality, and the weather was cold and extremely clear.

7.1 THE OBSERVATIONS

Because of the limited duration of even the longest total lunar eclipse, observation by drift scanning the entire disc is not practical. Therefore, seven lunar regions were selected for spot measurements in the 10.0μ-12.5μ band. The orthographic coordinates for these regions are shown in Table 7-1, and these regions are also shown in Figure 7-1.

Some time after the eclipse it was discovered that an inadvertent error had been present in the alignment of the guide telescope used to set on the regions. When the German-equatorially mounted telescope was swung to the opposite side of the pier during mid-totality, a shift of approximately 0.12 lunar radii occurred in the lunar surface points

TABLF 7-1. LUNAR SURFACE REGIONS OBSERVED DURING THE ECLIPSE OF FEBRUARY 10, 1971
(Measured points have an uncertainty of ±0.020 in ξ and η)

REGION NO.	LUNAR NAME	MEASURED POINTS				CORRECTED POINTS	
		ξ_a	η_a	ξ_b	η_b	ξ	η
1	Tycho environs	-0.059	-0.749	-0.180	-0.695	-0.120	-0.722
2	Mare Nubium	-0.197	-0.210	-0.308	-0.166	-0.252	-0.188
3	Copernicus environs	-0.245	+0.098	-0.376	+0.162	-0.310	+0.130
4	Archimedes environs	-0.003	+0.483	-0.112	+0.562	-0.058	+0.523
5	Mare Serenitatis	+0.376	+0.379	+0.268	+0.430	+0.322	+0.404
6	Mare Tranquillitatis	+0.5[illegible]	+0.089	+0.435	+0.120	+0.496	+0.104
7	Hipparchus environs	+0.221	-0.196	+0.093	-0.147	+0.157	-0.172

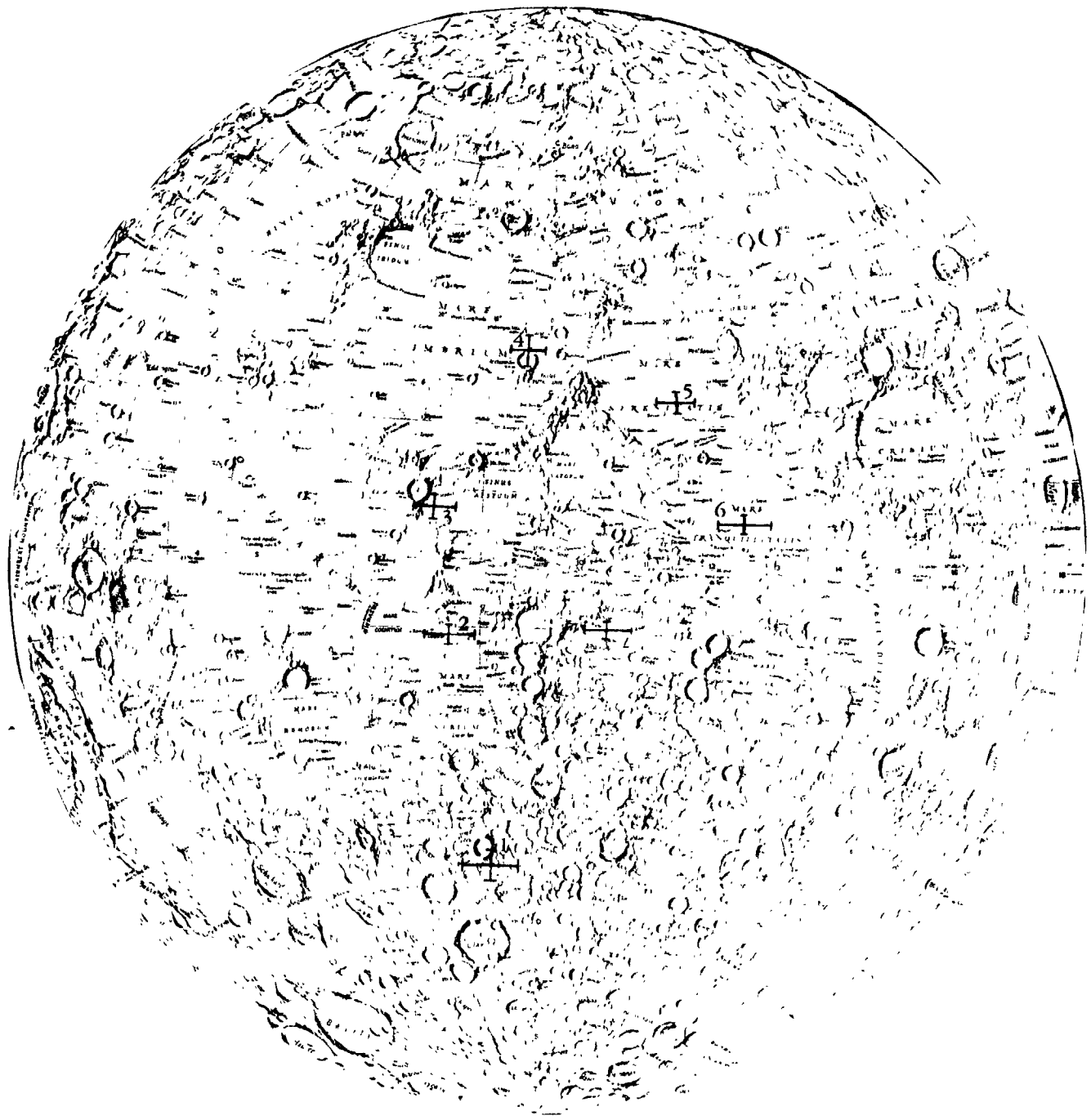

FIGURE 7-1. LUNAR REGIONS STUDIED DURING THE FEBRUARY 10 TOTAL ECLIPSE

measured. Such a position shift is manifested chiefly in the temperature-time curves as an alteration of the width of the curves from those for single points. An overall narrowing of these curves of about four minutes resulted and this necessitated the time correction procedure described in the appendix. The temperature values during eclipse are also slightly altered by three causes. The difference in eclipse temperatures due to the difference in eclipse duration and temperatures outside eclipse are negligible. Lastly, the random setting scatter of approximately 0.02 lunar radii about the individual points precludes a detectable temperature difference due to detailed local differences in lunar surface geology. For each of the seven regions studied, Table 7-1 lists the orthographic coordinates for the individual shifted points and the coordinates of each resultant point to which the time values were corrected.

The radiometer was used as attached to the 30-centimeter telescope at Huntsville. Observations were taken from more than 1 hour before first contact to approximately 1 hour after last contact. The 10- to 12-micrometer filter was used with an integration time of 1 second. The germanium bolometric detector was operated at 2°K with a chop frequency of 10 hertz. The chopping was between lunar and sky radiation by the scheme of Figure 2-1. The ac signal was fed through the same phase rectification amplifier and data acquisition system that is used for scanning data. The data were recorded only on paper printout.

The sequence of observations consisted of a spot measurement of the residual sky signal, followed by a spot measurement of each region in turn. Each spot measurement included a record of 15 printed signal values. The time was recorded during each measurement. The spot measurement time of 15 seconds was sufficiently short so that a significant change in lunar surface temperature did not occur during a measurement, even in the penumbral stages. Approximately 40 measurements were taken of each region.

7.2 DATA REDUCTION AND RESULTS

Since no astrometric analysis was required, data reduction was sufficiently limited so that it could be done by hand. For some necessary quantities which have a smooth variation with time, labor was saved by graphing these quantities and then reading off the values of the quantity for the desired times.

The first step of the reduction was the averaging of the signal values for each spot measurement. The spot measurements of the residual sky background were plotted as a function of time, and a smooth curve was drawn through the points. For each object point time, a value for the residual sky background was read from the curve, and this value was used to correct the associated object point measurement.

From data in the Ephemeris (Ref. 23) and from the known site location, the air mass for the center of the lunar disc was calculated and graphed as a function of time. This calculation included the effect of the topocentric parallax. An air mass value for each data point time was read from the graph. It is estimated that in the worst case, the error in atmospheric transmission made by using the disc center was less than 1 percent.

In order to conveniently effect calibration and to obtain an atmospheric attenuation coefficient, the assumption was made that following last contact of a lunar eclipse, the lunar surface quickly reaches the temperature distribution prior to first contact. Data of previous investigators (Ref. 22) support this assumption. Apparently, during a lunar eclipse, only the few millimeters near the surface are affected. Also, since the observations were taken in the 10- to 12-micrometer band, the weak line atmospheric absoprtion band model approximation should be applicable. A plot was made of the quantity $\ell n[V_m/Q(T_m)]$ as a func-

tion of the air mass, X, for all of the observations outside of eclipse. The values of T_m used in this plot were read from the data of Saari and Shorthill (Ref. 4) and were corrected for solar angle and distance by the method of Section 4-1. A computer-calculated table of the function Q(T) was useful for obtaining these values. This plot is shown in Figure 7-2. A line was fitted to the points by the least squares method, and this line is also shown in the plot. As shown by Equation 4-13, the slope of the line is the negative attenuation coefficient $-k_1$. This coefficient was found to be 0.053. Equation 4-15 was evaluated to obtain K, which was found to be 1,270 volts-cm²-ster./watt.

With these values for k_1 and K and with the graph of air mass as a smooth function of time, a graph was prepared of the quantity $1/K\bar{T}_a$ plotted as a smooth function of time. Values of this quantity were then read from the graph for each data point time, and these were multiplied by the corresponding signal values. Note that according to Equation 4-16, this product is equivalent to the radiance $Q(T_m)$ over the wavelength band. The computer-prepared table of Q(T) was then used to obtain the unknown T_m values.

In any study of the thermal response of the lunar surface to an eclipse the time is a crucial parameter. Because of the aforementioned position shift, the time values were corrected so that the measurements would apply to single lunar surface points. These points were chosen to be midway between the measured points. For calculation of these corrections it was assumed that the geocentric angular distance of any lunar surface point from the anti-solar point in the heavens (the direction of the Earth's shadow) is the key parameter, since, for given Earth-Sun and Earth-Moon distances, the insolation of that surface point depends solely upon this parameter. These corrections were obtained by calculating, for each

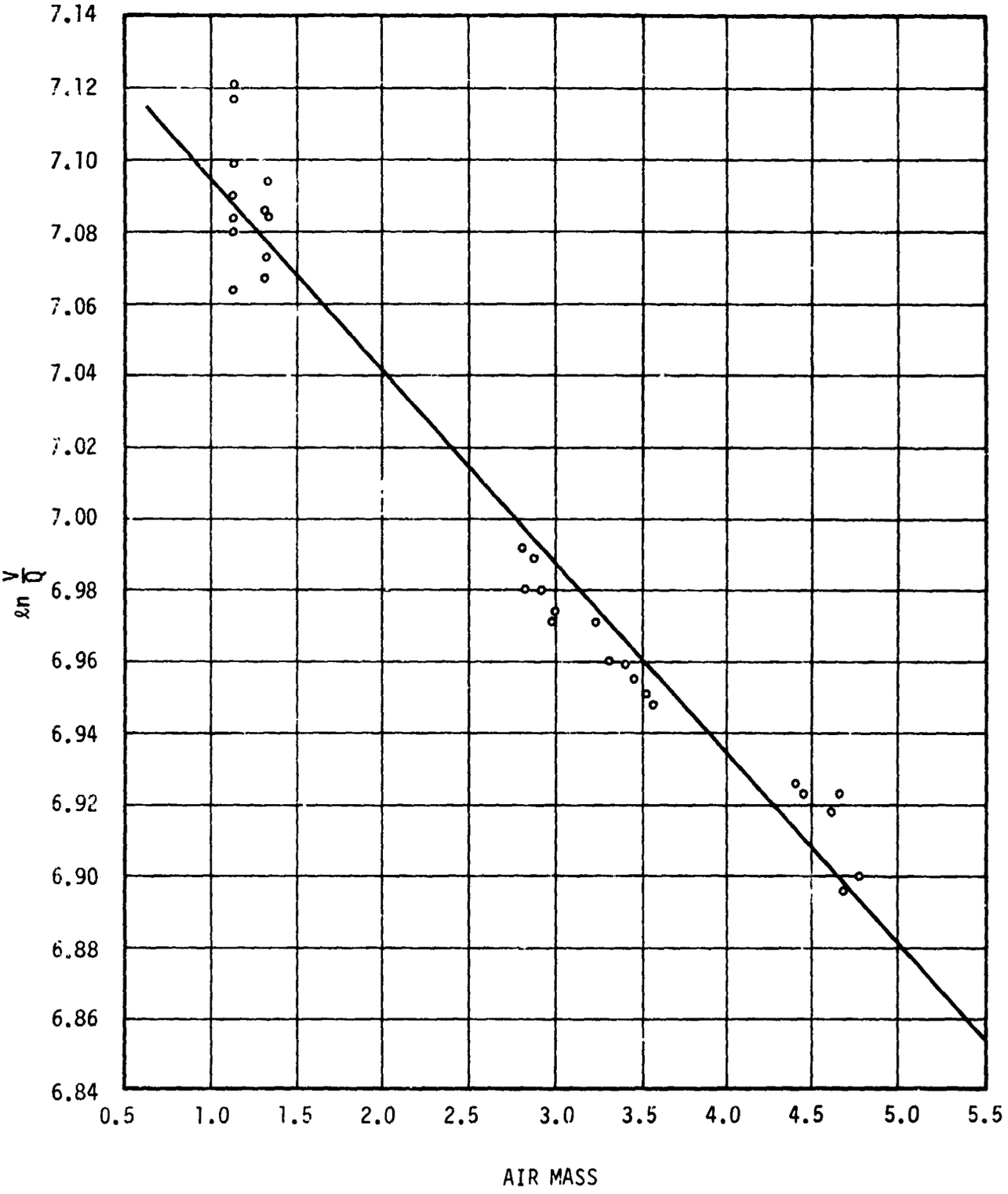

FIGURE 7-2. THE VARIATION OF $\ell n \frac{V_m}{Q(T_m)}$ AS A FUNCTION OF AIR MASS.

region at each data point time, the time shift by which the corrected point precedes (or succeeds) the observed point in having the same geocentric angular distance from the anti-solar point. The corresponding times for the corrected points were then obtained by applying these calculated time shifts to the data point times. Since these time corrections are small several simplifying approximations could be made. These approximations, the mathematical formulation for the time corrections, and the error of the approximations are presented in the appendix.

The resulting cooling curves for the seven lunar regions are shown in Figures 7-3 through 7-9. With the exception of region 1, these curves have approximately identical initial temperatures. It is of interest to note that region 1, which has a lower initial temperature, undergoes a smaller temperature decrease during eclipse. At the lower temperature, this region would not so severely radiate its heat to space.

For the purpose of fitting theoretical calculations, tabular data are more suitable. Therefore, these data are presented also in Table 7-2.

7.3 ERROR ANALYSIS OF TEMPERATURES

Equations 6-5 and 6-6 have been evaluated numerically to obtain an estimate of the accuracy of the eclipse observations. For this evaluation, the same values of the parameters have been used as for the scan data, with the exception of the approximate calibration temperature, the errors in calibration temperature, and the number of calibration observations. The following values have been used for the eclipse observations: $T_c = 390°K$, $(\Delta T_c)_{prob} = 10\ K°$, $(\Delta T_c)_{max} = 20\ K°$, and $N = 31$. These calibration temperature errors reflect the uncertainty of 5 K° indicated by Saari and Shorthill for their measurements at 390°K.

The results are shown plotted in Figure 7-10. The probable error is better than for the scan data, and reflects the larger number of calibration observations. This error is, in fact, lower than the uncertainty of any single value used for calibration, and shows the effect of error cancellation for a quantity derived from a large number of input quantities having randomly distributed errors.

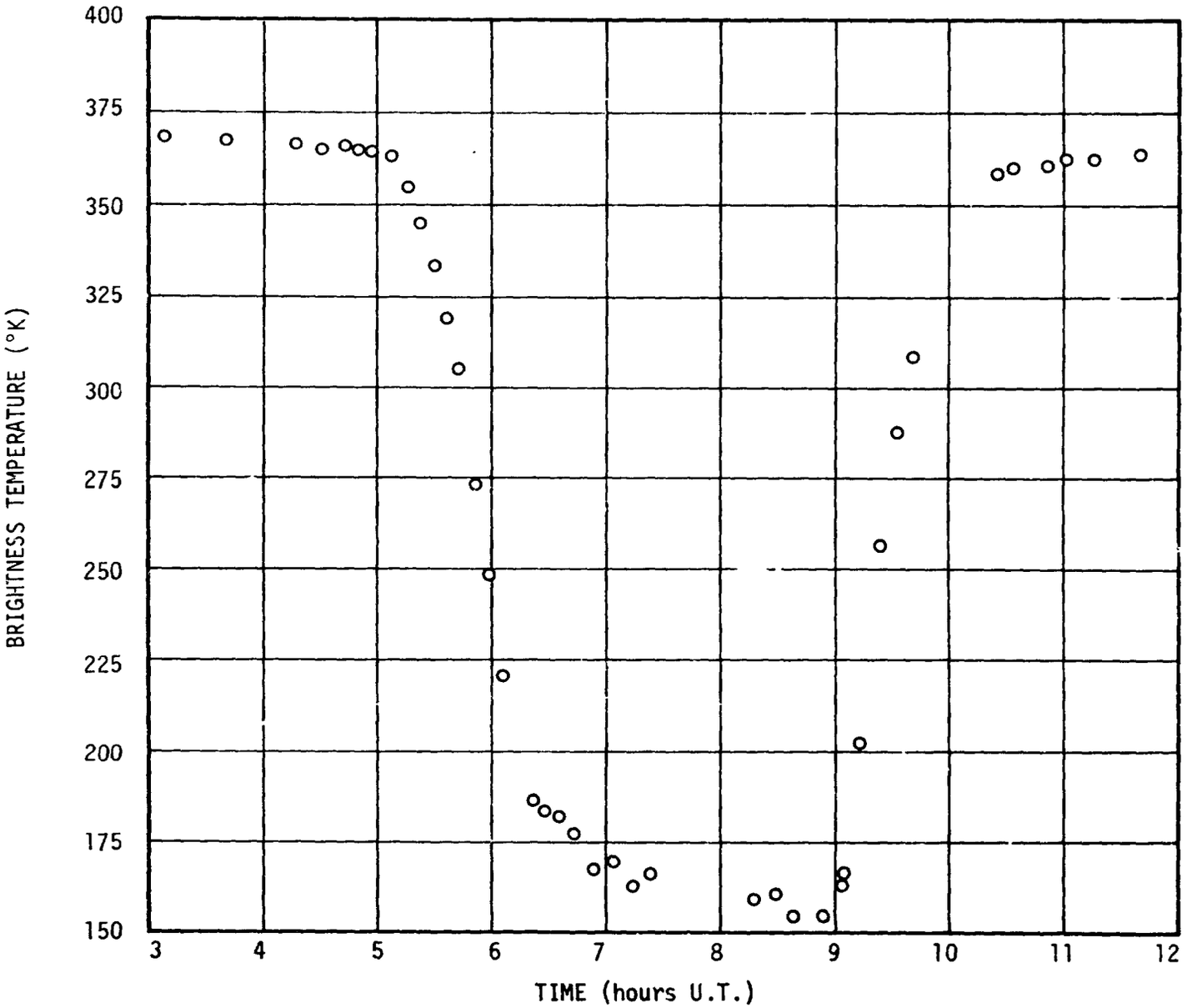

FIGURE 7-3. REGION 1, TYCHO ENVIRONS

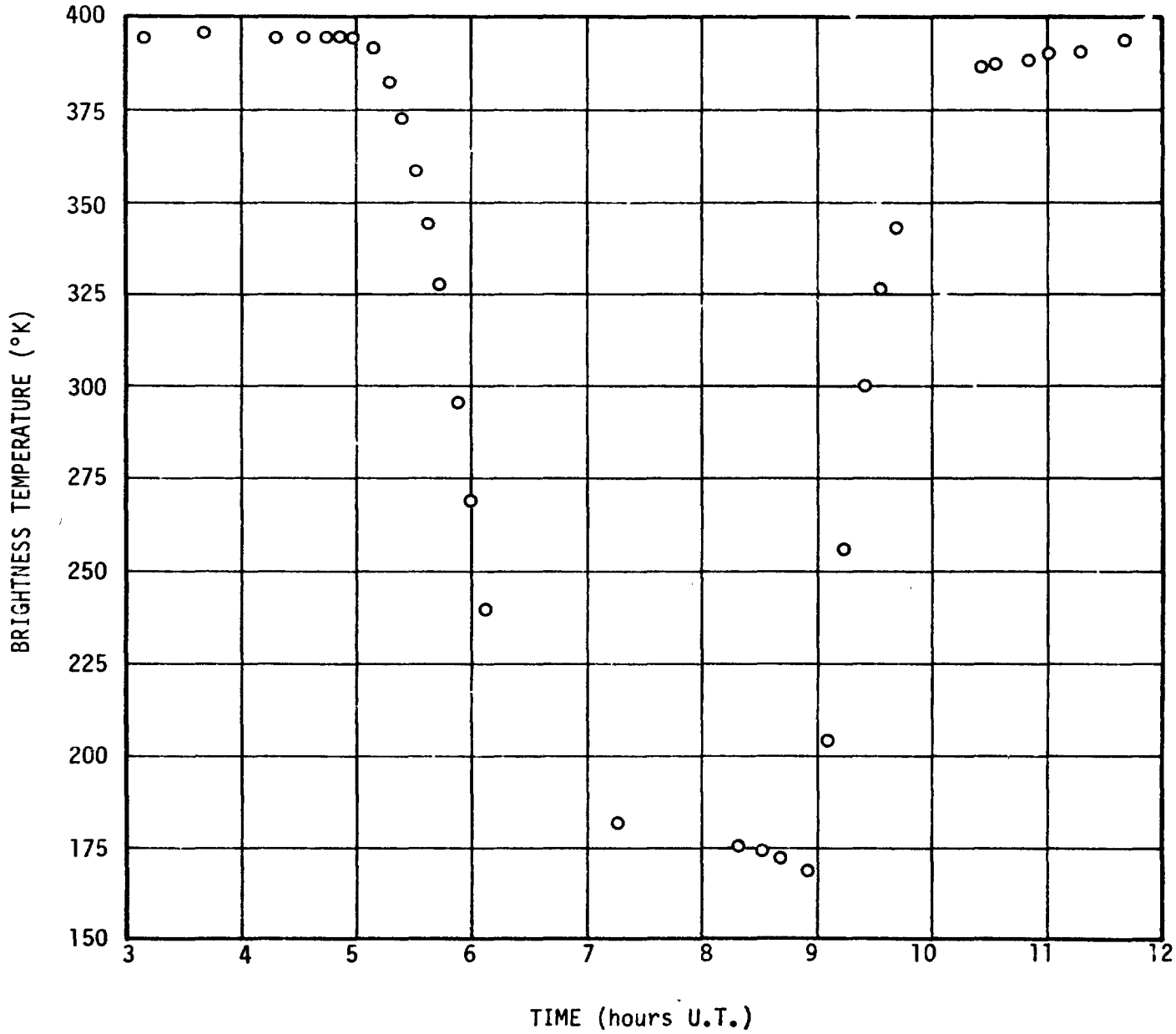

FIGURE 7-4. REGION 2, MARE NUBIUM

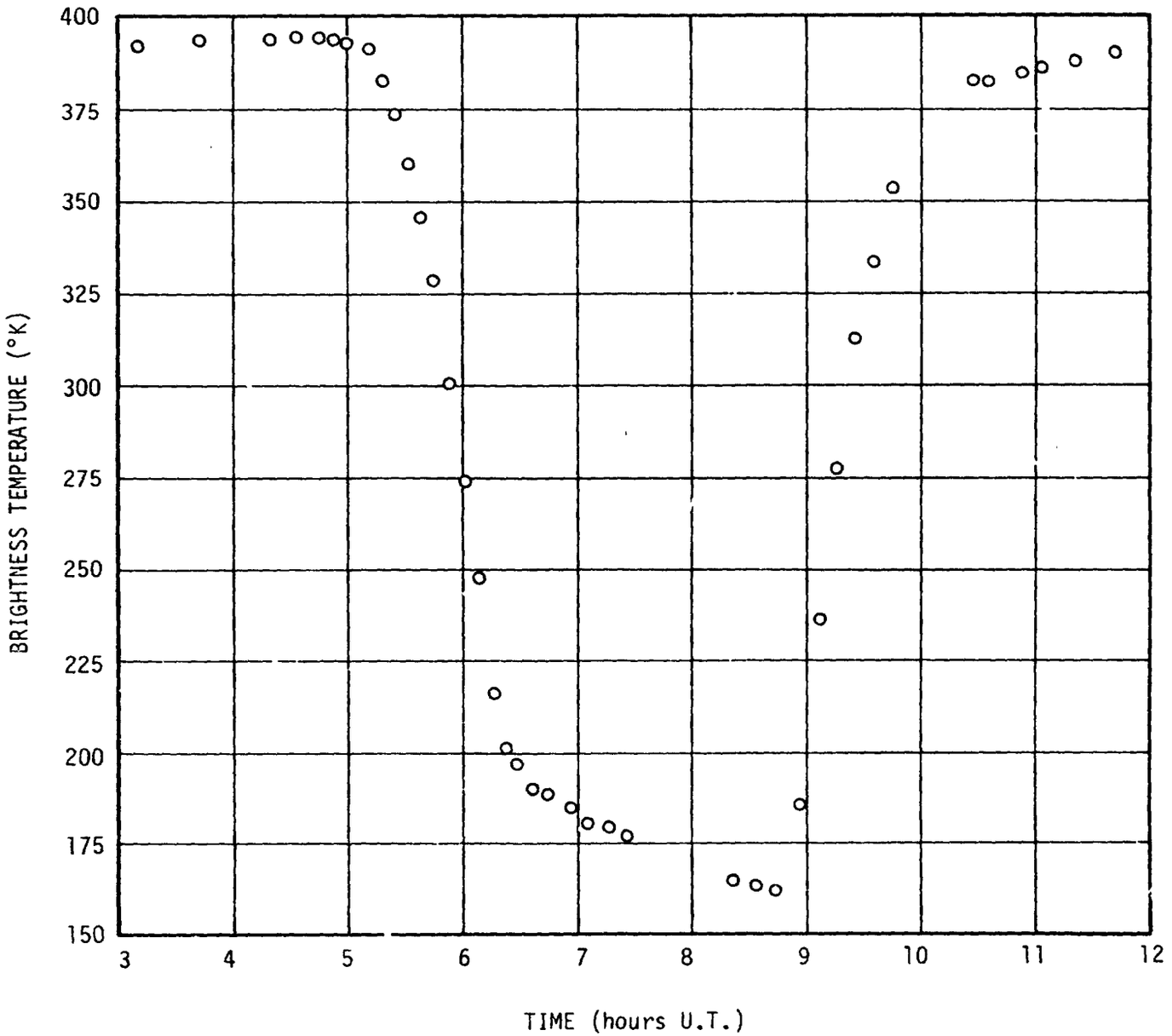

FIGURE 7-5. REGION 3, COPERNICUS ENVIRONS

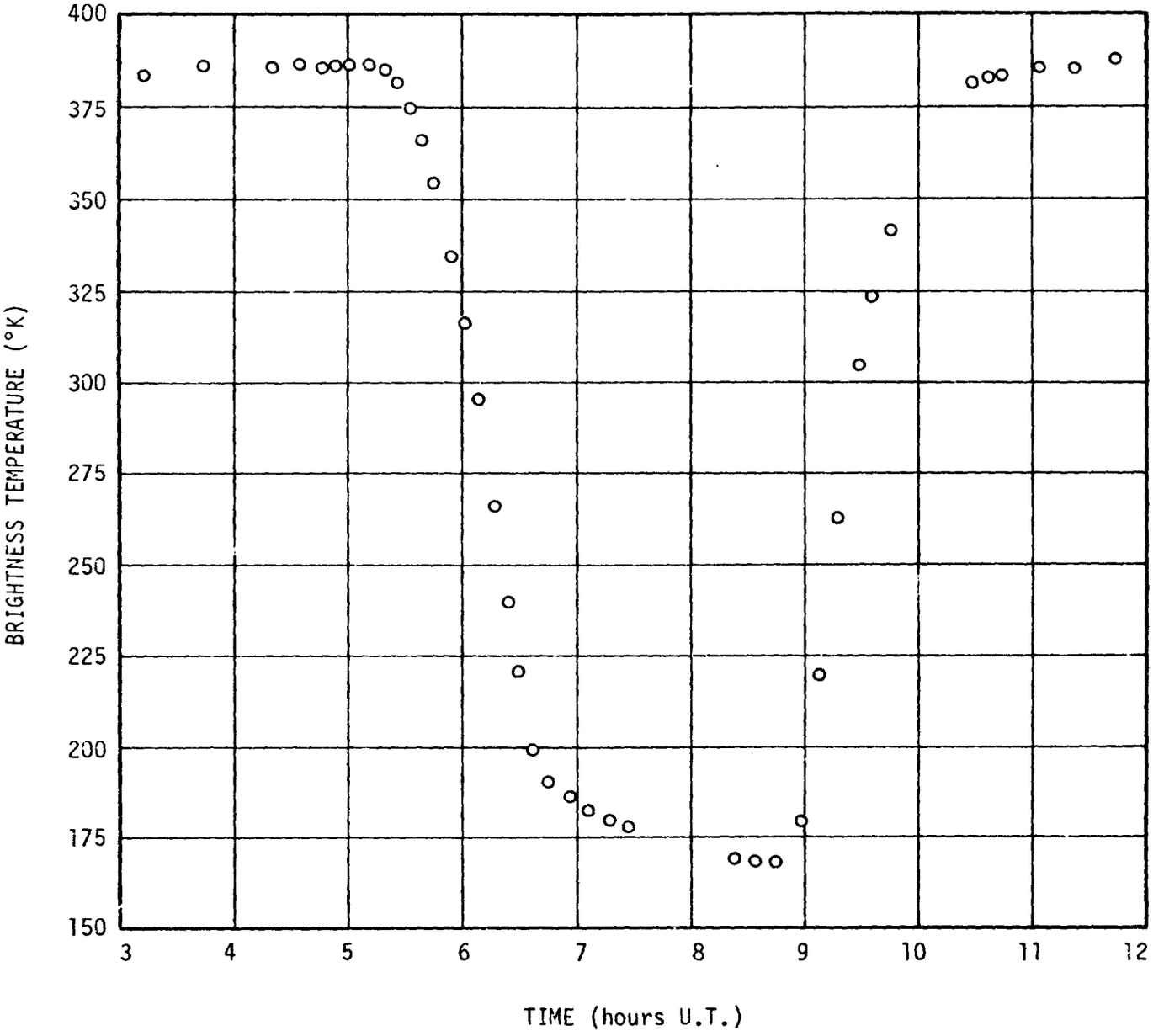

FIGURE 7-6. REGION 4, ARCHIMEDES ENVIRONS

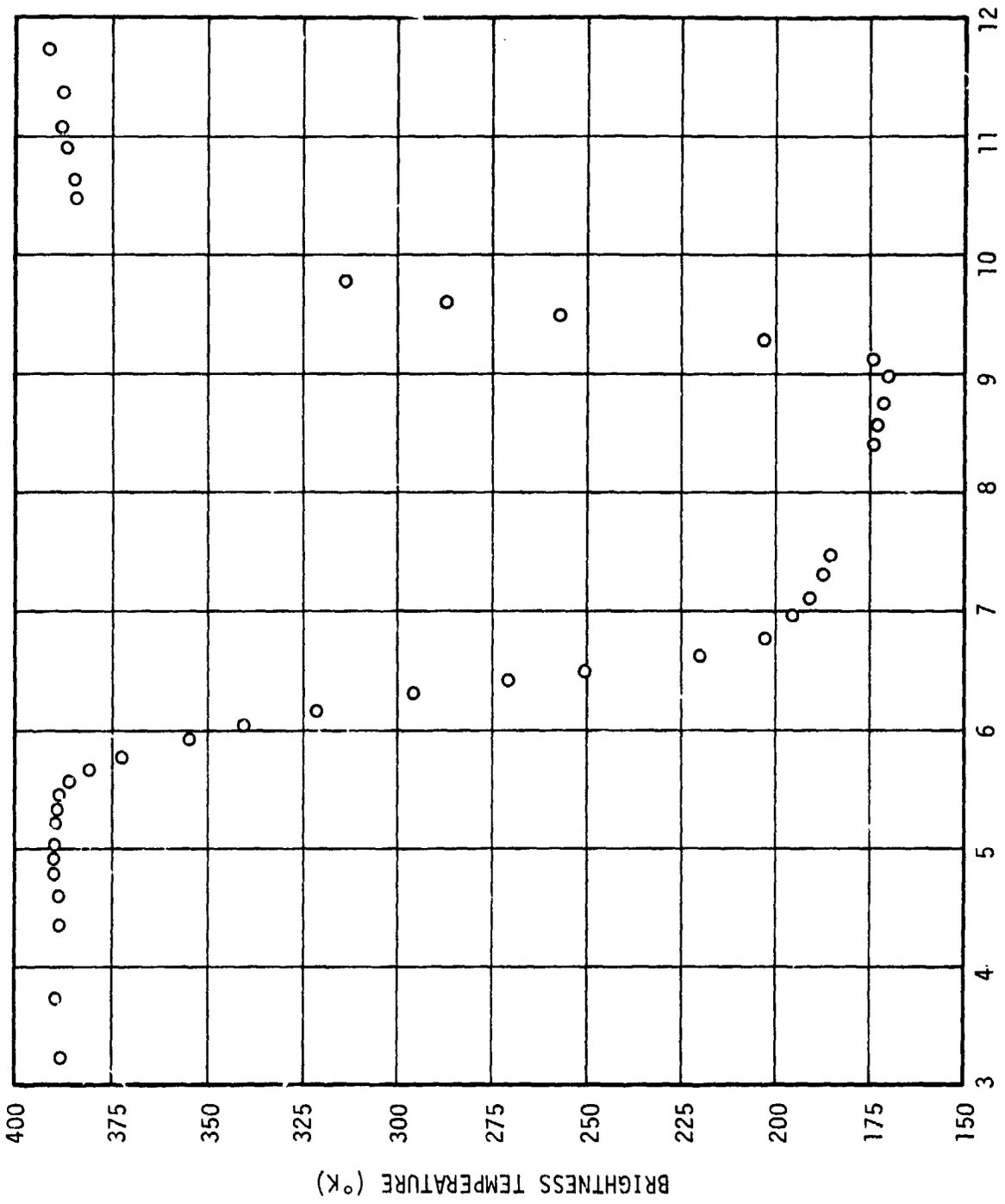

FIGURE 7-7. REGION 5, MARE SERENITATIS

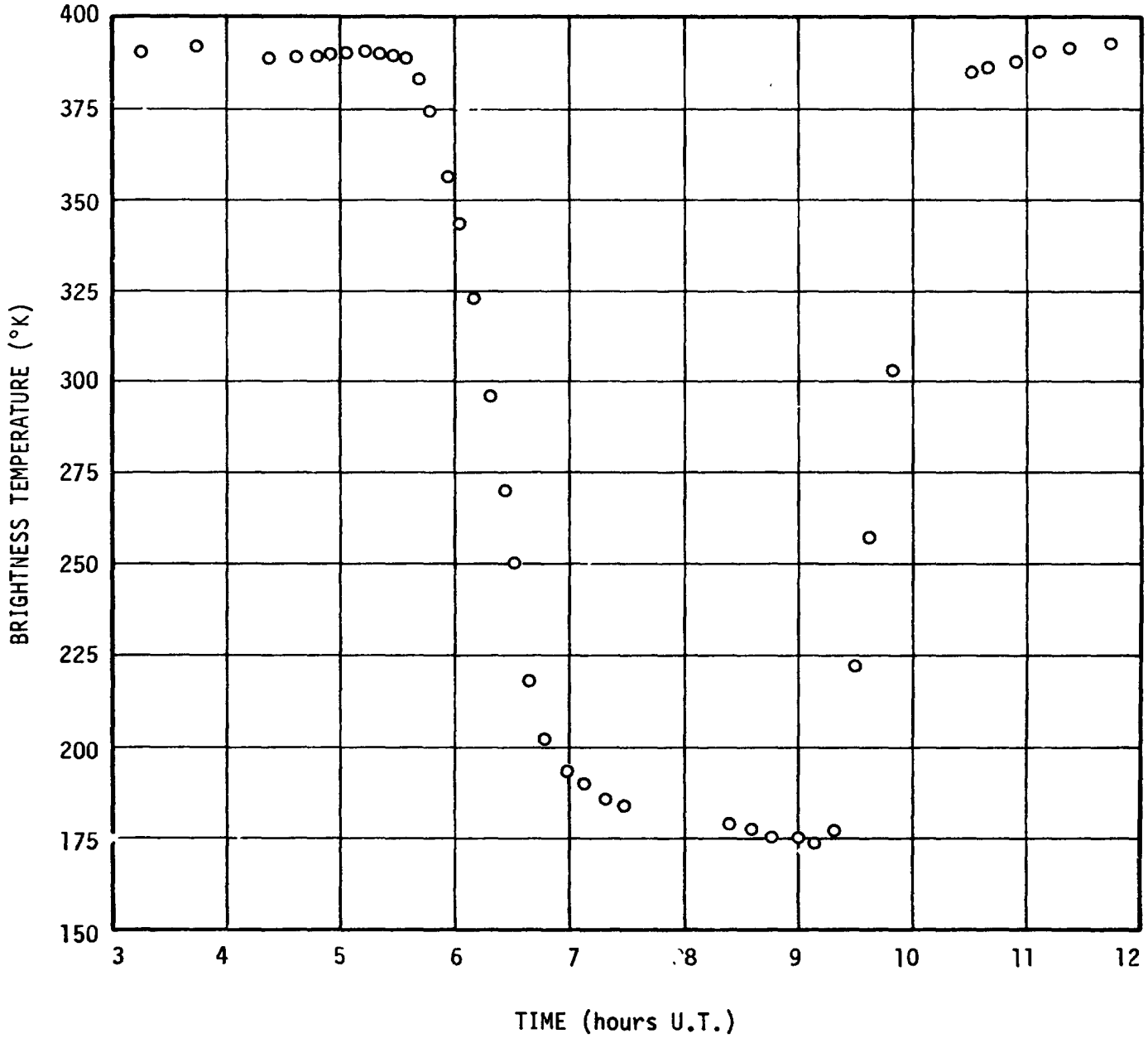

FIGURE 7-8. REGION 6, MARE TRANQUILLITATIS

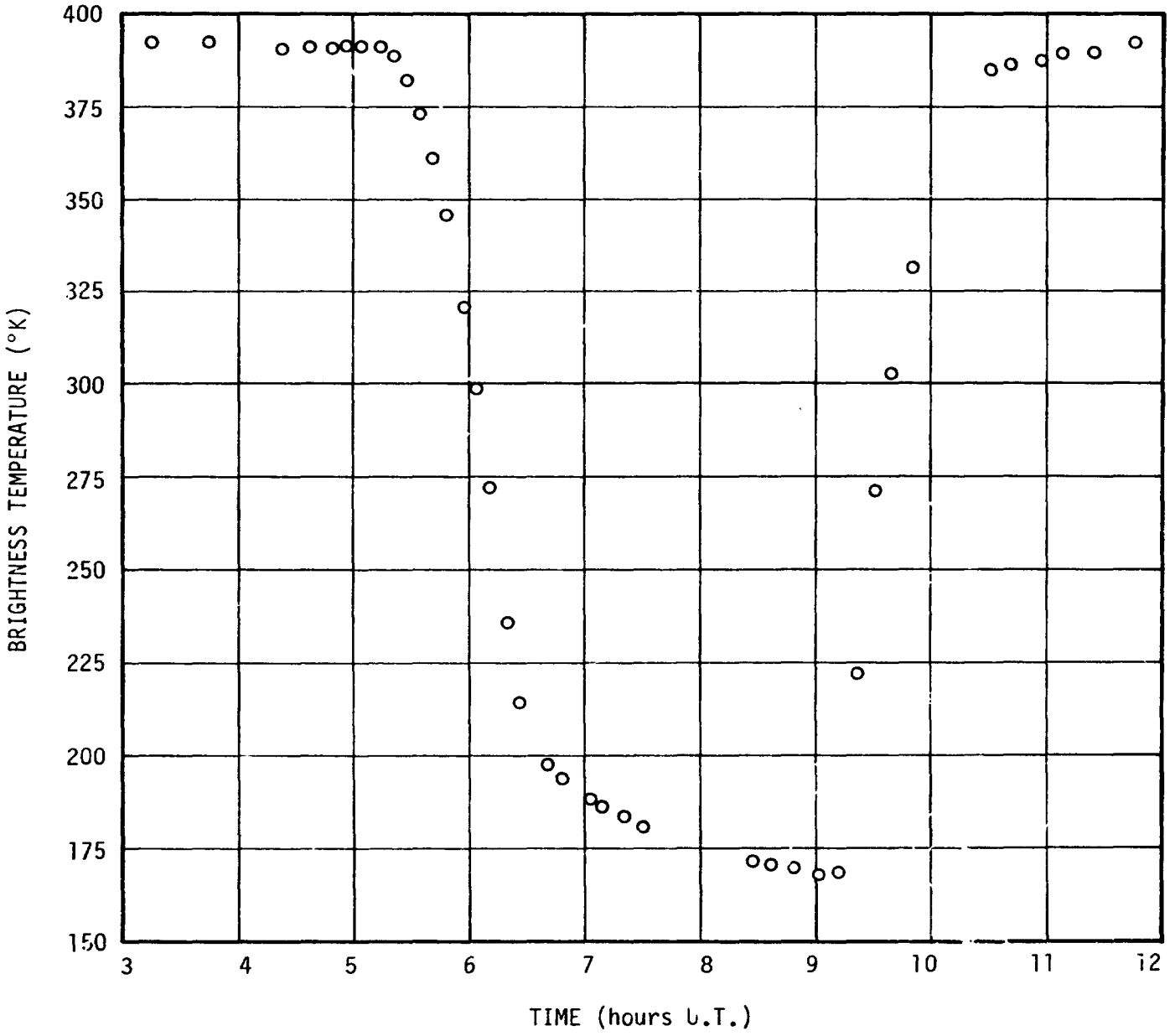

FIGURE 7-9. REGION 7, HIPPARCHUS ENVIRONS

TABLE 7-2. LUNAR SURFACE TEMPERATURE VARIATIONS DURING THE FEBRUARY 10 ECLIPSE

REGION 1: ξ = -0.120, η = -0.722				REGION 2: ξ = -0.252, η = -0.188			
TIME (U.T.) h m s	TEMPERATURE (°K)	TIME (U.T.) h m s	TEMPERATURE (°K)	TIME (U.T.) h m s	TEMPERATURE (°K)	TIME (U.T.) h m s	TEMPERATURE (°K)
03 08 15	368.3	07 13 57	163.5	03 09 38	394.8	09 13 53	255.8
03 40 51	367.2	07 22 36	166.6	03 42 07	395.4	09 24 44	299.9
04 18 10	366.4	08 17 13	159.3	04 19 11	394.4	09 33 57	326.9
04 32 01	365.1	08 29 22	160.8	04 33 28	394.8	09 42 10	343.1
04 44 10	365.9	08 38 11	154.7	04 45 36	394.6	10 26 56	386.5
04 51 22	365.2	08 53 58	154.8	04 52 23	394.8	10 34 17	387.2
04 58 04	364.6	09 03 08	163.3	04 59 15	394.4	10 51 11	388.2
05 08 30	363.3	09 04 02	166.3	05 10 07	391.4	11 01 43	389.9
05 17 03	354.9	09 12 35	202.3	05 18 14	382.2	11 18 17	390.9
05 23 30	345.2	09 23 49	256.4	05 24 37	372.9	11 40 53	393.4
05 30 19	333.9	09 32 34	287.6	05 31 38	358.9		
05 36 55	319.4	09 41 09	308.9	05 37 55	344.3		
05 43 06	305.0	10 25 48	358.9	05 44 08	327.7		
05 52 06	272.9	10 33 18	360.3	05 53 12	295.4		
05 58 44	248.3	10 49 45	361.2	05 59 57	269.4		
06 05 51	220.6	11 00 37	362.9	06 06 57	239.8		
06 22 16	186.6	11 16 05	362.9	07 16 01	183.2		
06 27 56	183.6	11 39 54	364.5	08 19 00	175.6		
06 35 07	182.0			08 31 16	174.1		
06 42 46	177.2			08 40 40	172.2		
06 53 29	167.7			08 55 06	168.2		
07 03 39	169.7			09 05 16	209.2		

TABLE 7-2 - Continued

REGION 3: ξ = -0.310, η = +0.130				REGION 4: ξ = -0.058, η = +0.523			
TIME (U.T.) h m s	TEMPERATURE (°K)	TIME (U.T.) h m s	TEMPERATURE (°K)	TIME (U.T.) h m s	TEMPERATURE (°K)	TIME (U.T.) h m s	TEMPERAUTRE (°K)
03 10 22	392.4	07 04 55	180.7	03 13 26	383.5	07 05 32	182.3
03 42 35	393.6	07 16 32	179.6	03 43 42	386.0	07 17 04	179.7
04 19 44	393.4	07 26 06	177.4	04 20 44	385.6	07 26 54	177.8
04 34 12	394.4	08 21 09	164.9	04 35 13	386.2	08 22 39	169.0
04 46 13	394.4	08 33 16	163.5	04 47 18	385.5	08 34 36	168.3
04 53 11	394.1	08 43 09	162.4	04 54 08	386.0	08 44 35	168.1
04 59 49	393.9	08 57 04	185.8	05 00 53	386.0	08 58 24	179.3
05 10 52	391.2	09 07 05	236.7	05 11 58	386.2	09 07 40	219.4
05 18 44	382.9	09 16 00	277.2	05 19 38	385.2	09 17 07	262.6
05 25 08	373.7	09 26 15	312.9	05 26 13	381.6	09 28 52	304.3
05 32 06	360.3	09 35 25	333.9	05 32 59	374.7	09 36 03	323.2
05 38 25	346.1	09 45 17	353.8	05 39 18	366.1	09 45 53	341.8
05 44 42	329.0	10 28 21	382.4	05 45 36	354.9	10 28 52	386.2
05 53 32	300.8	10 35 40	382.4	05 54 44	334.4	10 36 56	382.4
06 00 46	274.2	10 52 44	385.0	06 01 42	316.5	10 53 24	382.4
06 08 30	247.4	11 03 30	386.5	06 08 34	295.5	11 04 04	385.2
06 16 03	216.0	11 20 36	388.0	06 17 08	266.1	11 21 17	385.2
06 23 02	201.4	11 42 27	390.2	06 24 11	239.7	11 43 39	387.7
06 28 25	197.1			06 29 08	220.8		
06 35 47	189.9			06 36 42	199.2		
06 43 38	188.6			06 44 58	190.4		
06 55 59	185.0			06 56 51	186.6		

TABLE 7-2 - Continued

REGION 5: ξ = +0.322, η = +0.404				REGION 6: ξ = +0.496, η = +0.104			
TIME (U.T.) h m s	TEMPERATURE (°K)	TIME (U.T.) h m s	TEMPERATURE (°K)	TIME (U.T.) h m s	TEMPERATURE (°K)	TIME (U.T.) h m s	TEMPERATURE °K)
03 14 27	388.4	07 06 37	191.0	03 15 38	390.2	07 07 27	190.0
03 44 28	389.7	07 18 27	187.4	03 44 58	391.7	07 19 08	185.8
04 21 39	388.9	07 28 12	185.9	04 22 43	388.9	07 28 5[illegible]	184.0
04 36 39	389.2	08 22 58	173.9	04 37 26	389.2	08 23 48	178.9
04 48 14	390.2	08 34 50	173.1	04 48 48	[illegible]9.2	08 36 11	177.8
04 54 57	389.9	08 45 13	171.4	04 55 39	389.9	08 46 31	175.6
05 01 46	389.9	08 59 15	170.0	05 03 24	390.2	09 00 11	175.4
05 12 47	389.7	09 08 06	174.1	05 13 29	390.4	09 08 46	173 7
05 20 29	389.5	09 17 59	203.3	05 21 05	389.9	09 19 34	177.1
05 27 10	388.9	09 29 23	257.5	05 27 44	289.7	09 30 20	222.8
05 33 53	386.5	09 36 36	287.2	05 34 17	388.0	09 37 43	256.9
05 40 09	381.2	09 46 44	313.9	05 40 42	382.7	09 [illegible]9 49	303.0
05 46 29	372.6	10 29 38	384.2	05 47 43	374.5	10 30 41	385.2
05 56 01	354.7	10 38 17	385.2	05 56 34	356.4	10 40 04	386.7
06 02 39	340.7	10 54 03	387.0	06 03 13	343.6	10 55 26	388.2
06 09 38	321.6	11 05 20	388.0	06 10 15	323.2	11 07 27	390.4
06 18 42	295.6	11 22 32	388.5	06 19 18	295.9	11 23 59	391.7
06 25 14	270.9	11 44 03	391.9	06 25 50	270.2	11 44 49	392.4
06 30 10	250.5			06 30 58	250.2		
06 38 00	220.0			06 38 48	218.1		
06 46 07	202.9			06 47 02	202.3		
06 58 08	195.7			06 59 35	193.4		

TABLE 7-2 - Concluded

REGION 7: ξ = +0.157, η = -0.172			
TIME (U.T.) h m s	TEMPERATURE (°K)	TIME (U.T.) h m s	TEMPERATURE (°K)
03 16 51	392.4	07 08 26	186.1
03 45 53	392.4	07 20 16	183.9
04 23 47	390.7	07 30 11	181.0
04 38 48	390.9	08 27 18	171.3
04 49 51	390.4	08 37 05	170.5
04 56 37	391.4	08 48 15	169.8
05 04 35	390.9	09 01 39	168.0
05 14 50	391.2	09 10 57	168.6
05 22 07	388.2	09 21 33	222.0
05 28 36	381.9	09 31 23	271.2
05 35 05	373.2	09 39 50	302.5
05 41 48	361.2	09 50 58	331.0
05 48 43	345.8	10 31 56	385.4
05 57 43	320.8	10 41 47	386.2
06 04 17	298.7	10 58 06	387.5
06 11 16	272.2	11 08 35	389.2
06 20 27	235.7	11 25 01	389.7
06 26 39	214.3	11 46 32	391.7
06 40 19	197.5		
06 48 12	193.8		
07 01 05	188.2		

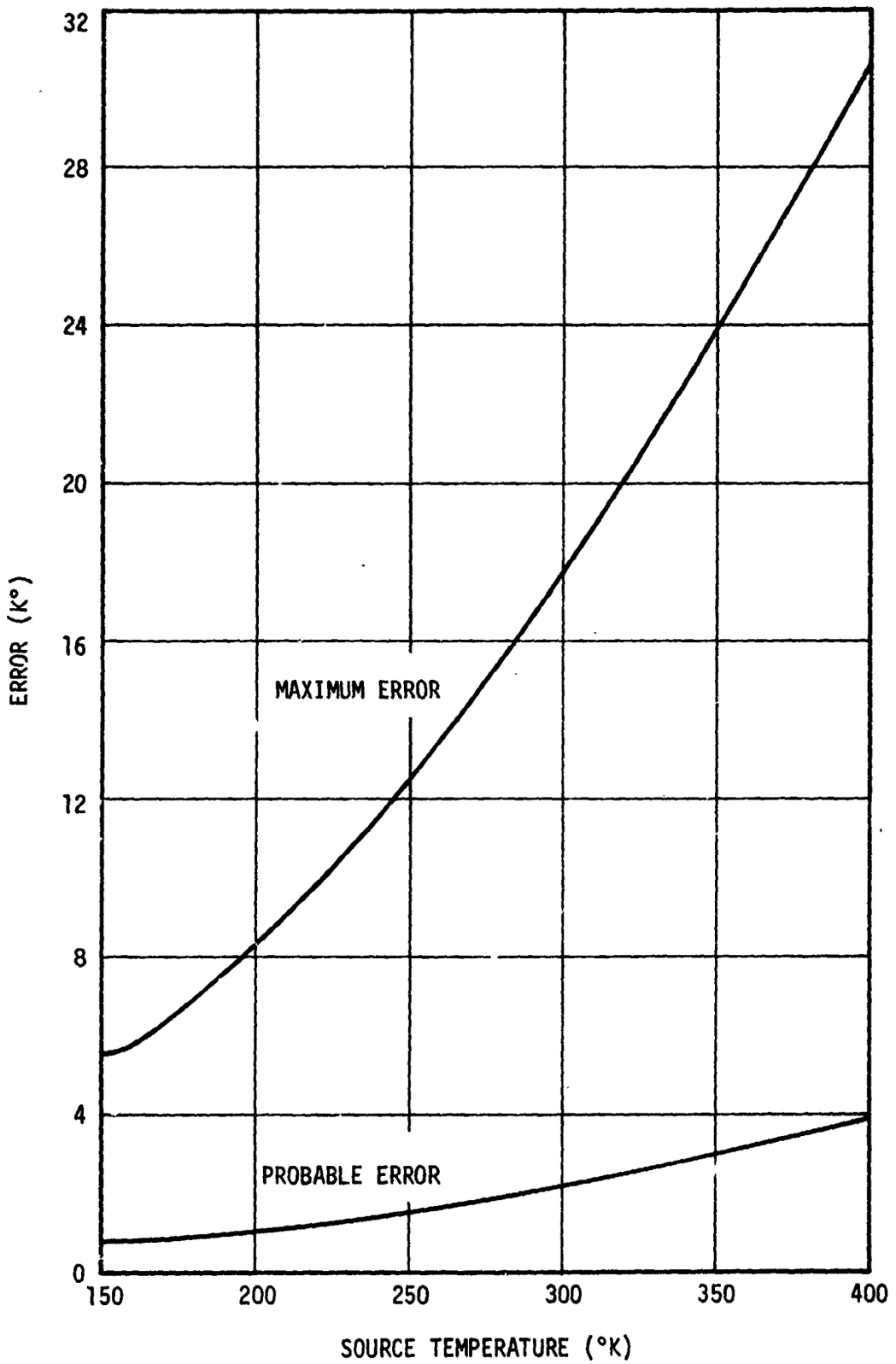

FIGURE 7-10. ESTIMATED ERROR OF THE ECLIPSE OBSERVATIONS

REFERENCES

1. Pettit, E. and S. B. Nicholson, "Lunar Radiation and Temperatures", Astrophysical Journal, 71, p. 102, 1930

2. Geoffrion, A. R., M. Korner, and W. M. Sinton, "Isothermal Contours of the Moon", Lowell Observatory Bulletin, V, No. 106, 1960

3. Sinton, W. M., "Eclipse Temperatures of the Lunar Crater Tycho", Lowell Observatory Bulletin, V, No. 108, 1960

4. Saari, J. M. and R. W. Shorthill, "Isothermal and Isophotic Atlas of the Moon", Boeing Scientific Research Laboratories, NASA CR-855, 1965

5. Saari, J. M., "The Surface Temperature of the Antisolar Point of the Moon", Icarus, 3, p. 161, 1964

6. Low, F. J., "Lunar Nighttime Temperatures Measured at 20 Microns", Astrophysical Journal, 142. p. 806, 1965

7. Mendell, W. W. and F. J. Low, "Low Resolution Differential Drift Scans of the Moon at 22 Microns", Journal of Geophysical Research, 75, No. 17, p. 3319, June 10, 1970

8. Murray, B. C. and R. L. Wildey, "Surface Temperature Variations During the Lunar Nighttime", Astrophysical Journal, 139, p. 734, 1964

9. Wildey, R. L., B. C. Murray, and J. A. Westphal, "Reconnaissance of Infrared Emission from the Lunar Nighttime Surface", Journal of Geophysical Research, 72, No. 14, p. 3743, July 15, 1967

10. Raine, W. L. and S. M. Landrum, "Use of a Direct-Imaging Filtered Radiometer for the Measurement of Lunar Brightness Temperatures", Teledyne Brown Engineering Summary Report RL-SSL-437, February 1969

11. Raine, W. L., "Reduction of Lunar Radiometer Data", Teledyne Brown Engineering, Interim Report RL-SSL-574, March 1969

12. Raine, W. L., "A Radiometer for the Measurement of Lunar Nighttime Temperatures", Teledyne Brown Engineering Summary Report SMSD-SSL-737, July 1969

13. Raine, W. L., "Development of a Radiometer for the Measurement of Lunar Nighttime Temperatures", Teledyne Brown Engineering Progress Report SSL-25166-1-1, October 1969

14. Raine, W. L., "The Astrometric Analysis of Lunar Radiometric Data", Teledyne Brown Engineering, Summary Report SMSD-SSL-1088, January 1970

15. Raine, W. L., "The Astrometric Analysis of Planetary Radiometric Data", Teledyne Brown Engineering, Summary Report SMSD-SSL-1139, April 1970

16. Raine, W. L., "A Radiometer for Lunar and Planetary Measurements in the Twenty-Micrometer Window", Teledyne Brown Engineering, Summary Report RL-SSL-1215, September 1970

17. Raine, W. L., "Thermal Mapping of the Lunar Surface", Teledyne Brown Engineering, Interim Report SE-SSL-1412, November, 1971

18. Ingrao, H. C., A. T. Young, and J. L. Linsky, "A Critical Analysis of Lunar Temperature Measurements in the Infrared", Harvard College Observatory, Scientific Report No. 6, April 1965

19. Elsasser, W. M., "Heat Transfer by Infrared Radiation in the Atmosphere", Harvard Meteorological Studies, No-6, Harvard University Press, Cambridge, Massachusetts, 1972

20. Goody, R. M., Quarterly Journal of the Royal Meteorological Society, 78, No. 165, 1952

21. Plass, G. N., Journal of the Optical Society of America, 50, No. 9, September 1960

22. Wesselink, A. J., "Heat Conductivity and the Nature of the Lunar Surface Material", Bulletin of the Astronomical Institutes of the Netherlands, 10, No. 390, p. 351, April 23, 1948

23. The American Ephemeris and Nautical Almanac, Department of the Navy, U.S. Naval Observatory, (Washington: U.S. Government Printing Office), published annually

24. Baird, D. C., An Introduction to Measurement Theory and Experiment Design, Englewood Cliffs, New Jersey, Prentice Hall, Inc., 1962

25. Winter, D. F. and J. M. Saari, "A Particulate Thermophysical Model of the Lunar Soil", The Astrophysical Journal, 156, p. 1135, June 1969

26. Raine, W. L., "Thermal Mapping of the Lunar Surface", Report SE-SSL-1649, Teledyne Brown Engineering Company, Huntsville, Alabama, pp. 5-9, September 1972

APPENDIX. ADDITIONAL CORRECTIONS TO THE SCAN AND ECLIPSE DATA

SCAN DATA CORRECTION FOR SMALL PHASE CHANGES

We begin with Equation 4-10. At the lunar subsolar point, this equation becomes

$$(1 - A)\frac{F_\odot}{d_\odot^2} \approx \bar{\epsilon}_m \sigma T_o^4 \qquad \text{(A-1)}$$

where T_o is the subsolar point temperature. Division of Equation 4-10 by Equation A-1 gives

$$\cos Z_\odot = \frac{T_m^4}{T_o^4} \qquad \text{(A-2)}$$

for the same value of $d_\odot$. We now differentiate Equation A-2 and divide by this same equation. The result is

$$\Delta T_m = -\frac{T \tan 2_\odot}{4} \Delta Z_\odot \qquad \text{(A-3)}$$

in the approximate Δ-notation. This is the relation used for phase correction over most of the illuminated surface. It may, however, be placed in a more convenient form. Equation 4-11 gives the relationship between the lunar solar zenith angle $Z_\odot$ and the lunar orthographic coordinates of the Sun and object point. Note that the Sun always lies almost in the lunar equatorial plane, so that $_\odot \approx 0$. If substitutions in terms of the selenographic longitudes ℓ and $_\odot$ are made into Equation 4-11, this equation takes the form

$$\cos Z_\odot = (1 - \eta^2)^{\frac{1}{2}} \cos(\ell - \ell_\odot) \quad . \qquad \text{(A-4)}$$

After differentiation, substitution for cos $(\ell - \ell_\odot)$, and use of $\Delta\ell_\odot = -2\pi\Delta\tau$, this equation becomes

$$\Delta Z_\odot = \pm \frac{(1 - \eta^2 - \cos^2 Z_\odot)^{\frac{1}{2}}}{\sin Z_\odot} 2\pi \Delta\tau \qquad \text{(A-5)}$$

in the Δ notation. The variable τ represents time expressed in lunar days. We now substitute Equation A-5 into Equation A-3 and use Equation A-2. The result is

$$\Delta T_m = \mp \frac{\pi}{2} T_m \left[(1 - \eta^2) \left(\frac{T_o}{T_m} \right)^8 - 1 \right]^{\frac{1}{2}} \Delta\tau \ . \qquad \text{(A-6)}$$

For the lunar afternoon surface the minus sign is chosen; the positive sign applies to the forenoon surface.

The model of Winter and Saari (Ref. 25) is used for phase correction over the nighttime surface. Their cooling curve may be fitted with sufficient accuracy by the quadratic

$$\tau = 0.0001537\ T_m^2 - 0.0461\ T_m + C \qquad \text{(A-7)}$$

where C is a constant. Differentiation provides

$$\Delta T_m = \frac{-\Delta\tau}{0.0461 - 0.0003074\ T_m} \ , \qquad \text{(A-8)}$$

which is the equation used for lunar darkside phase adjustment of temperatures.

Special consideration should be given to the lunar daytime surface near the terminator, for here the assumption of small conducted flux used in deriving Equation A-6 is invalid. The observational data indicate that near lunar sunset the surface temperature gradient $-dT_m/dZ_\odot$ reaches a maximum value of approximately

$$\left(-\frac{dT_m}{dZ_\odot}\right)_{max} = \frac{4000}{2\pi} \frac{°K}{\text{radian}} , \qquad (A-9)$$

and that this value is independent of selenographic latitude. The corresponding temporal gradient is obtained from

$$\left(-\frac{\Delta T_m}{\Delta \tau}\right)_{max} = \left(-\frac{\Delta T_m}{\Delta Z_\odot}\right)_{max} \frac{\Delta Z_\odot}{\Delta \tau} \qquad (A-10)$$

where the factor $\Delta Z_\odot/\Delta \tau$ is obtained from Equation A-5. Note that near the terminator $Z_\odot \approx \pi/2$. Thus

$$\left(-\frac{\Delta T_m}{\Delta \tau}\right)_{max} = 4000\ (1 - \eta^2)^{\frac{1}{2}} \frac{°K}{\text{lunation}} . \qquad (A-11)$$

The temporal gradient indicated by Equation A-6 reaches this value at $T_m = 209°K$ which is independent of η. On the darkside, the temporal gradient given by Equation A-8 has this value on the equator at $T_m = 149°K$. The observational data indicate that bright side temperatures near lunar sunset do not drop to much less than this value. In this boundary region near lunar sunset for $209°K > T_m > 149°K$, a phase adjustment interpolated between Equation A-6 at $T_m = 209°K$ and Equation A-8 at 149°K has been chosen. The adjustment equation for this region is

$$\Delta T = -66.7 \left[(1 - \eta^2)^{\frac{1}{2}} (T_m - 149°K) + (209°K - T_m)\right] \Delta \tau . \qquad (A-12)$$

Equations A-6, A-8, and A-12 have been incorporated into the computer reduction program. At present Equation A-6 is used for the entire lunar forenoon surface, but data sufficient to test the adjustment in the lunar sunrise region has not yet been reduced. The presently reduced data indicate that this phase adjustment procedure is satisfactory over the small phase changes for which it has been employed.

ECLIPSE DATA TIME SHIFT CORRECTION

The approximations made for the calculation of the eclipse time shifts are that the motions of the Moon in right ascension and declination were uniform over the time period of the eclipse, that the spherical astronomical coordinate system could be replaced by a rectangular system over the region of sky covered by the eclipse, that the geocentric librations could be neglected, that the variation of geocentric position angle during the eclipse could be neglected, and that the differential approximation could be used. The consequences of these approximations are examined at the end of this subsection.

During the time period covered by an eclipse, the separation in right ascension and declination between any lunar surface point and the antisolar point (the direction of the Earth's shadow) are given very nearly by the linear expressions

$$\alpha - \alpha_{AS} = \alpha_o + \dot{\alpha} t \ ,$$

and (A-13)

$$\delta - \delta_{AS} = \delta_o + \dot{\delta} t \ .$$

Here α_o, $\dot{\alpha}$, δ_o, and $\dot{\delta}$ are constants. In the rectangular approximations the apparent angular separation r between these points is given by

$$r^2 = (\alpha - \alpha_{AS})^2 \cos^2 \delta_o + (\delta - \delta_{AS})^2 \quad . \tag{A-14}$$

Equations A-13 may be substituted into Equation A-14, and the resulting equation may be solved for t as a function of α_o, $\dot{\alpha}$, δ_o, $\dot{\delta}$, and r. The total differential is then taken according to

$$dt = \frac{\partial t}{\partial \alpha_o} d\alpha_o + \frac{\partial t}{\partial \delta_o} d\delta_o \quad . \tag{A-15}$$

Equations A-13 and A-14 are again used for substitution for r in Equation A-15. If the approximate Δ-notation is used, the final expression for Δt is

$$\Delta t = \frac{-1}{\dot{\alpha}^2 \cos^2 \delta_o + \dot{\delta}^2} \left[(\dot{\alpha} \cos^2 \delta_o) \Delta\alpha_o + \dot{\delta} \Delta \delta_o \right.$$

$$\left. \pm \frac{(\dot{\alpha} \delta_o - \dot{\delta} \alpha_o) \cos^2 \delta_o (\dot{\alpha} \Delta\delta_o - \dot{\delta} \Delta\alpha_o)}{\dot{\alpha}\alpha_o \cos^2 \delta_o + \dot{\delta}\delta_o + (\dot{\alpha}^2 \cos^2 \delta_o + \dot{\delta}^2)\, t} \right] . \tag{A-16}$$

This equation applies in the penumbra. Prior to mid-eclipse the negative sign is used; after this time the positive sign is chosen. Careful examination of Equation A-16 reveals that the first two terms in the brackets give the time shift due to the separation of the lunar surface points in the direction of apparent lunar motion relative to the antisolar point. The third more complex term gives this shift due to the combination of the separation of these points perpendicular to this direction and the circularly symmetrical shadow of the Earth.

Equation A-16 was applied to the eclipse data point times. The constants α_o and δ_o were calculated for each lunar surface point from data in the Ephemeris (Ref. 23). The angular velocities $\dot{\alpha}$ and $\dot{\delta}$ are also from ephemeral data, and the positioned shifts $\Delta\alpha_o$ and $\Delta\delta_o$ were obtained from the data of Table 7-1 and the ephemeral data. The time shifts calculated for the outer penumbral boundary were used for data point times outside eclipse; data point times during the total phase were corrected with time shifts computed for the penumbra-umbra boundary.

Error in the time correction due to the approximations used has been evaluated as follows. The Ephemeris indicates that fractional errors due to the nonuniform lunar motion in right ascension and declination have maximum values of 0.006 and 0.012, respectively. The rectangular coordinates representation will produce a fractional error of $1/2\Delta\delta \tan\delta$ due to the convergence of the meridians at the poles, and a fractional error of $1/4\Delta\alpha \sin\delta$ due to the curvature of the declination circles. The quantities $\Delta\alpha$ and $\Delta\delta$ represent the extent of sky covered at declination δ. Maximum values of these fractional errors are estimated as 0.006 and 0.003, respectively. The maximum fractional error due to neglect of the geocentric librations is of the order of $|\Delta\ell \tan\ell| + |\Delta b \tan b|$ for librations $\Delta\ell$, Δb, and surface point coordinates ℓ, b, and here is 0.004. The variation of the geocentric position angle causes a maximum equivalent fractional error equal to the variation in radians and here is 0.008. Finally, the fractional error due to the differential approximation occurs in the third term in brackets of Equation A-16. The fractional error due to this approximation is $\Delta y/2y[(r^2)/(r^2 - y^2)]$, where Δy is the point separation perpendicular to the direction of lunar motion through the shadow, r is the apparent angular distance from the antisolar point, and y is the value of r at mid-eclipse. The maximum fractional error due to this approximation occurs at the umbral boundary and is about 0.020. The maximum

fractional error due to all sources is 0.060 or 7 seconds in time. The probable fractional error is estimated to be 0.013, which is equivalent to about 1 second of time.